Lattice-Boltzmann simulations of driven transport in colloidal systems

Lattice-Boltzmann simulations of driven transport in colloidal systems

Academisch Proefschrift

ter verkrijging van de graad van doctor aan de Universiteit van Amsterdam op gezag van de Rector Magnificus prof. mr. P. F. van der Heijden ten overstaan van een door het college voor promoties ingestelde commissie, in het openbaar te verdedigen in de Aula der Universiteit op vrijdag 26 november 2004, te 14:00 uur.

door

Fabrizio Capuani

geboren te Rome, Italië

Promotor: prof. dr. D. Frenkel

Co-promotoren: dr. I. Pagonabarraga and dr. C. P. Lowe

Faculteit: Natuurwetenschappen, Wiskunde en Informatica

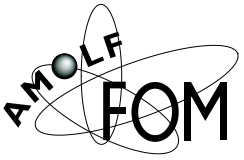

The work described in this thesis was performed at the FOM Institute for Atomic and Molecular Physics, Kruislaan 407, 1098 SJ, Amsterdam, The Netherlands. The work is part of the research program of the Stichting voor Fundamenteel Onderzoek der Materie (FOM) and was made possible by financial support from the Nederlandse Organisatie voor Wetenschappelijk Onderzoek (NWO).

to Ilaria Giulia and Annamaria,
who in the months of writings were one.

Contents

1 Introduction

Scientists have an effect upon society by finding out the details of how systems of practical interest work. The aim is either to obtain new knowledge, or learn how to use nature to our benefit. For this we need the basic rules of the systems, the governing equations, and we must know how to solve them for interesting conditions.

At the beginning of the twentieth century, scientists felt that, for macroscopic systems, all the relevant equations had been derived. Actually solving these equations for most practical problems is, however, a daunting task. Even though in the course of a few centuries, hundreds of talented scientists, including dozens of geniuses, worked on the solution of these equations, there are still many interesting practical situations and intriguing subtle interactions that lack a thorough understanding. It is not uncommon that areas of research that seemed exhausted suddenly regain the center of the scene. Perhaps a deeper understanding is needed to complement new experimental methods or for technological applications, or simply because new methods allow the solution of equations that previously seemed hopelessly intractable.

This thesis focuses mainly on *electro-hydrodynamics*. That is, systems where hydrodynamic (flow-induced) and electrostatic (charge-induced) interactions are of the same order of magnitude and are thus in competition. For applied purposes, a revival interest in this field has been driven by the practical needs of microfluidics and biophysics. On the theoretical side, electro-hydrodynamics is still challenging due to the inherent non-linearity of the relevant equations.

In microfluidics it was soon realized that the most efficient way to displace fluids in micro (or nano) capillaries is through electroosmosis. However, technological problems still remain unsolved. For example, the mixing of fluids at the extremely low Reynolds numbers that characterize very small scale flows remains an outstanding problem. In the context of biophysics, there is an additional question: living cells contain large numbers of charged (macro) molecules and large electric fields are maintained, in particular across membranes. Yet, little is known about the role of electrokinetic phenomena for molecular transport in cells.

The problem is, of course, that electrokinetic phenomena in all but the simples geometries cannot be treated analytically. One can imagine a protein in an electrolyte as a large charged particle surrounded by microions (of both signs) which rattle around while interacting with each other and with the protein, both electrostatically and hydrodynamically. The protein itself feels the environment and other proteins by means of forces, which can again being mediated by the solvent. However, all this complexity can actually help. Because the small particles move much faster than the large ones, they have time to explore so many configurations of phase space that they are, effectively, at equilibrium. To show this, let us estimate whether a microion is

able to follow the a colloidal particle in its most abrupt movement, a Brownian jump. We estimate the time of a Brownian jump of length l for a particle of mass m with friction coefficient ξ to be $\tau_j = m/\xi$. On the other hand, the time it takes an ion α of the electric double layer to relax to its equilibrium position in the layer is of the order $\tau_\alpha = l^2/D_\alpha$, where D_α is the diffusion coefficient of the ion. The electric double layer can be treated as approximately remaining in its equilibrium configuration if $\tau_\alpha \ll \tau_j$. Estimating the length of a jump as $l \approx u\tau_j$ and the particle velocity u as the root mean square value of one component of the thermal velocity $u = \sqrt{k_\mathrm{B}T/m}$ then, using the Stokes-Einstein relation $D\xi = k_\mathrm{B}T$, we find $\tau_j/\tau_\alpha \sim \xi_j/\xi_\alpha$. Using Stokes law, $\xi = 6\pi\eta a$, for the friction coefficient of a sphere of radius a in a fluid with viscosity η, we see that this corresponds to $a_\mathrm{ion} \ll a_\mathrm{particle}$. This condition is satisfied for colloidal particles.

Because retardation effects from the relaxation of the electric double layer are negligible, we can treat it "adiabatically". In this context, an important role is played by new types of computer simulations usually referred to as "Mesoscopic simulations". With this class of computer simulations one attempts a coarse graining procedure, recasting the microscopic description of a system, which would require solving the equations of motion for all the molecules, into a mesoscopic description where it is sufficient to follow the time evolution of the global properties of the system (mass and momentum density for example). There are several approaches to doing this, each with its own strategies, but the general procedure is to integrate out the fast degrees of freedom, reducing the actual simulation to only the slow ones. Among the mesoscopic simulations, the lattice-Boltzmann method (LB) (which I introduce in Chapter 2) has proved to have some very desirable properties for the study of the hydrodynamic interaction, especially from a computational point of view.

The first application in this thesis, and the only one unrelated to charged colloids, uses the LB method to study flow in random porous media. In Chapter 4 I show how velocity fluctuations decay in a simple model porous medium and how the use of approximate expressions, based on the pre-averaged properties of the flow, lead to large errors. This is contrary to the assumption underlying the existing theories for hydrodynamic dispersion. In an attempt to study flow in porous media, we introduce a highly simplified lattice-Boltzmann model for porous media. This model has the desirable property of possessing no excluded volume while allowing for friction on the fluid with a low density of obstacles. In my opinion, this model is ideally suited for studying the statistical properties of well behaved—in the sense that the spacial correlation functions decay exponentially—porous media. In the same chapter I show a simple way to obtain the largest possible Peclet numbers (in lattice simulations spurious diffusion always limits the Peclet number to small values).

Although the LB method is well established for the solution of flows in complex geometries, only recently has the study of the electrokinetic equations (Chapter 3), which couple electrostatics and hydrodynamics, been undertaken. In Chapter 5 I describe a novel method developed in the course of my PhD project that allows us to treat the electrokinetic equations and study previously unexplored flow conditions. Following the vogue, I should call the method a "hybrid" method because it couples a lattice-Boltzmann model of the neutral solvent with a discretization of the Smoluchowski description for the solutes. This combination of different methods is justified

by our choice of the level of description to use for the various components of the system (possible because of the scale separation between large colloidal particle and small ions). An important characteristic of the new method is that it strictly conserves mass and momentum at the level of the single node, thus rules out, from the very beginning, spurious mechanisms of transport. It is also very easy to implement and it is fully parallelizable. To illustrate the advantages of this pragmatic approach, in Appendix A I present two technical problems which originated from a different lattice-Boltzmann model. Small imbalances generated spurious mass currents at the boundary with a macroscopic object, that proved capable of obscuring the subtle interactions we were trying to study. In summary, although the method can be improved, I believe that it is already very flexible and well suited for studying colloidal suspensions of charged particles and microfluidics. Although in this thesis I have not extensively applied the method to the latter, in my opinion, that is the field were one might exploit fully its potential.

The remainder of the thesis concerns exploratory studies of the electrokinetic properties of charged colloids in electrolytes by means of the lattice-Boltzmann model presented in Chapter 5. In selecting this system to study, we were motivated by questions such as: how do the shape and charge distribution of a particle affect its mobility?

In Chapter 6, I describe computer simulations of the sedimentation velocity of highly charged spheres. I show that the sedimentation velocity can be discussed in terms of the equilibrium properties of the electric double layer. Moreover, at high charge, the surface-charge dependence of the sedimentation velocity is affected by the accumulation of charge on the surface of the sphere, and the sedimentation velocity resembles that of a sphere in an electrolyte with no-added salt, where coions cease to affect the sedimentation velocity of the spheres and only the dynamics of the counterions is relevant.

Another important aspect of the electrohydrodynamic interaction, which, once again, proves the flexibility of the method, is the study of the effect of the shape on electrokinetics. In Chapter 7 I study the role of shape, volume fraction, charge, and ionic strength on the sedimentation velocity of disks with non-zero thickness. They are relevant both practically and theoretically because they are a prototype for studying the effect of the shape and model real clay particles. I find that disk particles become hydrodynamically symmetric due to non-trivial interactions between the flow field near the particle and the electric double layer.

The last application I discuss concerns the electrophoretic mobility of a "patched" particle. In Chapter 8 I show how the electrophoretic mobility of such a sphere depends on the electric quadrupole moment and on the Debye screening length. I also show that if the particle undergoing electrophoresis is not exactly spherical (as occurs when representing a sphere on a lattice), one should consider also even electric multipole moments higher than the quadrupolar.

2 Hydrodynamics and the lattice-Boltzmann method

2.1 Introduction

Scientists associate a variety of meanings with the term "hydrodynamics". When I started as a novice in the field, I struggled for some time before realizing that there are at least two meanings of the word hydrodynamics, and two corresponding categories of scientists who claim the word and use it in a different way. On the one hand, we have scientists who study fluids as continuous media and are interested in their time evolution and interactions with obstacles and suspended particles. These scientists use the term hydrodynamic with its literal meaning: dynamics of fluids (liquid water—"hydros"—was, for ancient scientists, "the" fluid). On the other hand, for scientists concerned with collective properties of many microscopic molecules, the term "hydrodynamics" has a completely different meaning. It accounts for the dynamics of "dynamic variables" whose relaxation time is so slow as to be practically unaffected by the erratic motion of the microscopic constituents of the system. The latter degrees of freedom are so "fast" that they can be considered always in their equilibrium state. The realization that the "slow" variables follow the laws of the dynamics of fluids termed them "hydrodynamic variables". Even though this unification was one of the greatest results of statistical mechanics, the two concepts remain distinct and people who work on different fields refer to different levels of description when they talk about "hydrodynamics".

Throughout this thesis by "hydrodynamics" I will denote dynamics of the fluid. However, the simulation method which I used—the lattice Boltzmann method—heavily draws the ideas of statistical mechanics.

2.2 Phenomenological hydrodynamics equations

The phenomenological equations of hydrodynamics can be found in many text books (See, for example, [1, 2, 3, 4]), but because it is instructive to show their derivation I recapitulate here. Specifically, I will show the derivation of the macroscopic equations governing the motion of an isothermal, incompressible fluid in an adiabatic transformation (i.e. when heat exchange among different part of the fluid is negligibly small).

The state of a moving fluid is fully described if at each time t we can define the distribution of the fluid velocity $v(\mathbf{r}, t)$, and of two of the thermodynamic quantities of the fluid as, for example, the pressure $p(\mathbf{r}, \mathbf{t})$ and the density $\rho(\mathbf{r}, t)$ for every point

of space $\mathbf{r} \equiv (x, y, z)$. The evolution of a macroscopic state follows a path dictated by the basic conservation laws—i.e. the conservation of mass and of momentum—and the so-called constitutive equations, which are phenomenological laws.

Let us begin by considering the law of mass conservation. The mass of fluid in a volume element V_0 is $\int_{V_0} \rho \mathrm{d}V$. The mass of fluid flowing in a unit time through a surface element $d\mathbf{s}$ bounding V_0 is $\rho\mathbf{v} \cdot d\mathbf{s}$. Therefore, in absence of a sink or a source of mass, mass conservation implies that

$$\frac{\partial}{\partial t} \int_{V_0} \rho \mathrm{d}V = - \oint \rho\mathbf{v} \cdot \mathrm{d}\mathbf{s}, \tag{2.1}$$

where we follow the convention that the surface element $d\mathbf{s}$ is directed along the outward normal to the surface, hence the minus sign. By making use of Green's formula $\oint \rho\mathbf{v} \cdot \mathrm{d}\mathbf{s} = \int_{V_0} \nabla \cdot (\rho\mathbf{v}) \mathrm{d}V$, Eq. (2.1) can be written as $\int_{V_0} [\partial\rho/\partial t + \nabla \cdot (\rho\mathbf{v})] \mathrm{d}V = 0$. Because the volume element is arbitrary, the integrand in the equation has to vanish, i.e.

$$\frac{\partial \rho}{\partial t} + \nabla \cdot (\rho\mathbf{v}) = 0. \tag{2.2}$$

Equation (2.2) expresses the law of mass conservation in the usual local form. Moreover, most real fluids are approximately incompressible, and the relation $\mathrm{d}\rho/\mathrm{d}t = 0$ holds. Then, expressing the substantial derivative in terms of partial derivatives $d/dt = \partial/\partial t + \mathbf{v} \cdot \nabla$, we obtain

$$\frac{\mathrm{d}\rho}{\mathrm{d}t} \equiv \frac{\partial \rho}{\partial t} + (\mathbf{v} \cdot \nabla)\, \rho = \frac{\partial \rho}{\partial t} + \nabla \cdot (\rho\mathbf{v}) - \rho \nabla \cdot \mathbf{v}, \tag{2.3}$$

The conservation of mass [Eq. (2.2)] then implies that for incompressible fluids

$$\nabla \cdot \mathbf{v} = 0. \tag{2.4}$$

Equation (2.4) is the conservation of mass for an incompressible fluid.

2.2.1 Equation of motion of a fluid element

Let us next consider the conservation law for the momentum density $\rho\mathbf{v}$. The momentum of a fluid element of volume V_0, i.e. $\int_{V_0} (\rho\mathbf{v}) \mathrm{d}V$, is changed by the total force acting on it. This force, in the absence of external forces, is equal to the integral of the pressure over its surface $-\oint p d\mathbf{s}$. Again, applying Green's formula, we can transform the surface integral into a volume integral $\oint p \mathrm{d}\mathbf{s} = \int_{V_0} \nabla p \mathrm{d}V$, and write the conservation of momentum in its integral form as $(\mathrm{d}/\mathrm{d}t)[\int_{V_0} (\rho\mathbf{v}) \mathrm{d}V] = -\int_{V_0} \nabla p \mathrm{d}V$. The conservation of momentum in the local form becomes

$$\frac{\mathrm{d}\,(\rho\mathbf{v})}{\mathrm{d}t} = -\nabla p. \tag{2.5}$$

Because in this procedure we computed the change in momentum of a volume element by means of Newton's second law, the time derivative in Eq. (2.5) should be interpreted as the *substantial* derivative because it denotes the rate of change of momentum of a moving fluid particle. For convenience, let us rewrite the conservation of momentum

in the Eulerian coordinate system: the system which is fixed in space. In this frane of reference, the rate of change of momentum density is $\partial(\rho\mathbf{v})/\partial t$. Let us begin by expanding the substantial time derivative of the momentum density

$$\frac{\mathrm{d}}{\mathrm{d}t}(\rho\mathbf{v}) = \frac{\partial(\rho\mathbf{v})}{\partial t} + (\mathbf{v}\cdot\nabla)(\rho\mathbf{v}). \tag{2.6}$$

Then, using the law of mass conservation for an incompressible fluid ($\nabla\cdot\mathbf{v}=0$), we can transform the second term on the right hand side as

$$(\mathbf{v}\cdot\nabla)(\rho\mathbf{v}) = (\mathbf{v}\cdot\nabla)(\rho\mathbf{v}) + (\rho\mathbf{v})(\nabla\cdot\mathbf{v}) = \nabla\cdot(\rho\mathbf{v}\mathbf{v}) \tag{2.7}$$

and obtain the following expression equivalent to Eq. (2.6)

$$\frac{\mathrm{d}}{\mathrm{d}t}(\rho\mathbf{v}) = \frac{\partial(\rho\mathbf{v})}{\partial t} + \nabla\cdot(\rho\mathbf{v}\mathbf{v}). \tag{2.8}$$

By using Eq. (2.8), we can now write the law of momentum conservation Eq. (2.5) in the Eulerian coordinate system as

$$\frac{\partial(\rho\mathbf{v})}{\partial t} = -\nabla\cdot\mathbf{\Pi}, \tag{2.9}$$

where we defined

$$\mathbf{\Pi} = \rho\mathbf{v}\mathbf{v} + p\mathbf{I}, \tag{2.10}$$

or in Cartesian components

$$\Pi_{ik} = \rho v_i v_k + \delta_{ik} p. \tag{2.11}$$

By analogy with the mass flux, it is easy to recognize that $\mathbf{\Pi}\cdot\mathrm{d}\mathbf{s}$ represents the momentum flowing in a unit time through the surface element $\mathrm{d}\mathbf{s}$. The tensor $\mathbf{\Pi}$ is called the momentum flux tensor.

2.2.2 Viscous flows

Equation (2.11) represents a completely reversible transfer of momentum and is valid only for ideal fluids: fluids which do not dissipate momentum. However, real fluids do dissipate momentum. At a phenomenological level, this effect can be regarded as transport of momentum due to an irreversible mechanism. Therefore, we add an irreversible term into the momentum flux tensor, which we indicate as σ^i_{ik}

$$\Pi_{ik} = \rho v_i v_k + \delta_{ik} p - \sigma^i_{ik}. \tag{2.12}$$

In order to explicitly write σ^i_{ik}, we have to use phenomenological laws. One example of such a law is Newton's law of irreversible transfer of momentum among the fluid constituents,

$$\sigma^i_{ik} = \eta\left(\frac{\partial v_i}{\partial x_k} + \frac{\partial v_k}{\partial x_i}\right) \tag{2.13}$$

(where η is the shear viscosity), which postulates an irreversible transfer of momentum from particles with higher speed to particles with a lower one . The last two term in Eq. (2.12) are usually combined in the stress tensor $\sigma_{ik} = -\delta_{ik}p + \eta\left(\frac{\partial v_i}{\partial x_k} + \frac{\partial v_k}{\partial x_i}\right)$.

By substituting the irreversible momentum flux tensor in Eq. (2.12) and adding an external force (per unit volume) $\mathbf{F}^{ext}$ as another source of momentum change, we obtain the equation of motion for an incompressible Newtonian fluid

$$\frac{\partial(\rho v_i)}{\partial t} = -\frac{\partial}{\partial x_k}\left[\rho v_i v_k + \delta_{ik} p - \eta\left(\frac{\partial v_i}{\partial x_k} + \frac{\partial v_k}{\partial x_i}\right)\right] + F_i^{\text{ext}}. \tag{2.14}$$

By performing some basic algebra, we can rewrite this equation in the more familiar form

$$\frac{\partial(\rho \mathbf{v})}{\partial t} + \nabla\cdot(\rho \mathbf{v}\mathbf{v}) = -\nabla p + \eta\nabla^2\mathbf{v} + \mathbf{F}^{\text{ext}}, \tag{2.15}$$

or equivalently as

$$\rho\left[\frac{\partial \mathbf{v}}{\partial t} + (\mathbf{v}\cdot\nabla)\,\mathbf{v}\right] = -\nabla p + \eta\nabla^2\mathbf{v} + \mathbf{F}^{\text{ext}}. \tag{2.16}$$

This equation is the Navier-Stokes equation for an incompressible Newtonian fluid and, together with the equation $\nabla\cdot\mathbf{v} = 0$ is a compact way to write the conservation laws of mass and momentum, the incompressibility condition, and the phenomenological Newton's law for dissipative fluids.

2.2.3 Similarity laws of hydrodynamic phenomena

If two physical systems of different size obey the same equations, the systems are said to be "similar". In similarity theories one expresses a physical law only in terms of dimensionless variables and pure numbers. Then, in mathematical terms, two physical systems are considered similar when all the pure numbers are equal. In hydrodynamics, the most frequently used pure number is the Reynolds number, which is obtained by making the Navier–Stokes equation dimensionless.

Let us consider a viscous flow in a system whose units of length is l and express the steady state velocity through the unit of velocity U. We can then write the steady-state Navier-Stokes equation

$$\rho(\mathbf{v}\cdot\nabla)\,\mathbf{v} = -\nabla p + \eta\nabla^2\mathbf{v} + \mathbf{F}^{\text{ext}} \tag{2.17}$$

in terms of the dimensionless quantity $\mathbf{V} = \mathbf{v}/U$, and $\mathbf{R} = \mathbf{r}/l$ as

$$\rho\frac{U^2}{l}\mathbf{V}\cdot\nabla\mathbf{V} = -\frac{1}{l}\nabla p + \eta\frac{U}{l^2}\nabla^2\mathbf{v} + \mathbf{F}^{\text{ext}}. \tag{2.18}$$

The ratio of the term in the left hand side (the inertial term), to the second term in the right hand side (the viscous term) is of the order of $(\rho U l)/\eta$ which is the Reynolds number

$$Re = Ul\rho/\eta = Ul/\nu, \tag{2.19}$$

where $\nu = \eta/\rho$ is the kinematic viscosity of the fluid.

The Reynolds number is a measure of the relative importance of the inertia with respect to the viscosity and it determines the flow regime. When inertia dominates,

i.e. when the Reynolds number is large, we observe turbulence phenomena, which are outside the scope of this thesis. On the other hand, when the viscous terms dominates, and inertia is negligible, we are in the creeping flow regime. In this regime, the equation of motion becomes linear in the velocity and the hydrodynamic interaction becomes very strong. For colloids, the typical length scales ($l \sim 10^{-6}m$), velocities ($U \sim 10^{-3}m\,s^{-1}$) and viscosities ($\nu \sim 10^{-6}m^2\,s^{-1}$) are such that the Reynolds number is extremely low ($Re \sim 10^{-3}$), especially if one considers that the threshold for turbulence is a Reynolds number of $O(10^2$–$10^3)$.

Because this thesis regards largely colloidal systems, I only consider low Reynolds number flows where the term in the left hand side of Eq. (2.17) is negligible, and the steady-state Navier-Stokes equation simplifies to the Stokes equation

$$-\nabla p + \eta\nabla^2\mathbf{v} + \mathbf{F}^{\text{ext}} = 0, \tag{2.20}$$

plus the usual incompressibility condition $\nabla \cdot \mathbf{v} = 0$.

2.3 The Boltzmann equation

In the course of my education, I have been taught about the "dogma" of the atomistic theories in a way that led me to believe that this has never been under discussion, more or less since Democritus (excluding the weird and obscure era called the middle ages...). I was therefore much surprised to learn that most of Boltzmann's work was fiercely opposed by his contemporaries (just over one century ago!), even though people who studied Boltzmann's life acknowledge that his opponents were also a great source of motivation [5]. In devising his theory, Boltzmann wanted to clarify some important aspects of the second law of thermodynamics. Specifically he was concerned about the contradiction between the irreversibility implied by the second law of thermodynamics and the reversibility of the microscopic equation of motion of the small particles. While the authors of energetics solved this paradox by abandoning altogether the idea of atoms, Boltzmann developed a new statistical theory which showed that the second law of thermodynamics is valid only in a statistical sense. In order to achieve his goal, he donated to posterity his two masterpieces: the Boltzmann equation and the H-theorem. Far from hoping to give a rigorous or exhaustive description of Boltzmann's work, in this section I will pinpoint some aspects of the Boltzmann kinetic theory which have recently been exploited by the scientists who developed the lattice-Boltzmann method.

2.3.1 Basics of kinetic theories

Kinetic theories study the collective motion of a gas composed of a large number of molecules. Microscopically, each of them follows the classical equations of motion

$$\begin{cases} \dfrac{\mathrm{d}\mathbf{x}_i}{\mathrm{d}t} &= \dfrac{\mathbf{p}_i}{m} \\ \dfrac{\mathrm{d}\mathbf{p}_i}{\mathrm{d}t} &= \mathbf{F}_i \end{cases}, \tag{2.21}$$

(where i indexes the i^{th} molecule and m is the mass of the molecules). Because it is hopeless to solve Eqs. (2.21) for a number of molecules anywhere near to a realistic system, in kinetic theories this microscopic description is abandoned in favor of a statistical description of the system, and the main observable becomes the probability density $f(\mathbf{x}, \mathbf{p}, t)$ of finding a molecule around position $\mathbf{x}$, at time t, and with momentum $\mathbf{p}$. The equilibrium state is defined by the probability density f^e which is, by definition, unchanged by the collisions among the molecules, i.e.

$$\left(\frac{\mathrm{d}f^e}{\mathrm{d}t}\right)_{coll} = 0. \tag{2.22}$$

By means of an elegant reasoning, Maxwell was able to show that the distribution function

$$f^e = \frac{\rho}{m}\left(\frac{m}{2\pi k_{\mathrm{B}} T}\right)^{\frac{3}{2}} \exp\left(-\frac{mv^2}{2k_{\mathrm{B}} T}\right) \tag{2.23}$$

is a collisional invariant [in Eq. (2.23) v is the molecules speed, ρ is the fluid density, and k_B the Boltzmann constant]. However, Maxwell did not say how the distribution function f approaches the equilibrium condition. Boltzmann accomplished this mission by establishing the equation that bears his name. The molecules considered by Boltzmann are point sized and stream freely for most of the time, while occasionally undergoing instantaneous, binary collisions that drive them toward an equilibrium state. This mechanism is expressed concisely by the Boltzmann equation

$$\left[\frac{\partial}{\partial t} + \mathbf{v}\cdot\nabla\right] f(\mathbf{x}, \mathbf{v}, t) = \left(\frac{\mathrm{d}f}{\mathrm{d}t}\right)_{coll}. \tag{2.24}$$

With the assumption that the distribution functions of two molecules undergoing a collision are independent from each other, Boltzmann was able to show that the Maxwell–Boltzmann distribution, Eq. (2.23), is a steady solution of his equation. Furthermore, with his famous H-theorem

$$H(t) = -\int f \ln f \ \mathrm{d}\mathbf{v}\mathrm{d}\mathbf{x} \tag{2.25}$$

$$\frac{\mathrm{d}H}{\mathrm{d}t} \geq 0, \tag{2.26}$$

he proved that any initial distribution decays to the Maxwell–Boltzmann form.

The link of this kinetic theory to fluid dynamics is readily obtained. The hydrodynamic fields as density, momentum, and momentum flux are simply moments of the distribution function

$$\begin{aligned} \rho(\mathbf{x}, t) &= \int m f(\mathbf{x}, \mathbf{v}, t)\mathrm{d}\mathbf{v} \\ \mathbf{j}(\mathbf{x}, t) \equiv \rho(\mathbf{x}, t)\,\mathbf{v}(\mathbf{x}, t) &= \int (m\mathbf{v})\, f(\mathbf{x}, \mathbf{v}, t)\mathrm{d}\mathbf{v} \\ \mathbf{\Pi}(\mathbf{x}, t) &= \int (m\mathbf{v}\mathbf{v})\, f(\mathbf{x}, \mathbf{v}, t)\mathrm{d}\mathbf{v}. \end{aligned} \tag{2.27}$$

Because mass, and momentum are collisionally invariant, by making use of Eq. (2.24), we can show that the equilibrium hydrodynamic fields follow the equations

$$\begin{aligned} \frac{\partial \rho^e}{\partial t} + \nabla \cdot (\rho^e \mathbf{v}^\mathbf{e}) &= 0 \\ \frac{\partial (\rho^e \mathbf{v}^\mathbf{e})}{\partial t} + \nabla \cdot \mathbf{\Pi}^\mathbf{e} &= 0 \end{aligned} \tag{2.28}$$

The equilibrium part of the momentum flux tensor is, by using Eq. (2.23)

$$\mathbf{\Pi}^e = \frac{\rho k_B T}{m}\mathbf{I} + \rho \mathbf{v}\mathbf{v}, \tag{2.29}$$

which, for an ideal gas where $p = \rho k_B T/m$, is equivalent to the Eulerian form of the momentum-flux tensor. Therefore, Eqs. (2.28) are the Euler equation of hydrodynamics for an ideal, incompressible, isothermal fluid as we showed in Section 2.2.

The non-equilibrium part of the momentum flux

$$\mathbf{\Pi}^{neq} = -\frac{\rho k_B T \tau}{m}\left[\overline{\nabla \mathbf{v}} + \overline{\nabla \mathbf{v}}^t\right], \tag{2.30}$$

corresponds to the irreversible loss of momentum given by the Newton law [Eq. (2.13)] with the shear viscosity given by $\eta = (\rho k_B T \tau)/m$ [in Eq. (2.9) the bars indicates that the operators are made traceless and the "t" the transpose matrix].

2.4 Lattice Boltzmann equation

After having sketched the basics of the kinetic theory of Boltzmann, I will show how a similar approach has been developed for a lattice system. Initially, the reason for developing a lattice kinetic theory was that, because the continuum distribution function contains much more information than "only" hydrodynamics, it was hoped that the lattice counterpart of the Boltzmann equation would suffice to keep the hydrodynamic properties at a macroscopic level, while being much cheaper to solve numerically. While this ambitious program has mostly been abandoned, the lattice Boltzmann equation proved to be extremely relevant for the study of low-Reynolds-number hydrodynamics in complex geometries.

In the lattice Boltzmann equation [6, 7, 8], the distribution function $f(\mathbf{x}, \mathbf{v}, t)$ is substituted by a discrete version $f(\mathbf{r}, \mathbf{c}_i, t)$, usually written in the compact form $f_i(\mathbf{r}, t)$, which is the probability density of finding a particle at position $\mathbf{r}$, at time t, and with velocity $\mathbf{c}_i$. Here $\mathbf{r}$, $\mathbf{c}_i$, and t are discrete, while $f_i(\mathbf{r}, t)$ is continuous. The time evolution of the distribution function f_i is given by the lattice Boltzmann equation, which is written in analogy with Eq. (2.24) as

$$f_i(\mathbf{r} + \mathbf{c}_i, t + 1) = f_i(\mathbf{r}, t) + \Delta_i(n) \tag{2.31}$$

where Δ_i is the change in f_i due to the instantaneous collisions.

Following the analogy with the continuum kinetic theories, one needs to specify the form of the collision operator Δ_i, which will in turn specify the equilibrium distribution function $f^e(\mathbf{r}, t)$. By definition, the equilibrium distribution function is the

distribution which is left unchanged by the collision operator, i.e. $\Delta_i(f^e) = 0$. With his equation, Boltzmann showed that the equilibrium distribution is also the most probable one. Unfortunately, for the discrete Boltzmann equation, the most probable distribution function does not obey the Euler equation for hydrodynamics [9], mainly because it does not satisfy all the symmetry requirements. Hence, in order to recover hydrodynamic behavior at long times and large length scales, a completely different procedure is necessary.

Because we cannot use the most probable distribution density, we are forced to construct an approximate equilibrium distribution function. In the lattice Boltzmann method, such an approximate equilibrium distribution is expressed as a series expansion in powers of the flow velocity $\mathbf{u}$

$$f_i^e = \rho \left[a_0^i + a_1^i \mathbf{u}\cdot\mathbf{c}_i + a_2^i \overline{\mathbf{uu}} : \overline{\mathbf{c}_i\mathbf{c}_i} + a_3^i \mathrm{u}^2 \right], \tag{2.32}$$

where $\overline{\mathbf{uu}} = [\mathbf{uu} - (1/3)\, u^2\mathbf{I}]$ is the traceless part of $\mathbf{uu}$. Then, the coefficients are fixed by imposing that the hydrodynamic fields mass, momentum, and the equilibrium part of the stress tensor are moments of the *equilibrium* distribution function:

$$\begin{aligned} \rho(\mathbf{r},t) &= \sum_i f_i^e(\mathbf{r},t) \\ \mathbf{j}(\mathbf{r},t) &= \sum_i f_i^e(\mathbf{r},t)\mathbf{c}_i \\ \boldsymbol{\Pi}^e(\mathbf{r},t) \equiv p\mathbf{I} + \rho\mathbf{uu} &= \sum_i f_i^e(\mathbf{r},t)\mathbf{c}_i\mathbf{c}_i. \end{aligned} \tag{2.33}$$

These constraints may seem superfluous, because by definition the hydrodynamic fields are collisionally invariant, hence they should automatically be only functions of the equilibrium distribution function. However, the reader should not forget that our equilibrium distribution is obtained as a series expansion and is therefore an approximate one. In reality, by determining the coefficients of the expansion by imposing Eqs. (2.33), we make sure that the first moments of the equilibrium distribution density satisfy the Euler equations for an inviscid fluid.

Having fixed the functional form of the equilibrium distribution f_i^e, we need to define the collision operator Δ_i. In the following, I will refer to the enhanced collision operator first defined by Higuera *et. al.* [10, 7, 11] and later modified by Ladd [8]. Higuera *et al.* noted that if one is only interested in the Navier–Stokes equation at the hydrodynamic scale, the collision operator could be made very simple. Specifically, the collision operator can be constructed by linearizing about the local equilibrium

$$\Delta_i(f) = \Delta_i(f^e) + \sum_i \mathcal{L}_{ij}\left(f_j - f_j^e\right). \tag{2.34}$$

Because, by definition, $\Delta_i(f^e) = 0$, we need to determine only the linear operator $\mathcal{L}_{ij}$. It is remarkable that on a lattice this task can be performed analytically based solely on general symmetry considerations [7]. One way to obtain $\mathcal{L}_{ij}$ is via the spectral decomposition, i.e. by decomposing it as $\mathcal{L}_{ij} = \sum_k \lambda_k \mathrm{P}_{ij}^k$, where P_{ij}^k are the projector operators along the eigenvectors E_i^k, and λ_k are their corresponding

eigenvalues. Another, equivalent, way of determining $\mathcal{L}_{ij}$ is by directly imposing the conservation laws. The linear collision operator has to conserve the collision invariant quantities, i.e. it should satisfy $\Delta_i(\rho) = 0$, and $\Delta_i(\rho\mathbf{u}) = 0$; in addition the stress tensor has to decay isotropically. These conditions translates directly into the following eigenvalues equations

$$\begin{aligned} \sum_i \mathcal{L}_{ij} &= 0 \\ \sum_i \mathbf{c}_i \mathcal{L}_{ij} &= 0 \\ \sum_i \overline{\mathbf{c}_i \mathbf{c}_i} \mathcal{L}_{ij} &= \lambda \overline{\mathbf{c}_j \mathbf{c}_j} \\ \sum_i c_i^2 \mathcal{L}_{ij} &= \lambda_{\mathrm{B}} c_j^2. \end{aligned} \tag{2.35}$$

These equations, while making sure that the linear collision operator satisfy all the conservation relations required for hydrodynamic behavior of the systems, fix 10 eigenvalues. The remaining 8 eigenvalues, because they do not relate to physical observables, correspond to artificial conservation laws. Therefore, to ensure the fastest possible decay of these spurious modes, these eigenvalues are set to -1.

In summary, to solve the lattice Boltzmann equation Eq. (2.31), which we rewrite here

$$f_i(\mathbf{r} + \mathbf{c}_i, t + 1) - f_i(\mathbf{r}, t) = \Delta_i(n), \tag{2.36}$$

we perform a two step procedure. The first one is the collisionless streaming

$$f_i(\mathbf{r} + \mathbf{c}_i, t + 1) - f_i(\mathbf{r}, t) = 0, \tag{2.37}$$

which corresponds to the Liouville operator in the continuum limit. In practice, Eq. (2.37) is a simple propagation step where each density distribution f_i is moved to the site correspondent with the discrete velocity $\mathbf{c}_i$. The second step is the collision step that relaxes the non-equilibrium part of the distribution density (the equilibrium distribution function is collisionally invariant). After the collision has taken place, we obtain the after collision distributions $f_i' = f_i + \Delta_i(f)$. In principle, the post-collision distribution functions f_i' are computed by applying the collision operator $\mathcal{L}_{ij}$ as prescribed by Eq. (2.34). However, because we know the exact form of the collision operator (through its spectral decomposition), the simulation algorithm can be written directly in terms of the moments of the density distribution, ρ, $\mathbf{j}$, $\mathbf{\Pi^e}$, and the full $\mathbf{\Pi}$.

The post collision momentum flux tensor $\Pi^{'}$ can be computed according to [8]

$$\Pi^{'}_{\alpha\beta} = \Pi^{eq}_{\alpha\beta} + (1 + \lambda)\left(\overline{\Pi}_{\alpha\beta} - \overline{\Pi}^{eq}_{\alpha\beta}\right) + \frac{1}{3}(1 + \lambda_B)\left(\Pi_{\gamma\gamma} - \Pi^{eq}_{\gamma\gamma}\right)\delta_{\alpha\beta}, \tag{2.38}$$

and the post collision distribution functions are

$$f_i + \Delta_i(f) = \rho\left[a_0^i + a_1^i u_\alpha \cdot c_{i\alpha} + a_2^i \Pi^{'}_{\alpha\beta} : \overline{c_{i\alpha} c_{i\beta}} + a_3^i \mathrm{u}^2\left(\Pi^{'}_{\alpha\alpha} - 3\rho c_s^2\right)\right]. \tag{2.39}$$

By performing a multi-time-scale analysis [9], the shear viscosity of the fluid can be expressed in terms of the eigenvalue λ

$$\eta = -\frac{1}{6}\rho\left(\frac{2}{\lambda}+1\right). \tag{2.40}$$

By tuning the eigenvalue λ, we can change the shear viscosity of the fluid (within limits set by convergence). The eigenvalue λ_B is irrelevant for an incompressible fluid and can be safely set to -1[8].

2.4.1 Simplification for low Reynolds number

For low-Reynolds flows, the steady state Navier-Stokes equation (2.15) simplifies to the Stokes equation [Eq. (2.20), and $\nabla \cdot \mathbf{v} = 0$]. One way of solving these steady-state equations, is by computing the steady state of the linearized Navier-Stokes equations

$$\begin{array}{rcl} \partial_t \rho & = & -\nabla \cdot (\rho \mathbf{u}), \\ \partial_t (\rho \mathbf{u}) & = & -\nabla p + \eta \nabla^2 \mathbf{u} + \mathbf{F}^{ext}. \end{array} \tag{2.41}$$

Ladd [8] shows that in order to fulfill the conservation laws implicit in Eqs. (2.41), it is sufficient to use a simpler form for the equilibrium distribution function

$$f_i^e = \rho\left[a_0^i + a_1^i \mathbf{u}\cdot\mathbf{c}_i\right]. \tag{2.42}$$

Moreover, by fixing $\lambda = -1$, corresponding to a shear viscosity $\eta = \rho/6$ [cf. Eq. (2.40)], the simulation algorithm is greatly simplified and the post collision distribution density is simply

$$f_i + \Delta_i(f) = \rho\left[a_0^i + a_1^i u_\alpha \cdot c_{i\alpha}\right]. \tag{2.43}$$

2.4.2 Bounce-back rule for a suspension of colloids

To have interesting flows at low Reynolds number, macroscopic objects must interact with the fluid. These macroscopic objects will act on the fluid as a boundary condition which will exchange momentum with the fluid, thus creating non-trivial flow patterns. At contact with the macroscopic objects, the appropriate boundary conditions have to be imposed, typically the non-slip boundary condition, where the fluid has the same velocity of the macroscopic particle.

In the lattice Boltzmann method, the first issue that needs to be addressed is how to map a continuum object (a wall or a colloid for example) on a lattice. Ladd [8] showed that placing these boundary nodes in the middle of the links connecting the interior of the object with the exterior region provides a useful recipe that obeys momentum conservation and best lattice resolution of the macroscopic object; without introducing involved and expensive more precise second- or higher-order schemes. Figure 2.1 shows a cartoon of the mapping procedure of an arbitrarily shaped object placed on a two dimensional lattice. At the boundary nodes the so-called bounce-back procedure is applied [8]. This procedure prescribes that, during the propagation step (at half a time step), the incoming distributions f_i are reflected back. Specifically, if i and i'

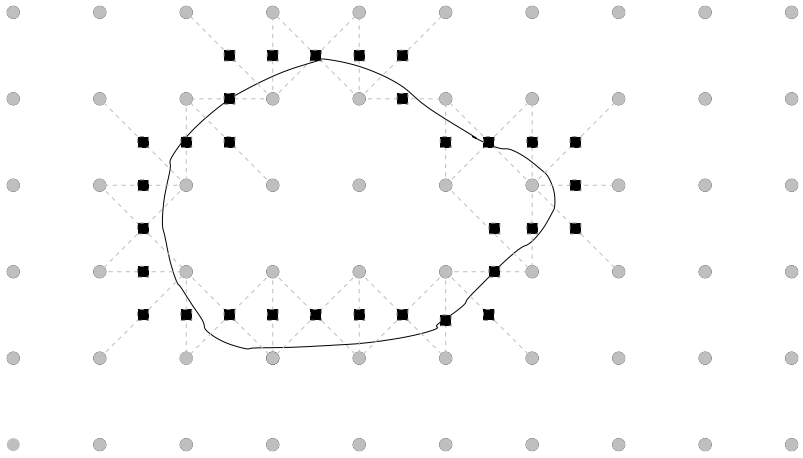

Figure 2.1: Mapping procedure. First, one draw on top of the lattice nodes (light gray spheres) the actual shape of the macro particle (continuum black line). Then one should identify all the links connecting an internal node with an external one (dashed light gray line). The lattice representation of the macroscopic particle will be given by the collection of the midpoints of the identified links (black squares).

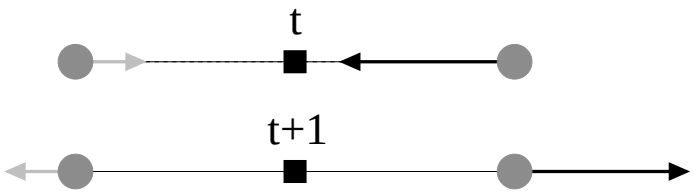

Figure 2.2: Bounce back rule.

refer to oppositely directed velocities, and, at site $\mathbf{r}$, the link along the velocity $\mathbf{c}_i$ is a boundary link, the following rules apply [See Fig. (2.2)]

$$\begin{aligned} f_{i'}(\mathbf{r}, t+1) &= f_i(\mathbf{r}, t), \\ f_i(\mathbf{r}+\mathbf{c}_i, t+1) &= f_{i'}(\mathbf{r}+\mathbf{c}_i, t). \end{aligned} \tag{2.44}$$

This procedure is correct if the macroscopic obstacle is at rest and acts as a momentum sink as, for example, a wall or a porous medium.

If, on the other hand, the obstacle is in motion, one has first to compute the velocity of the solid body located at the link $\mathbf{u}_l$, which is given by the well known formula for

the velocity of a point of a rigid body

$$\mathbf{u}_l = \mathbf{U} + \Omega \times \left(\mathbf{r} + \frac{1}{2}\mathbf{c}_i - \mathbf{R} \right), \tag{2.45}$$

where $\mathbf{R}$ is the center of mass of the solid body and $\mathbf{U}$ and $\mathbf{\Omega}$ are the solid-body velocity and angular velocity, respectively. In this case, Eqs. (2.44) must include the momentum exchange with the particle

$$\begin{aligned} f_{i'}(\mathbf{r}, t+1) &= f_i(\mathbf{r}, t) - 2a_1^i \rho \mathbf{u}_b \cdot \mathbf{c}_i, \\ f_i(\mathbf{r} + \mathbf{c}_i, t+1) &= f_{i'}(\mathbf{r} + \mathbf{c}_i, t) + 2a_1^i \rho \mathbf{u}_b \cdot \mathbf{c}_i. \end{aligned} \tag{2.46}$$

The sum of all the moment exchanged with the fluid should be applied back to the suspended particle, to ensure overall momentum conservation.

Note that Eqs. (2.46) imply that the lattice nodes inside the particle have the same property as the external region. In particular the fluid should be placed also inside the colloid. Moreover, the bounce-back rule allows for a leakage of mass density in and out of the macroscopic particle. Although these may seem weird conditions, for simple fluids the transport coefficients of the suspended colloids are correct, provided that one takes care of the few spurious correlations in, for example, the velocity autocorrelation function induced by the internal fluid [12, 13].

However, this behavior is not acceptable when there is a difference in the composition of the interior of the particle and its environment. An example of most relevance for this thesis is a charged colloid, which attracts a cloud of oppositely charged ions. Eqs. (2.46), would lead to an unphysical change in the charge of the colloid driven by momentum exchanges. If one wants to deal with such systems, one should eliminate this spurious effect. In this thesis, we exploited as much as possible the Galilean invariance of the systems. This allowed us to use a reference system fixed on the colloid, and keep the charged object at rest, thus avoiding this complication.

2.4.3 Lattice Boltzmann method in a nutshell

After this brief introduction of the theoretical basis of the lattice Boltzmann method, I will show how the computer simulation is implemented.

First of all, one must choose the underlying lattice, which must fulfill symmetry constraints. Useful lists of lattices are given by Qian [14] and Frisch *et al.* [9]. Throughout this thesis I used the so-called D3Q18 lattice [15, 8], where the "3" refers to the dimensionality and the "18" to the number of links per site, and which is defined by the following set of discrete 18 velocities $\{\mathbf{c}_i\}$,

$$\begin{array}{ccc} \mathbf{c}_{1,2} = (\pm 1, 0, 0), & \mathbf{c}_{3,4} = (0, \pm 1, 0), & \mathbf{c}_{5,6} = (0, 0, \pm 1), \\ \mathbf{c}_{7,\ldots,10} = (\pm 1, \pm 1, 0), & \mathbf{c}_{11,\ldots,14} = (\pm 1, 0, \pm 1), & \mathbf{c}_{15,.,18} = (0, \pm 1, \pm 1). \end{array} \tag{2.47}$$

In Equations (2.47) 6 velocities have speed $c_i \equiv |\mathbf{c}_i| = 1$, and 12 have speed $c_i = \sqrt{2}$. The six velocities of speed 1 are counted twice; an inheritance from the four dimensional face-centered hyper-cubic lattice (FCHC), from which, by a projection

onto 3D, the D3Q18 is generated [15]. Another widely used lattice in three dimensions is the D3Q19 which adds an extra distribution density f_i with speed 0 and velocity $\mathbf{c}_{19} = (0, 0, 0)$. Depending upon the specific system under study, there are also other useful lattices with different sets of velocities.

Next, one should specify the form of the equilibrium distribution and of the collision operator and compute the coefficients of its expansion in the flow velocity $\mathbf{u}$. Because I exclusively considered low Reynolds number flows, I could use the simplified form [Eq. (2.42)]. For the D3Q18 lattice, the coefficients of the expansion are

$$\begin{array}{llll} a_0^i = \frac{1}{12}, & a_1^i = \frac{1}{6}, & i = 1, .., 6 \\ a_0^i = \frac{1}{24}, & a_1^i = \frac{1}{12}, & i = 7, .., 18 \end{array} \tag{2.48}$$

Equations (2.48) implies a sound speed $c_s^2 = 1/2$, which is a suitable value to ensure stability of the simulation.

We are left with the last step in the preparation of the computer simulation, namely the mapping of the colloid(s) onto the lattice, by identifying all the links which connect the interior of the colloids with the exterior. Along these links, during the propagation step the bounce-back rule will be applied (see Figs. 2.1 and 2.2).

Now, everything is ready to start the time evolution of the lattice-Boltzmann simulation which will lead to the steady state of Eq. (2.41). The algorithm of a lattice Boltzmann simulation is divided in three steps: computation of the post-collision distribution densities f_i's [for low Re by means of Eq. (2.43)], their propagation with the application of the bounce back rule, and the re-computation of the hydrodynamic fields (at low Re and shear viscosity 1/6 only ρ and $\mathbf{u}$ are needed).

After all this work, one should have a basic (hopefully) working lattice Boltzmann method.

3 Introduction to electrokinetics

3.1 The Poisson–Boltzmann equation and the electric double layer

Consider an electrolyte composed of k species of positive and negative ions dissolved in a neutral fluid. The ions create an electric field $\mathbf{E}(\mathbf{r}) = -\nabla\Phi(\mathbf{r})$, where $\Phi(\mathbf{r})$ is the electrostatic potential which, if we denote by $q(\mathbf{r})$ the charge density due to the ions, can be computed using the Poisson equation

$$\nabla^2\Phi(\mathbf{r}) = -\frac{4\pi q(\mathbf{r})}{\epsilon}, \tag{3.1}$$

where ϵ is the dielectric constant of the (overall) neutral medium. If the electrostatic potential is not constant, the ions of species k are subject to the electrostatic force $\mathbf{F} = z_k e\mathbf{E}$, where z_k is their valency (with charge sign) and e is the elementary charge. The effect of this electric force is counteracted by the thermal motion of the ions. A convenient way [16, 17, 18, 19, 20], [21, 22] to take the thermal equilibrium into account is to write the equilibrium distribution density of the ions as a Boltzmann equilibrium (which implies point sized ions)

$$n_k(\mathbf{r}) = n_0 \exp(-z_k e\Phi(\mathbf{r})/k_B T). \tag{3.2}$$

For specificity, let us consider a two species system. The charge density is then expressed in terms of the probability distributions of the two species

$$q(\mathbf{r}) = e\left(z_+ n_+(\mathbf{r}) + z_- n_-(\mathbf{r})\right). \tag{3.3}$$

In order to obtain a closed expression for the electrostatic potential, we can substitute Eq. (3.3) into Eq. (3.1) to get

$$\nabla^2\Phi(\mathbf{r}) = -\frac{4\pi e}{\epsilon}\left(z_+ n_+(\mathbf{r}) + z_- n_-(\mathbf{r})\right). \tag{3.4}$$

Finally, let us substitute Eq. (3.2) into Eq. (3.4) to obtain the so-called Poisson Boltzmann equation (PB) which, for a symmetric electrolyte (i.e. $z_+ = -z_- = z$), reads

$$\nabla^2\Phi(\mathbf{r}) = \frac{8\pi e z n_0}{\epsilon}\sinh\left(ez\Phi(\mathbf{r})/k_B T\right). \tag{3.5}$$

Unfortunately, solutions for this non-linear equation are only available for very simple geometries. However, if the electric potential is small, in other words if $e\Phi(\mathbf{r})/k_B T \ll$

1, the approximation $\exp(\pm ze\Phi(\mathbf{r})/k_BT) \simeq 1 \pm ze\Phi(\mathbf{r})/k_BT$ holds, and Eq. (3.5) is simplified by the linearized Poisson-Boltzmann equation (LPB)

$$\nabla^2\Phi(\mathbf{r}) = \frac{8\pi e^2 z^2 n_0}{\epsilon k_B T}\Phi(\mathbf{r}) = \kappa^2\Phi(\mathbf{r}), \tag{3.6}$$

which can be solved analytically for many interesting geometries. In Equation (3.6), note that $\kappa = \sqrt{8\pi e^2 z^2 n_0/\epsilon k_B T}$ has the dimension of an inverse length.

Let us now introduce a charged macroscopic particle in the electrolyte. The equilibrium density of microions in solution will still be given by Eq. (3.5), where now the macroscopic particle enters via a boundary condition for the electrostatic potential $\Phi(\mathbf{r})$. This equation, again, cannot be solved in general. Hence, to make it tractable, one must restrict the study to the case of small surface potentials (in other words, to weakly charged particles), in which the linearized Poisson-Boltzmann equation (3.6) provides a reasonable approximation. For simplicity, let us consider the case of a spherical macroscopic particle.

Intuitively, the like-charged microions (in the remainder *coions*) will be repelled, while the oppositely charged microions (*counterions*) will be attracted toward the sphere. While the electrostatic interaction favors an infinitesimally thin layer of counterions, which will immediately screen the charge of the sphere, entropy will prevent the counterions from condensing on the sphere. As a balance of the two forces, one could expect a cloud of counterions surrounding the sphere until the charge of the sphere is fully screened. Far beyond this length, called the Debye screening length, the sphere appears neutral. The layer of microions is usually referred to as the electric double layer (EDL). It is the presence of inhomogeneity and EDL that causes the distinctive electrostatic and hydrodynamic effects called electrokinetic phenomena, which I will briefly introduce below. For a rigorous description of the equilibrium distribution of the microions in terms of their free energy, I refer the reader to the book of Verwey and Overbeek [21].

Quantitative predictions for the co- and counterion equilibrium-density-distributions are given by the Debye-Hückel theory [19, 20]. In their theory, Debye and Hückel assume that the electrostatic potential is much smaller than k_BT. Hence, instead of the full Poisson-Boltzmann equation, they use the approximate linearized Poisson-Boltzmann equation (3.6) for computing the electrostatic potential and, via Eq. (3.2), the co- and counterions equilibrium distributions.

For a sphere of radius a, Eq. (3.6) can be easily solved to give the Yukawa potential

$$\Phi(r) = \Phi_0 \frac{a}{r} e^{-\kappa(r-a)}, \tag{3.7}$$

where r originates at the sphere center and $\Phi_o = \Phi(0)$ is the electrostatic potential at contact with the sphere. By substituting the Yukawa potential into the linearized version of Eq. (3.2), the concentrations of co- and counterions are, respectively,

$$\begin{aligned} n_+(\mathbf{r}) &= n_0\left(1 - \frac{ez\Phi_0}{k_BT}\frac{a}{r}e^{-\kappa(r-a)}\right) \\ n_-(\mathbf{r}) &= n_0\left(1 + \frac{ez\Phi_0}{k_BT}\frac{a}{r}e^{-\kappa(r-a)}\right). \end{aligned} \tag{3.8}$$

The counterion cloud in the vicinity of the charged sphere decays faster than exponentially over a distance of the order of $\lambda_D = \kappa^{-1}$, the Debye screening length. The coions, on the other hand, are expelled from the vicinity of the sphere and reach the bulk value with the same functional dependence. The symmetry of co- and counterions with respect to the bulk concentration [showed by Eq. (3.8)] is a typical signature of the validity of the Debye-Hückel approximation. The electrostatic potential at contact Φ_0 is usually named the zeta potential ζ. In electrokinetic phenomena, the relevant parameter is the relative size of the macroscopic particle to the extension of the EDL. Therefore, the Debye screening length λ_D is the appropriate unit of length, and the electrokinetic phenomena are conveniently described in terms of the dimensionless length κa.

In this description of the diffuse layer, I disregarded the so-called Stern layer [23, 24]. However, because this layer is thought to be inside the non-slip region of the fluid [23, 24], it is believed that it does not influence the hydrodynamic interactions with the fluid. It is possible to consider this layer as part of the sphere and model the system simply as an effective sphere plus an electric diffuse layer. Throughout this thesis I shall not consider the effect of a dynamic Stern layer, i.e. a Stern layer whose counterions are not glued on the particle surface but are free to move.

3.2 Electrokinetic phenomena

The term "Electrokinetic phenomena" refers to all phenomena in which the EDL is distorted from its equilibrium position via an external force, of electrical or other origin. Because of this distortion, the EDL reacts and consequently induces a relative motion between the suspended particles and the fluid. Many electrokinetic phenomena have been reported in the literature, but they can be grouped into two categories depending upon the nature of the perturbing force. On the one hand we have electrophoresis, where the macroscopic charged particle and its EDL are displaced by means of an electric field—here the specific particle velocity is due to the balance between the direct electrostatic interaction and the hydrodynamic friction, plus the counter-reaction of the EDL, which has the opposite charge. On the other hand, in a sedimenting sample, the driving force is gravitational and, because of the relative motion between the particles and the electrolyte, a local electric field is generated. The so-called sedimentation potential is the experimentally measured electrostatic potential difference between the top and the bottom of a sedimenting sample.

In both cases, the macroparticles move. If, instead, the macroscopic objects are fixed, as, for example walls, slits, or a fixed obstacles, there are two equivalent electrokinetic phenomena. If an electric field is applied to, for example, a charged slit containing an electrolyte, the fluid will start moving generating a quasi plug flow. Although this phenomenon is called electro-osmosis, the physics is essentially the same as in electrophoresis due to Galilean invariance. If, instead, we displace the electrolyte in a charged porous medium by means of (for example) a pressure gradient, we will measure an electrostatic potential difference between the two sides, called the "streaming potential". Again, a second of thought will show the equivalence of this potential with the sedimentation potential.

For more details I refer the reader to the vast literature present; for a general introduction see, for example, [3, 25, 2], for a mascript focused on colloidal suspensions see [23, 26], and for a nice recent review of the recent achievements see [24].

3.2.1 Onsager relation

In the previous section, I divided the electrokinetic phenomena into two categories. As the careful reader already suspects, there is a close relation also among the two basic electrokinetic phenomena. In one case, we displace the (overall neutral) fluid by means of an electric field; in the other, we generate an electrostatic potential by displacing particles (which together with the EDL are, again, neutral). This symmetry finds its formalization in an Onsager relation. For charged particles, the mass current J_M is generated by two mechanisms: a force $\mathbf{G}$ which acts onto the particles because they have a mass, and the electrostatic forces $\mathbf{E}$ that displace mass because particles posses charge. Conversely, the electric current J_e is generated by the action of a direct, electrostatic, force plus a non electrostatic force that, by displacing the charged particles, also contributes to the electric current. More formally

$$\begin{aligned} J_M &= \mathcal{A}\mathbf{G}+\mathcal{L}_{ge}\mathbf{E} \\ J_e &= \mathcal{B}\mathbf{E}+\mathcal{L}_{eg}\mathbf{G}, \end{aligned} \tag{3.9}$$

where $\mathcal{A}$, $\mathcal{B}$, and $\mathcal{L}_{ge}$ and $\mathcal{L}_{eg}$ are the relevant transport coefficients. The symmetry of the electrokinetic phenomena is formalized by the equality $\mathcal{L}_{eg} = \mathcal{L}_{ge}$.

3.2.2 Sedimentation velocity

Below, I briefly review the classical theories for sedimentation and electrophoresis. In a sedimentation experiment, charged colloids sediment under the influence of the gravitational force. The sedimentation velocity of a charged sphere (for example) is slightly less than that of a neutral one of the same size and weight because, while sedimenting, a charged sphere has to drag the (distorted) electrical double layer along. The amount of friction exerted by the EDL depends upon its spatial extension (measured by the dimensionless length κa, where a is the radius of the spheres) and upon the total charge of the sphere. In the two limits $\kappa a \to 0$, and $\kappa a \to \infty$ the EDL exerts no extra friction. In the first case, the EDL is extremely diffuse and, because in this limit the Yukawa potential reduces to a constant, the electrostatic potential exerts no force. In the second case, the layer is so thin and so close to the colloid that the no-slip boundary condition prevents any force generation. For intermediate values of κa the EDL, distorted by the flow field near the particle, will try to restore its equilibrium shape. In doing so, the EDL exerts a force on the fluid which opposes the perturbing, gravity, force; hence it will reduce the sedimentation velocity.

Booth [27] and later Ohshima [28] gave analytical formulae for the reduction of the sedimentation velocity $U(Z)/U_0$ in the limit of a single weakly-charged spherical colloid. In this limit, they predict that the sedimentation velocity, $U_0(Z)$ can be expressed as

$$\frac{U_0(Z)}{U_0} = 1 - c_2 Z^2, \tag{3.10}$$

where U_0 is the sedimentation velocity of a neutral sphere, and c_2 is a constant that can be computed analytically in the Debye-Hückel limit. For monovalent co- and counterions, i.e. when $z_+ = -z_- = 1$, which also have the same diffusivity, $D_+ = D_- = D$, the expression for c_2 is

$$c_2 = \frac{k_B T l_B}{72\pi a^2 \eta D} f(\kappa a), \tag{3.11}$$

where $f(\kappa a)$ is the following function

$$\begin{aligned} f(\kappa a) \quad = \quad & \frac{1}{1+(\kappa a)^2}\Big[\mathrm{e}^{2\kappa a}\left(3E_4(\kappa a) - 5E_6(\kappa a)\right)^2 + 8\mathrm{e}^{\kappa a}\left(E_3(\kappa a) - E_5(\kappa a)\right) \\ & -\mathrm{e}^{2\kappa a}\left(4E_3(2\kappa a) + 3E_4(2\kappa a) - 7E_8(2\kappa a)\right)\Big] \end{aligned} \tag{3.12}$$

of the integral functions

$$\mathrm{E}_n(x) = x^{n-1}\int_x^\infty dt\; t^{-n}\exp(-t). \tag{3.13}$$

In the remainder of this thesis we repeatedly refer to this theory.

3.2.3 Electrophoresis

When charged spheres are immersed in an electrolytic solution in the presence of an external electric field, they begin to move under the effect of the electrostatic force. For a quantitative prediction of the translational velocity, one needs to explicitly consider the combined effect of the electric double layer and of hydrodynamics. Again, analytical formulae were obtained in the two limiting scenarios $\kappa a \to 0$, and $\kappa a \to \infty$. As we already observed in the sedimentation case, for $\kappa a \to 0$ the EDL does not couple with the external electric field and the electrophoretic mobility is given by the ratio of the electrostatic force $Q\mathbf{E}$ (acting directly onto the particle) to the Stokes drag $\xi = 6\pi\eta a$ and to the driving electric field $\mathbf{E}$. The electrophoretic mobility is then simply

$$\mu_e = \frac{Q}{6\pi\eta a}, \tag{3.14}$$

which, in terms of the the zeta potential ζ (i.e. the electrostatic potential at contact) reads:

$$\mu_e = \frac{2}{3}\frac{\epsilon}{\eta}\zeta. \tag{3.15}$$

This result was first derived by Hückel in 1924 [29]. In 1903, von Smoluchowski [30] showed that in the opposite limit, i.e. when $\kappa a \to \infty$, the electrophoretic mobility is increased by a factor 3/2

$$\mu_e = \frac{\epsilon}{\eta}\zeta. \tag{3.16}$$

Remarkably, the Smoluchowski result is valid regardless of the shape of the macroscopic particle and it is used daily in hundreds of laboratories in the world for separating many biologically relevant particles. Phenomenological descriptions of these results can be found in text books and reviews [25, 31, 32].

3.3 Electrokinetic equations

In order to provide the general framework for the description of electrolyte dynamics, I first briefly review the dynamics of dilute mixtures—of which electrokinetic phenomena are a sub set—on hydrodynamic length and time scales. As in all hydrodynamic descriptions, the starting point of this discussion lies in the laws of conservation of mass and momentum.

3.3.1 Mass conservation

Every species of the fluid mixture satisfies the usual mass conservation law:

$$\frac{\partial \rho_k}{\partial t} + \nabla \cdot \rho_k \mathbf{v}_k = 0, \tag{3.17}$$

where $\mathbf{v}_k$ is the velocity and ρ_k the density distribution of the species labeled by k. The total density, $\rho = \sum_k \rho_k$, is also conserved, and satisfies an equation analogous to Eq. (3.17) with respect to the barycentric velocity $\rho\mathbf{v} = \sum_k \rho_k \mathbf{v}_k$, which describes the evolution of a fluid element. If we refer the motion of all species to this common velocity, then Eq. (3.17) can be expressed as

$$\frac{\partial \rho_k}{\partial t} + \nabla \cdot \rho_k \mathbf{v} = -\nabla \cdot \mathbf{j}_k, \tag{3.18}$$

where I have introduced the relative current of species k, $\mathbf{j}_k = \rho_k(\mathbf{v}_k - \mathbf{v})$, which accounts for all dynamical effects arising from the mismatch in velocities between the different species. For mixtures composed of molecular constituents at low Reynolds number (as is usually the case in electrolytes), the inertial time scale is extremely small; hence the relative current can be assumed proportional to a thermodynamic driving force, which is proportional to the gradient of the chemical potential. As a result, the relative current of species i becomes diffusive and can be expressed as [33]

$$\mathbf{j}_k = -\sum_k D_{ik} \rho_k \nabla \beta\mu_k, \tag{3.19}$$

where β is $1/k_B T$, with k_B the Boltzmann constant and T the temperature. $\beta\mu_k = \log \rho_k + \beta\mu_k^{ex}$ is the chemical potential decomposed into an ideal and excess part, while D_{ik} corresponds to the diffusion coefficient that determines the flux of species i induced by spatial variations in the chemical potential of species k. For the sake of simplicity, I focus on the case where cross diffusion is neglected, and hence $D_{ik} = D_i \delta_{ik}$. By substituting the chemical potential in Eq. (3.19), I express mass conservation in the form of a set of convection-diffusion equations, expressing the two mechanisms that control density evolution for each species,

$$\frac{\partial \rho_k}{\partial t} + \nabla \cdot \rho_k \mathbf{v} = \nabla \cdot D_k \left[\nabla \rho_k + \rho_k \nabla \beta\mu_k^{ex} \right]. \tag{3.20}$$

3.3.2 Momentum conservation

Next, let us consider momentum conservation. On the same length and time scales, as I have already shown in Section 2.2.1, momentum conservation implies that the barycentric velocity, for low Reynolds number flows, follows the linearized Navier-Stokes equation,

$$\frac{\partial}{\partial t}\left(\rho\mathbf{v}\right) = \eta\nabla^2\mathbf{v} - \nabla p + \mathbf{F}^{ext}, \tag{3.21}$$

where η is the shear fluid viscosity, while $\mathbf{F}^{ext}$ is an external force density acting on a fluid element. The effect of the interactions among the different species enters as a net force acting on the fluid expressed as the gradient of the local pressure p. In the presence of spatial gradients, the pressure has in general a tensorial character, and can be derived from the free energy of the system. However, for ideal electrolytes, the local pressure can always be expressed as a scalar. Hence, for the sake of simplicity, we will consider this situation in what follows.

In general, the pressure gradient can be computed from the chemical potential as

$$\beta\nabla p = \sum_k \rho_k \beta\nabla\mu_k = \sum_k \left(\nabla\rho_k + \rho_k\beta\nabla\mu_k^{ex}\right) \tag{3.22}$$

and acts as a force. The first term of the pressure corresponds to the ideal-gas contribution, $\beta p^{id} = \sum_k \rho_k$ while the other two contain all the information of the interactions among the fluid species. If there is one majority neutral component, which only contributes to the ideal part of the pressure, then the excess component of the pressure can be identified as the osmotic pressure of the mixture.

Using Eq. (3.22) for the pressure gradient, the Navier-Stokes equation reads

$$\frac{\partial}{\partial t}\left(\rho\mathbf{v}\right) = \eta\nabla^2\mathbf{v} - \nabla p^{id} - \sum_k \rho_k\nabla\mu_k^{ex} + \mathbf{F}^{ext}. \tag{3.23}$$

3.3.3 Electrokinetic equations

The electrostatic equations can be computed as a special case of Eqs. (3.20) and (3.23) by replacing $\mu_k^{ex} = z_k e\Phi$, where z_k is the valency of the charged species k, and Φ is the electrostatic potential. The Smoluchowski equation (3.20) becomes

$$\frac{\partial\rho_k}{\partial t} + \nabla\cdot\rho_k\mathbf{v} = \nabla\cdot D_k\left[\nabla\rho_k + e\beta z_k\rho_k\nabla\Phi\right], \tag{3.24}$$

while the Navier–Stokes equation (3.23) is

$$\frac{\partial}{\partial t}\left(\rho\mathbf{v}\right) = \eta\nabla^2\mathbf{v} - \nabla p^{id} - \sum_k e z_k\rho_k\nabla\Phi + \mathbf{F}^{ext}. \tag{3.25}$$

We still need an additional equation that prescribes how the electrostatic potential is related to the local charge density. Since transport processes associated to mass and

momentum transfer in fluid mixtures are much slower than the propagation of electromagnetic waves, the electric field is completely determined by the Poisson equation

$$\nabla^2 \Phi = -\frac{4\pi e}{\epsilon} \left[\sum_{k=\pm} z_k \rho_k + \rho_s \right], \tag{3.26}$$

where ρ_s is for the charge density of the solid surfaces and accounts for possible confining walls or moving suspended particles in the electrolyte.

4 Velocity fluctuations and dispersion in a simple porous medium

Abstract

We model a fluid-filled disordered porous medium by a lattice-Boltzmann system with randomly broken links. The broken links exert a friction on the fluid without excluding volume. Such a model closely mimics the idealized picture of a porous medium, which is often used in the theoretical analysis of hydrodynamic dispersion. We find that the Brinkman equation describes both the mean flow characteristics and the spatial decay of velocity fluctuations in the system. However, the temporal decay of the velocity correlations (that a particle experiences as it moves with the fluid), cannot be simply related to the spatial decay. It is this temporal decay that determines the dispersivity. Thus, hydrodynamic dispersion is generally greater than theories based on spatial correlations would imply. This is particularly true at high densities, where such theories considerably underestimate both the magnitude and transient time scale for dispersion. Nonetheless, temporal velocity correlations are still ultimately screened and the hydrodynamic dispersion coefficient converges exponentially. The long-lived transients reported for more realistic systems must therefore be due explicitly to the presence of excluded volume.

4.1 Introduction

When a tracer particle is introduced into a stationary fluid, it will be dispersed by Brownian motion. The dispersion can be characterized by the mean of the squared displacement in a given direction, Δx^2. From the Einstein definition of the self-diffusion coefficient D_0, this increases linearly with time, the constant of proportionality being twice D_0,

$$\left\langle \Delta x^2(t) \right\rangle = 2D_0 t \tag{4.1}$$

For a stationary fluid filling the voids in a (nonadsorbing) porous medium, the motion of the tracer particles is hindered by the medium and the diffusion coefficient of the tracer particles is reduced relative to D_0. If, on the other hand, the fluid flows through the porous medium with a mean velocity $\overline{V}$, then the dispersion of tracer particles (now defined by the variance in their displacements) increases and can become very large compared to $2D_0 t$ at a given time. The origin of this "hydrodynamic" dispersion lies in the fact that, even in the absence of Brownian motion, different particles experience different local flow velocities and are, therefore, transported by convection over

different distances in a given time t. Quantitatively, the dispersion coefficient D is related to the time integral of the time correlation function of the velocity fluctuations experienced by tracer particles:

$$D = \int_0^\infty \langle \left[v_i(0) - \overline{V}\right] \left[v_i(t) - \overline{V}\right] \rangle dt \tag{4.2}$$

where $v_i(t)$ is the instantaneous velocity of a particle along the flow direction as it moves through the fluid. Note that we follow convention here and refer to the *diffusion* coefficient for the equilibrium case (where there is no flow), and to the *dispersion* coefficient for the non equilibrium case (where the fluid flows). The relative importance of this convective dispersion, relative to simple diffusion, can be characterized by the Peclet number Pe. It is defined as $Pe = U^* l^*/D_0$, where U^* is a characteristic velocity and l^* is a characteristic length. The obvious choice for the characteristic velocity U^* is the mean velocity of the fluid $\overline{V}$. At high Peclet numbers, tracer transport over distances larger than l^* is dominated by convection, and dispersion is therefore dominated by the spatial fluctuations in fluid velocity. Conversely, at low Peclet numbers, the convective contribution is small and simple diffusion dominates

In order to understand hydrodynamic dispersion, we need an idea of how fluid flows in porous media. If the fluid is Newtonian, then the steady-state velocity fields $\mathbf{v}$ will be solutions of the time-independent Navier-Stokes equations

$$\begin{aligned} -\nabla p + \eta \nabla^2 \mathbf{v} + \mathbf{F} &= 0 \\ \nabla \cdot \mathbf{v} &= 0. \end{aligned} \tag{4.3}$$

that satisfy stick boundary conditions at the solid/fluid interface. Here p is pressure, $\mathbf{F}$ is any external forces acting on the fluid, and η is the viscosity. We have also assumed that inertia is negligible (the flow is at low Reynolds number). The relation between the steady-state flow velocity and the applied pressure gradient is then given by the Darcy's law,

$$\overline{V} = -\frac{\kappa}{\eta} \nabla p, \tag{4.4}$$

where κ is a constant (the permeability) that depends only on the properties of the porous medium, not on those of the fluid. Equation (4.4) is a first-order equation while Eqs. (4.3) are second-order equations. It is therefore impossible to formulate rational boundary conditions between the two. In 1947 Brinkman proposed an equation to describe the locally averaged flow in a porous media that is, the flow on a scale large compared to any local inhomogeneity in the medium [34]. The Brinkman equation considers the balance of forces acting on a volume element of fluid, i.e., the pressure gradient, the divergence of the viscous stress tensor, and the friction force exerted by the porous medium:

$$\eta \nabla^2 v - \nabla p - \frac{\eta}{\kappa} v = 0. \tag{4.5}$$

The crucial assumption is that the external force in the Navier-Stokes equation [Eq. (4.3)] can be replaced by the force term in Darcy's law [Eq. (4.4)]. This substitution is only justified if the porous medium occupies a vanishingly small fraction of space. In that case one may consider the porous medium as a continuum that exerts a

friction on the fluid at every point. In spite of the approximate nature of the Brinkman equation, it has proved to be an extremely useful tool for modeling flow in spatially inhomogeneous porous media [35, 36].

Of most relevance to us here is the use of the Brinkman equation to describe not average flow velocities, but the spatial decay of fluctuations in the flow velocity. It is clear from Eq. (4.2) that it is these fluctuations that play the crucial role in determining the dispersion coefficient. Indeed, if Brownian motion can be neglected, the particle velocity $v_i(t)$ appearing in Eq. (4.2) is simply the instantaneous velocity of a particle as it convects along a streamline. This we refer to as the Lagrangian velocity correlation function $C_v(t)$. This concept was utilized by Koch and Brady [37] in their theoretical analysis of dispersion in random media composed of randomly distributed fixed particles. Notably, they made use of the fact that a velocity fluctuation generated by one of the fixed points making up the porous medium will, according to the Brinkman theory, decay in space on a length scale set by the Brinkman length λ . The Brinkman length is the square root of the permeability. If the particles making up the medium have no spatial extension (they are simply points in the fluid exerting friction), the decay is exponential. If they do have a spatial extension, in the sense that stick boundary conditions apply on the surface, the decay is slower, going with distance r as $1/r^3$ [38]. On the other hand, if the presence of the porous medium is neglected, the Brinkman equation reduces to the usual Navier-Stokes equation for which a velocity perturbation decays as $1/r$. This leads to an unbounded integral for the dispersion coefficient, implying that the dispersion coefficient diverges; that is, it would always depend on the system size. The hydrodynamic screening predicted by the Brinkman equation thus plays a crucial role in determining the dispersion coefficient. A similar effect occurs in sedimentation, where velocity fluctuations in an unbounded system diverge [39]. In this case, it is the presence of container walls that is crucial in providing the necessary screening [40].

The question we want to address here is how well this picture, central to the theory of Koch and Brady [37], describes hydrodynamic dispersion. One reason for doing so is that numerical simulations of dispersion in packed beds of spheres, reported in Ref. [41], suggested that the dispersion coefficient was still increasing on time scales where the theory suggested it should have already converged. This raised the question: Is this the asymptotic behavior? For realistic packed beds of spheres Koch *et al.* [42] showed that the screening picture describes the decay of the velocity fluctuations reasonably well. Dorlosfky and Brady [43] arrived at the same conclusion. There are nonetheless two complications with this "realistic" system. First, as noted above, the Brinkman screening is less dramatic (going from a $1/r$ decay to $1/r^3$) for spatially extended particles than is the case for points (from $1/r$, to exponential). Second, the presence of an explicit solid/fluid interface, where the flow velocity goes to zero, means that there is a region close to the surface that the tracer particles must always enter and leave by diffusion. Koch and Brady suggest that the presence of this diffusive boundary layer means that the dispersion coefficient reaches its asymptotic value on time scales much longer than would otherwise be expected. This could also be responsible for the behavior observed in Ref. [41]. In this chapter we, therefore, consider a simple model system where both these complications are absent; that is, following in the spirit of the theory, we consider a porous medium composed of fixed points that exert

friction but have no spatial extension. Indeed, the analysis of such a system gives one contribution to the overall dispersion coefficient in the expression derived for a packed bed [37]. It is regarded as the contribution to the dispersion coefficient due to the velocity perturbation at distances far from the fixed particle. Specifically, this purely convective term, D_c, makes a contribution to the total dispersion coefficient

$$D_c = \frac{\overline{V}}{8\pi\rho\lambda^2}, \tag{4.6}$$

where ρ is the number density of the fixed points. For the work we describe here, we will ignore Brownian motion and concentrate solely on the decay of velocity fluctuations due to convection. In that case, we have $D = D_c$. While the model may seem of somewhat academic interest, there are important examples of hydrodynamic dispersion in dilute systems for which the model could be reasonably applied. Dispersion in flow through polymer networks would be an example.

4.2 Description of the model

To simulate fluid flow in our model porous media, we employed the D3Q18 lattice-Boltzmann (LB) method, introduced in Chapter 2. Here we recapitulate only the basics. The quantity we calculate in the LB method is the discretized one-particle velocity distribution function $f_i(\mathbf{r}, t)$, which is the probability that a particle at lattice site $\mathbf{r}$ at time t has a velocity $\mathbf{c}_i$. For the calculation that we performed, we needed the density $\rho(\mathbf{r})$ and momentum density $\mathbf{j}(\mathbf{r})$, which are moments of this distribution function

$$\rho(\mathbf{r}, t) = \sum_i f_i(\mathbf{r}, t), \tag{4.7}$$

$$\mathbf{j}(\mathbf{r}, t) = \sum_i \mathbf{c}_i f_i(\mathbf{r}, t), \tag{4.8}$$

where i sums over all possible velocities $\mathbf{c}_i$. The time evolution of the distribution function is described by the discretized analog of the Boltzmann equation [8]:

$$f_i(\mathbf{r} + \mathbf{c}_i, t + 1) = f_i(\mathbf{r}, t) + \Delta_i(\mathbf{r}, t), \tag{4.9}$$

where, Δ_i is the change in f_i due to "collisions" at the lattice sites. The post collision distribution $f_i + \Delta_i$ is propagated in the direction of the velocity vector $\mathbf{c}_i$. The overall procedure involves two steps: a propagation step and a collision step. In the propagation step each distribution function moves to the neighboring site with velocity $\mathbf{c}_i$. In the collision step the distributions at each site "collide," in the sense that they are modified by the collision operator. In Chapter 2 we have already shown that following this procedure, the evolution of the hydrodynamic fields satisfy the Navier-Stokes equations.

We now need a method to model the porous medium. Within the lattice-Boltzmann framework there is a straightforward procedure for imposing stick boundary conditions at an explicit solid/fluid interface. A simple bounce-back rule performed on boundary

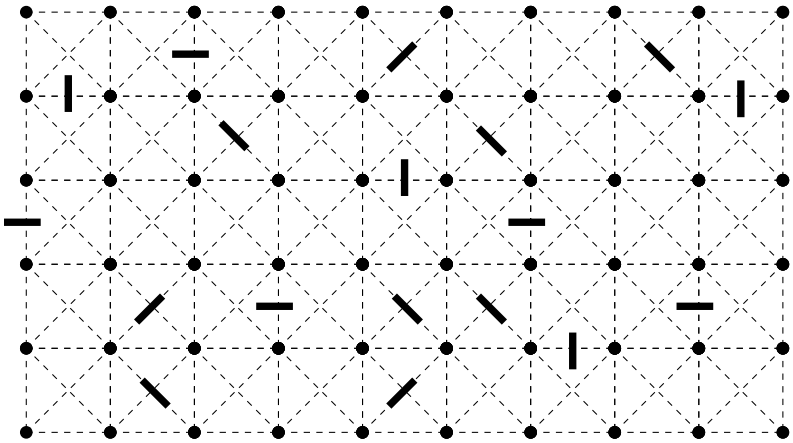

Figure 4.1: Two dimensional schematic representation of the model porous medium we employed. The dashed lines represent the allowed links between lattice sites. The thick bars on a link show broken links where the bounce back procedure will be implemented.

links enforces the stick boundary condition to second order, while not perturbing the stress [8]. Boundary links are defined as links connecting lattice sites inside and outside the solid object, and obviously these come in pairs. Adopting a convention of labeling the link that goes from inside to outside as ib and its partner $-ib$ the bounce back equations reads as

$$\begin{aligned} f_{-ib}(\mathbf{r}_b, t+\Delta) &= f_{ib}(\mathbf{r}, t) \\ f_{ib}(\mathbf{r}_b + \mathbf{c}_{ib}, t+\Delta) &= f_{-ib}(\mathbf{r}_b + \mathbf{c}_{ib}, t). \end{aligned} \tag{4.10}$$

Here we do not want an explicit solid-fluid interface, in the sense of a solid phase that excludes volume from the fluid. Instead, with a given probability, we break links [that is, define a set of links for which the propagation equation is modified according to Eq. (4.10)]. These broken links exclude no volume (so long as the fraction of broken links stays well below the percolation threshold) but will exert a friction on the fluid proportional to the local flow velocity. They are effectively point scatterers.

4.3 Results

To generate our model porous medium we generated a set of point sources for friction according to a binomial distribution. We first fixed the probability Φ that a link would be broken. This number was varied between 0.01 and 0.3. For every link, we then generated a random number between 0 and 1. If this random number was less than Φ, the link was broken, otherwise it was left intact. In this way, we generated one particular realization of the porous medium for a given value of Φ. All our results were obtained by performing simulations for at least 25 independent configurations for every value of Φ. Note that, for every configuration, the fraction of broken links

is not exactly equal to Φ. Only the average value is imposed. We cannot predict *a priori* how the Brinkman length depends on the fraction Φ of broken links, because this, even for point scatters, involves the many-particle hydrodynamic interactions. We therefore determine λ numerically. This can be done in two ways. One is to measure the average flow velocity in the presence of an applied external force and calculate the permeability. The second is to compute the flow profile in a simple confined geometry. For instance, the Brinkman Eq. (4.5) can easily be solved for a three-dimensional porous medium confined in a slit bounded by two hard walls. On the walls, stick boundary conditions apply. If we apply a body force parallel to the plates, the solution for the steady velocity profile, as function of the distance from the center z, is given by

$$v_x(z) = \frac{\lambda^2 F}{\eta}\left[1 - \frac{\cosh\left(\frac{z}{\lambda}\right)}{\cosh\left(\frac{L}{2\lambda}\right)}\right], \tag{4.11}$$

where the two plates are located at $z = -L/2$ and $z = +L/2$, x is the direction of the force, and F is a force per unit of volume. Note that the Brinkman length λ enters this equation twice: first through the (Darcy) prefactor, and second through the "screening" length that determines the shape of the flow profile. The constraint that a single value of λ should fit both the shape and the prefactor provides a good consistency check on our determination of λ.

The simulation box had a length of 320 lattice spacings in the direction of the flow, and 40 lattice spacings in the other two directions. Periodic boundary conditions were used in the unbounded directions. Even for the lowest density system ($\Phi = 0.01$), the Brinkman length was found to be no larger than 3.41 lattice units. This is more than an order of magnitude less than the smallest system dimension. At larger values of Φ, the Brinkman length is even smaller. Hence, we expect finite-size effects to be negligible at all the values of Φ that we studied. To study the flow, we let the system evolve under the applied body force $\mathbf{F}$. After some transient time, the flow fields reach a steady state. All correlation functions that we report have been computed for this steady state. To compute the average flow profile, we averaged the steady-state flow profiles of all 25 different configurations. It is to this averaged flow profile that we fitted the Brinkman flow profile given by Eq. (4.11). A result of this fitting procedure is shown in Figure 4.2. It is worth remembering that the Brinkman length is the only parameter in this fit. The figure shows that the computed flow profile fits the Brinkman expression. This result is not *a priori* obvious and provides a useful check that we do indeed have a system with a well-defined Brinkman length whose spatially averaged behavior is a solution to the Brinkman equation. By repeating this fitting procedure for other values of Φ, we obtained the dependence of λ on Φ. We found that the low density result $\lambda \propto 1/\sqrt{\Phi}$ holds to a good approximation over the whole range of Φ we consider here.

As Figure 4.2 shows, the Brinkman length describes the distance over which a flow profile in a porous medium is perturbed by an "obstacle" (in this case the hard wall). In the spirit (if not the letter) of Onsager's regression hypothesis, we might expect that "spontaneous" spatial velocity fluctuations should decay on the same length scale. To verify this, we computed the spatial velocity correlation function (SVCF) defined as

$$C_s(r) = \langle \left[v(0) - \overline{V}\right]\left[v(r) - \overline{V}\right]\rangle \tag{4.12}$$

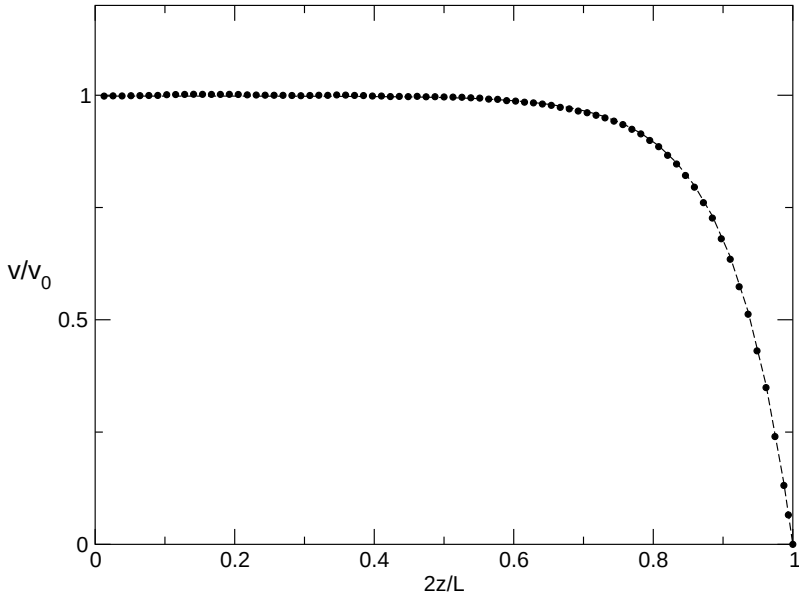

Figure 4.2: Velocity profile for a fluid flowing through the model porous medium confined between two plates. Flow velocity v normalized by the maximum flow velocity v_0 is plotted as a function of dimensionless distance from the center. The dashed line is the solution of the Brinkman equation; the circles are the numerical data.

where $v(r)$ is the component of fluid velocity along the flow direction at a distance r. To compute the SVCF (and all remaining correlation functions), we considered a purely periodic system without walls. In such a system, the average flow velocity is the same everywhere. In any specific realization of the disorder, however, there will be local deviations from the average value. The SVCF shows how these disorder-induced fluctuations decay, spatially, to zero.

In Figure 4.3 (open symbols) we show $C_s(r)/C_s(0)$ computed for a range of values of Φ. In this figure, we have expressed all distances in units of the Brinkman length λ. If, as we assume, the Brinkman length is the only relevant length scale in the system, then all the functions should superimpose. This is precisely what we observe. Moreover, the SVCF decays exponentially, with a characteristic decay distance of a Brinkman length. It seems, therefore, that the average flow profiles and the averaged spatial decay of perturbations in the flow profile satisfy Brinkman scaling. It would seem logical to assume that, as the spatial decay of velocity fluctuations satisfies Brinkman scaling, so should the temporal decay. If this were true, then Brinkman scaling should apply to dispersion of tracer particles. In fact, it has been argued that the nature of the equations, in particular, that the Brinkman equation has no explicit time dependence, has as a consequence that the Lagrangian velocity correlation function (LVCF) should decay in the same way as the SVCF, i.e., exponentially, with a characteristic time

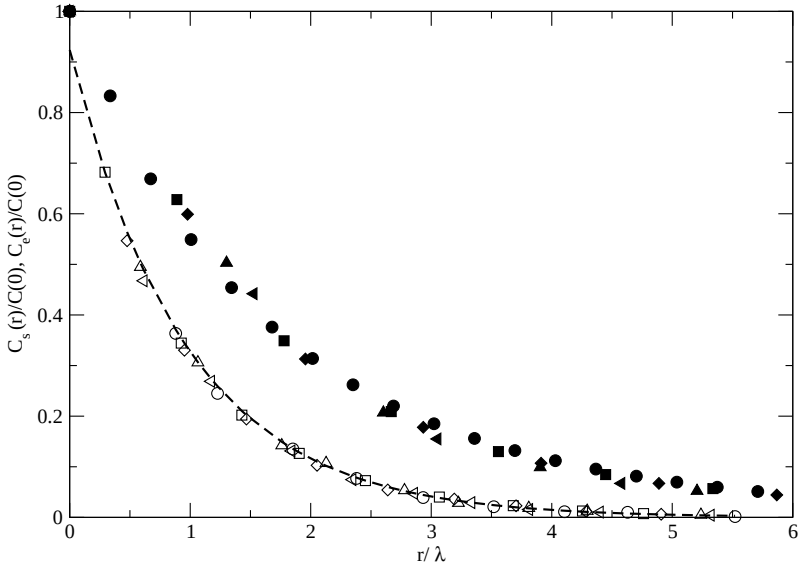

Figure 4.3: The normalized spatial velocity correlation function $C_s(r)/C(0)$ (open symbols), and Eulerian velocity correlation function $C_e(r)/C(0))$ (filled symbols), as a function of dimensionless distance r/λ. The broken link fractions are $\Phi = 0.01$ (plus), 0.08 (circles), 0.1 (squares), 0.2 (diamonds), and 0.3 (triangles). Error bars are smaller than symbols. The dashed line is the result of fitting an exponential to $C_s(r)/C(0)$ for $r/\lambda > 0.5$

equal to $\lambda/\overline{V}$ [37]. The LVCF is, within this approximation, simply

$$C_v(t) \approx \langle \left[v(0) - \overline{V}\right] \left[v(\mathbf{r} = \overline{V}t) - \overline{V}\right] \rangle = C_e(r = \overline{V}t) \tag{4.13}$$

We call this approximation to the LVCF the Eulerian time velocity correlation function (EVCF), $C_e(\overline{V}t)$. In Figure 4.3 (filled symbols) we show the normalized EVCF computed for a range of values of Φ, together with the SVCF. We observe that, to a good degree of approximation, all EVCF's superimpose. The typical length of decay is a little bit larger than that for the SVCF, because we are now considering correlations along the flow direction only. Otherwise, there is little difference. Based on this approximation, one would expect that the natural unit of time for the Lagrangian velocity correlation functions is the Brinkman time defined as $\tau = \lambda/\overline{V}$, i.e., the average time it takes a tracer particle to travel over a distance equal to one Brinkman length. In order to calculate the Lagrangian velocity correlation function, we need to follow the trajectory along which a particle travels; that is, we have to calculate velocity correlations for a streamline. In Appendix 4.B we describe our procedure for doing so. Figure 4.4 shows the LVCF for a system with $\Phi = 0.3$. In the same figure, we show the theoretical prediction for the shape of the LVCF corresponding to the EVCF and assuming that the velocity time correlation function can be obtained directly by replacing the displacement in the latter by $t\overline{V}$. The figure shows clearly that there exists no such simple relation between the spatial and temporal decays of velocity

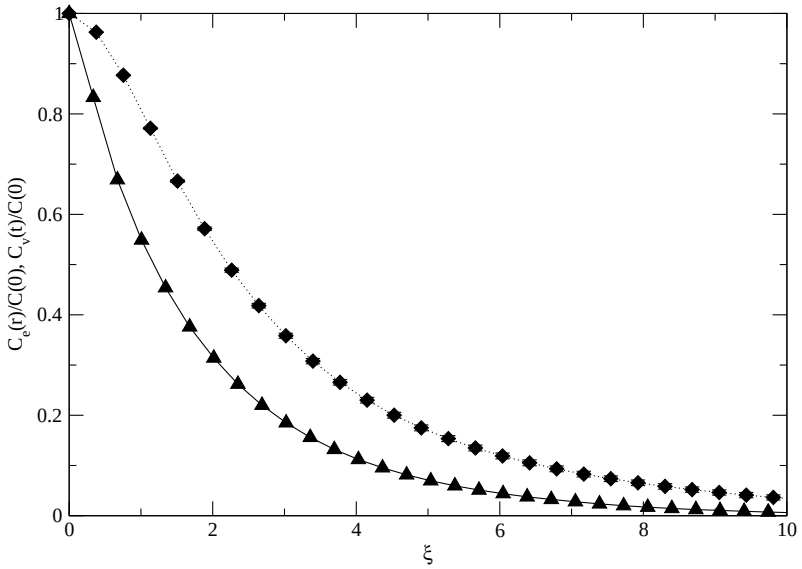

Figure 4.4: Comparison of the scaled, normalized, Eulerian (triangles), and Lagrangian (diamonds) velocity correlation functions. ξ is in dimensionless unit equal to r/λ for $C_e(r)$ and to t/τ for $C_v(t)$. Time τ is the average time to convect a Brinkman length ($\tau = \lambda/\overline{V}$). The dotted lines are guides to the eye.

fluctuations. In the first place, there is a marked difference in the behavior at short times. The initial rate of decay of the Lagrangian function is zero, so it cannot be approximated by an exponential. It is straightforward to show, from the incompressibility condition, that this must be the case (see Appendix 4.A). More importantly, if we plot the LVCF for different values of Φ (i.e., different Brinkman lengths), we cannot make the different LVCF's collapse onto the same master curve (see Figure 4.5). This is surprising, because it suggests that the Brinkman time is *not* the only relevant time scale in the system. In fact, Koch and coworkers [37, 42] have suggested that anomalous ("non-Brinkman") decay of velocity time correlation functions should be intimately linked to similar anomalies in the SVCF. Yet, our simulations appear to show "normal" behavior in the EVCF and "anomalous" behavior in the LVCF. As the LVCF decays much more slowly than one would expect on basis of the Brinkman-scaling assumption, the dispersion coefficient [calculated from Eq. (4.2)] is larger than would be predicted by simple use of the Brinkman equation. The slow decay of the LVCF indicates that the velocity of tracer particles remains strongly correlated in the time that it takes the fluid on average to move over one Brinkman length. Hence, the hydrodynamic screening picture that works so well for average flow profiles, seems to be quantitatively (though not qualitatively) incorrect when we consider temporal correlations.

In what follows, we shall consider hydrodynamic dispersion in the limit of high Peclet number. In this limit, and in the absence of any explicit solid/fluid interface, the

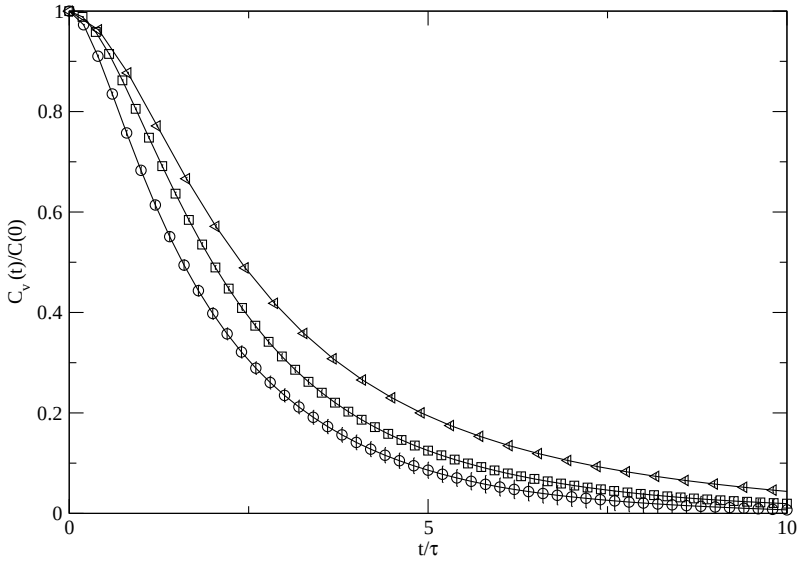

Figure 4.5: The normalized Lagrangian velocity correlation function as a function of dimensionless time. The different points correspond to different broken link fractions. The corresponding dimensionless densities are 2.4 (circles), 1.7 (squares), and 0.27 (triangles). Note that the curves do not superimpose but decay more slowly with decreasing dimensionless density (increasing absolute density). The lines are guide to the eye.

Brownian motion of the tracer particles can be ignored. It then follows from Eq. (4.2), that the dispersion coefficient is related to the time integral of the Lagrangian velocity correlation function. We now compare the computed dispersion coefficients with values predicted by the theory of Koch and Brady. Before proceeding, we need to briefly recapitulate their model. They model the porous medium by a continuum of points, every point exerting a friction on the fluid. This might seem an abstract concept of porous media, but it represents a simplified model of a dilute packed bed of spheres in the limit of many scatterers per Brinkman length cubed. Using such a model, they were able to compute the fluid velocity perturbation at large distances generated by particles making up the porous medium. From this they derive an expression for the dispersion coefficient. In order to perform the calculation they approximate the LVCF with the EVCF. The resulting theoretical expression for the dispersion coefficient at high Peclet number D_{th} is

$$\frac{D_{th}}{D_0} = \frac{3}{4} Pe, \tag{4.14}$$

where the Peclet number is $Pe = U^* l^* / D_0$; U^* being naturally identified with the mean velocity of fluid $\overline{V}$ and D_0 being the diffusion coefficient [here superfluous because it cancels the D_0 on the left hand side of Eq. (4.14)]. Some discussion is needed about the choice of l^*. In general, l^* is a typical length of the system. The theory takes as a characteristic length the "effective" radius of spherical particles that leads to a low

density random medium with the same Brinkman length; that is, particles that exert a friction equal to $6\pi\eta a$, where a is a "hydrodynamic radius". This gives the expression $D_{th} = \frac{3}{4}\overline{V}a$. In actual fact, the radius a is a somewhat fictitious parameter obtained by implying a dilute bed of spheres to model the porous medium. The following procedure is needed to obtain a as function of the Brinkman length λ. A dilute bed of spheres, with number density of scatterers ρ, exerts a total drag equal to ρ times the Stokes drag of a single sphere. Darcy's law gives a value for the same drag in terms of the Brinkman length [Eq. (4.4)]. Equating the two, one gets

$$\lambda = \sqrt{\frac{1}{6\pi\rho a}}. \tag{4.15}$$

Using Eq. (4.15), the dispersion coefficient becomes

$$D_{th} = \frac{< u >}{8\pi\rho\lambda^2} \tag{4.16}$$

We need, at this point, an expression for ρ in terms of the broken links model. We should point out that, at this level of detail, it is difficult to map our model directly to the theory because we have, in effect, points with a directionally dependent friction. The theory, on the other hand, considers points that exert an isotropic friction. To match (approximately) the two we proceed as follows. In the D3Q18 lattice there are 18 links, six of which have weight 2 [8]; in our case only two such links are oriented along the flow direction. There are also eight singly occupied links with a component in the flow direction, oriented at 45 degrees to the flow. We therefore take these to contribute 1/2. The remaining links are oriented perpendicular to the flow direction, so they contribute nothing. Allowing for the fact that each link belongs to two lattice sites, the effective density of links, in lattice units, we therefore take to be $\rho = 4\Phi$. From the simulation data the dispersion coefficient can be computed from the Lagrangian velocity correlation function

$$D = \int_0^\infty C_v(t)dt = C(0)\int_0^\infty C_v(t)/C(0)dt. \tag{4.17}$$

The initial value of the function, $C(0)$, is simply the covariance of the velocity field. This is, in fact, true for all the correlation functions we have defined. Equation (4.17) defines D. If, instead, we approximate LVCF with EVCF, we can define

$$D_{Eul} \quad = \quad C(0)\int_0^\infty C_e(t)/C(0)dt = C(0)\tau'. \tag{4.18}$$

As we have already shown that the normalized function $C_e(t)/C(0)$ scales onto a single curve; τ' defined by Eq. (4.18) and representing a characteristic time, is the same for all values of the Brinkman length. The two integrals will, in general, be different, in that while $C_v(t)$ is related to the velocity of the particle at time t, $C_e(t)$ refers to the velocity of a particle at a position $r = \overline{V}t$. The two quantities are only necessarily equal in the absence of velocity fluctuations.

In units where length, time and velocity are, respectively, λ, τ, and $\overline{V}$, the dispersion coefficients are thus

$$\begin{aligned} D^*_{th} &= \frac{1}{8\pi\rho\lambda^3}, \\ D^*_{Eul} &= \frac{C(0)}{\overline{V}^2}\frac{\tau'}{\tau}, \\ D^* &= \frac{1}{\overline{V}^2}\int_0^\infty C_v(t)dt. \end{aligned} \tag{4.19}$$

In the following we will plot the dispersion coefficients as a function of the dimensionless friction point density $\rho^* = \rho\lambda^3$. This is the number of scatterers per cubic Brinkman length and sets the intrinsic scale of the system. The scaling of the Brinkman length [$\lambda \sim \rho^{-1/2}$, see Eq. (4.15)] means that dense porous media in "real word" units are actually dilute in the intrinsic scale set by the Brinkman length. In fact, when $\rho \to \infty$, $\rho^* \to 0$; that is, high dimensionless number densities correspond to the approximations made in the theory, because in the (spatially) dilute limit there are many scatterers per Brinkman length cubed. This assumption is needed to treat the porous medium as a continuum. We are thus able to disentangle the effect of the dilute limit approximation and use the EVCF instead of the LVCF to compute the dispersion coefficient. In Figure 4.6 we plot D^*_{th} and D^*_{Eul} as functions of $1/\rho^*$ for high values of ρ^*. The theoretical value of the dispersion coefficient D^*_{th} is a linear function of $1/\rho^*$ [Eqs. (4.19)]. We observe that in the dilute limit D^*_{Eul} also has a linear behavior. A linear fit of D^*_{Eul} for high ρ^* has an intercept at zero, as the theory predicts. In the figure we plotted also D^*, which has the same behavior. At a given number density the difference between D^*_{th} and D^*_{Eul} quantifies the effect of the dilute limit approximation, whereas the difference between D^*_{Eul} and D^* quantifies the error made by approximating the LVCF with the EVCF. The difference between D^*_{th} and D^* is a measure of the accumulated effect of the two approximations. We can conclude that the theoretical expression works very well in the dilute limit. In this regime the absolute agreement between the theory and simulations, given the approximate nature of the mapping, is clearly very good. This confirms the prediction of Koch and Brady theory that the dispersivity is independent of volume fraction for dilute beds.

In Figure 4.7 we show the whole range of densities covered by our simulations, and we repeat the analysis carried out for Figure 4.6. Again on the abscissa is the inverse dimensionless density $1/\rho^*$. For decreasing values of the dimensionless density the two lines diverge. The difference between the two represents the factor needed to correct for the dilute limit assumption. We observe that the computed dispersion coefficients no longer have a linear dependence on $1/\rho^*$. We also see that there is an appreciable difference between the exact dispersion coefficient D^* and both the approximations D^*_{Eul} and D^*_{th}. This difference increases with decreasing ρ^*. This means that, for what would correspond to an *increasingly* packed bed, the dispersion coefficient becomes much larger than the theory predicts. Both the dilute limit assumption and approximating the Lagrangian velocity correlation function with the Eulerian contribute to the error. At low and moderate densities it is the former, rather than the latter, that limits the validity of the theory.

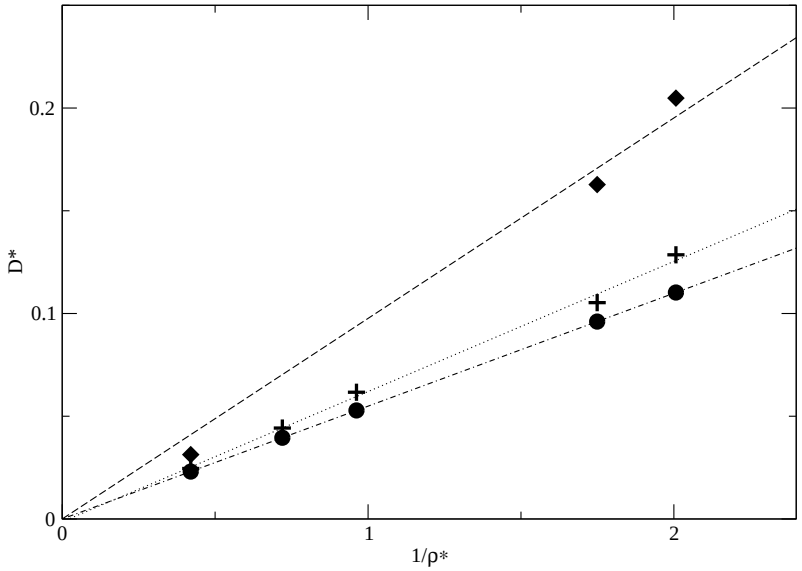

Figure 4.6: The dimensionless dispersion coefficient D^* (diamonds) as a function of inverse dimensionless density ρ^*. Also plotted are the theoretical values of the dimensionless dispersion coefficient D^*_{th} (circles) and the dispersion coefficient obtained by approximating the Lagrangian velocity correlation function with the scaled Eulerian function, D^*_{Eul} (plus). Note that high values of ρ^* correspond to low point densities so this data covers the spatially dilute regime. The lines are linear fits of the corresponding data points.

4.4 Conclusions

In this paper we described numerical simulations of flow through a simple model porous medium. The porous medium was modeled by simply breaking randomly, with probability Φ, the links used in the lattice-Boltzmann equation. From the point of view of comparing with theory, this broken link model has two advantages. First, it has no excluded volume. Second, it exerts a relatively high local friction. The latter allows one to calculate correlation functions over several Brinkman lengths. We showed, by two different calculations, that this model does indeed behave as the Brinkman equation predicts. Specifically, for the velocity profile of a flow through a porous medium sandwiched between two plates and the spatial decay of fluctuations in the local flow velocity about the mean (SVCF). The latter is an assumption in the Koch and Brady theory of dispersion in random media and it is a good one. We found that there is a universal behavior of spatial correlations if we measure lengths in units of the Brinkman length, confirming that this is the only relevant length in the system. We also confirmed that, spatially, this results in an exponential screening of the fluctuations. Again, this is central to the Koch and Brady theory. It guarantees convergence of the dispersion coefficient, which would otherwise diverge. We can conclude that the broken link model is well described by the Brinkman equation.

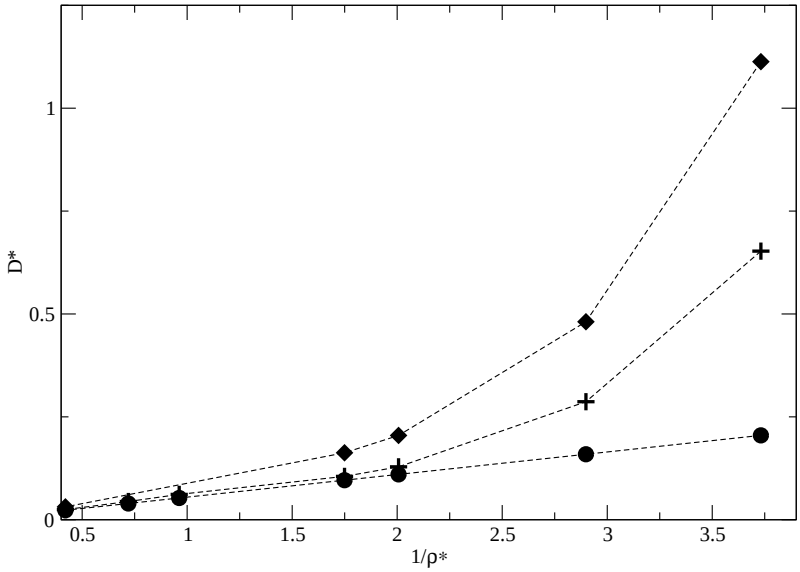

Figure 4.7: The dimensionless dispersion coefficient D^* (diamonds) as a function of inverse dimensionless density ρ^*. Also plotted are the theoretical values of the dimensionless dispersion coefficient D^*_{th} (circles) and the dispersion coefficient obtained by approximating the Lagrangian velocity correlation function with the scaled Eulerian function D^*_{Eul} (plus). Note that low values of ρ^* correspond to high point densities so this data extends to the spatially dense regime. The curves are drawn as a guide to the eye.

Conversely, the Brinkman equation describes successfully the spatial decay of velocity fluctuations in our model porous medium.

From the point of view of hydrodynamic dispersion, it is the temporal rather than spatial decay of fluctuations that is relevant. For the Lagrangian velocity correlation function (the temporal decay of the velocity a particle experiences as it traverses the fluid) things were more complex. This "time" velocity correlation function behaved quite differently. Its decay is not a simple exponential and, if we attempt to relate time to an average displacement, there is no universal behavior in the scaled decay. The decay of this function cannot be predicted by a simple mapping to the Brinkman equation alone. It is not possible to say that Lagrangian fluctuations are uniquely related to the Eulerian fluctuations for all densities of scatterers. This is an approximation invoked in the Koch and Brady theory and one, the simulations show, that is only strictly justified for low densities (Koch and Brady themselves acknowledge that it is a low density approximation). We should stress, however, that the decay of the Lagrangian correlation function with time is still asymptotically exponential. Thus, the qualitative picture that the screening of the velocity fluctuations by the porous medium itself leads to a convergent dispersion coefficient remains true. The results reported in Ref. [41] cannot be attributed to a breakdown of the screening picture, the slow decay must in some way be related to the more complex nature of

the porous medium, notably, the presence of excluded volume and diffusive boundary layers. Nonetheless, the conclusion that Lagrangian correlations can decay on much longer temporal (and, by implication, spatial) scales is consistent with Ref. [41]. Here, the correlation functions were decaying on timescales that greatly exceeded the Brinkman time.

Given the simplicity of our model and its similarity to the system Koch and Brady used to develop part of their theory of dispersion in packed beds, a direct comparison seemed appropriate. We thus computed the dispersion coefficient (in the limit where molecular diffusion can be neglected) as a function of broken link density. In the limit where the theory should be most valid (low volume fraction, a broken link "volume" interpreted as the volume of a sphere that exerts the same friction), we found reasonable agreement. At higher volume fractions, the agreement breaks down and the theory grossly underestimates the dispersion coefficient. In this regime, the decay of the Lagrangian velocity correlation functions differs dramatically from the scaled spatial decay used to approximate it in the theory. The fact that the theory gives dispersivities that actually agree quite well with experimental results for dense packed beds, must be due to the fact that it more accurately accounts for the boundary layer dispersion that we do not consider here.

4.A Initial rate of decay of the LVCF

In this section we give a simple argument as to why the initial gradient of the Lagrangian velocity correlation function, computed along the direction of the flow, should be zero. We define the $\mathbf{x}$ direction as the tangent to the trajectory $\hat{\mathbf{x}} \equiv \hat{\mathbf{t}}$. The $\hat{\mathbf{y}}$ and $\hat{\mathbf{z}}$ directions would be any pair of orthogonal vectors in the plane orthogonal to the trajectory. The LVCF is defined as $C_x(t) = \langle u_x(0)u_x(t)\rangle$ and its time derivative is

$$\frac{\partial C_x(t)}{\partial t} = \left\langle u_x(0)\frac{\partial u_x(t)}{\partial t}\bigg|_{t=0}\right\rangle. \tag{4.20}$$

On the other hand, the time derivative of the fluid velocity experienced by a tracer particle can be written as

$$\frac{\partial u_x(t)}{\partial t}\bigg|_{t=0} = \frac{\partial x(t)}{\partial t}\bigg|_{t=0}\frac{\partial u_x(t)}{\partial x}\bigg|_{t=0} = u_x(0)\frac{\partial u_x(t)}{\partial x}\bigg|_{t=0}. \tag{4.21}$$

We can now use the incompressibility condition $\nabla \cdot \mathbf{u} = 0$, this can also be written as

$$\frac{\partial u_x}{\partial x} + \left[\frac{\partial u_x}{\partial y} + \frac{\partial u_x}{\partial z}\right] = 0. \tag{4.22}$$

The term within the square brackets is zero by definition because of the choice of the axes. As a consequence $\partial u_x/\partial x = 0$, so it follows that $\partial C_x(t)/\partial t = 0$. Thus the initial slope of the LVCF along a stream line is zero. It follows that along the direction of the mean fluid flow the slope is also zero, because the average of the vector tangent to a trajectory is parallel to the vector defining the direction of the flow.

4.B Computing Streamlines

A streamline is the trajectory followed by a tracer particle when the system is stationary and the particles have no diffusion. In this section we describe how we computed the stream lines. The problem that has to be solved is simple: given a velocity field $\mathbf{V}(\mathbf{x}_i)$ on a lattice $\mathbf{x}_i$, construct a flux line $\mathbf{x}(t)$, where $\mathbf{x}$ is a continuous variable. A straightforward procedure to perform this calculation is the Euler method: $\mathbf{x}(t+1) = \mathbf{x}(t) + \mathrm{dt}\ \mathbf{V}(\mathbf{x}(t))$. This method is only accurate to first order. We employed the Runge-Kutta method in the midpoint approximation [44], which is accurate to second order in the time-step. Higher order methods were not necessary. The value of $\mathbf{V}(\mathbf{x}(t))$ has to be interpolated. In order to compute the off lattice values of the velocity field, we used a very simple trilinear interpolation, which is the three dimensional generalization of the linear interpolation $V(x_i + dx) = V(x_i) + \mathrm{dx}\ (V(x_{i+1}) - V(x_i))$.

Although very simple, the approach described above proved to be very robust. We checked that the time step chosen was small enough to ensure a consistent stream line calculation up to the distance used in our simulations. Any possible improvement in the stream line calculation results in a small enhancement of the effect we have pointed out in this chapter.

5 Discrete solution of the electrokinetic equations

Abstract

We present a robust scheme for solving the electrokinetic equations. This goal is achieved by combining the lattice-Boltzmann method (LB) with a discrete solution of the convection-diffusion equation for the different charged and neutral species that compose the fluid. The method is based on identifying the elementary fluxes between nodes, which ensures the absence of spurious fluxes in equilibrium. We show how the model is suitable to study electro-osmotic flows. As an illustration, we show that, by introducing appropriate dynamic rules in the presence of solid interfaces, we can compute the sedimentation velocity (and hence the sedimentation potential) of a charged sphere. Our approach does not assume linearization of the Poisson–Boltzmann equation and allows us for a wide variation of the Peclet number.

5.1 Introduction

The study of the dynamics of suspensions of charged particles is interesting both because of the subtle physics underlying many electrokinetic phenomena and because of the practical relevance of such phenomena for the behavior of many synthetic and biological complex fluids [45, 46]. In particular, electrokinetic effects can be used to control the transport of charged and uncharged molecules and colloids, using electrophoresis, electro-osmosis, and related phenomena [3]. As micro-fluidic devices become ever more prevalent, there are an increasing number of applications of electroviscous phenomena that can be exploited to selectively transport material in devices with mesoscopic dimensions [47].

In virtually all cases of practical interest, electroviscous phenomena occur in confined systems of a rather complex geometry. This makes it virtually hopeless to apply purely analytical modeling techniques. But also from a molecular-simulation point of view electroviscous effects present a formidable challenge. First of all, the systems under consideration always contain at least three components; namely a solvent plus two (oppositely charged) species. Then, there is the problem that the physical properties of the systems of interest are determined by a number of potentially different length scales (the ionic radius, the Bjerrum length, the Debye–Hückel screening length and the characteristic size of the channels in which transport takes place). As a result, fully atomistic modeling techniques become prohibitively expensive for all but the

simplest problems. Conversely, standard discretizations of the macroscopic transport equations are ill suited to deal with the statistical mechanics of charge distributions in ionic liquids, even apart from the fact that such techniques are often ill-equipped to deal with complex boundary conditions.

In this context, the application of mesoscopic ("coarse-grained") models to the study of electrokinetic phenomena in complex fluids seem to offer a powerful alternative approach. Such models can be formulated either by introducing effective forces with dissipative and random components, as in the case of dissipative particle dynamics (DPD) [48], or by starting from simplified kinetic equations, as is the case with the lattice-Boltzmann method (LB).

The problem with the DPD approach is that it necessarily introduces an additional length scale (the effective size of the charged particles). This size should be much smaller than the Debye screening length, because otherwise real charge-ordering effects are obscured by spurious structural correlations; hence, a proper separation of length scales may be difficult to achieve. A lattice-Boltzmann model for electroviscous effect was proposed by Warren [49]. In this model, the densities of the (charged) solutes are treated as passive scalar fields. Forces on fluid elements are mediated by these scalar fields. A different approach was followed in Ref. [50], where solvent and solutes are treated on the same footing (namely as separate species). This method was then extended to couple the dynamics of charged colloids to that of the electrolyte solution. As we shall discuss below, both approaches have practical drawbacks that relate to the mixing of discrete and continuum descriptions.

The LB model that we introduce below appears at first sight rather similar to the model proposed by Warren. However, the underlying philosophy is rather different. We propose to consider the *fluxes* between connected nodes as the basic physical quantities that determine the evolution of local densities. Such a formulation ensures local mass conservation, does not rely on fluxes or gradients computed at the lattice nodes (which constitutes a source of error in other models due to the need to approximate them on a lattice), and by choosing a symmetric formulation for the link fluxes in terms of the nodes that are affected, we can recover the proper equilibrium without spurious fluxes. Our model relies on a LB formulation for mixtures. Hence, the improvements of the formulation based on link fluxes will overcome some of the limitation of previous LB models for mixtures based on gradient expansions of a free energy [51, 52].

The method described is very flexible, and, in particular, general boundary conditions are easily implemented. This feature also makes the proposed formulation attractive, since it avoids problems related to mass and charge conservation at fluid–solid interfaces, an artifact that has plagued previous LB implementations. It is then possible to model the dynamics of colloidal particles and polyelectrolytes in solution. The electrostatic interaction between them is derived from the charge distribution in the fluid. Hence, we do not need to assume any specific form for the interaction between charged colloids, or between monomers in a polyelectrolyte. Electro-osmosis, the sedimentation potential, electrophoresis, or other electrokinetic phenomena can be easily treated within the model. In this paper we consider the first two to illustrate the capabilities of the method.

The electrolyte is treated at the Poisson–Boltzmann level. We are not restricted

to the linearized Debye–Hückel regime and can study the electrokinetic effects at high charge densities, being only limited by ionic condensation (as occurs, for example, in cylinders). The model we introduce neglect effects due to charge correlations.

5.2 Numerical lattice method

In developing the method which I will present in this chapter, we were motivated by the necessity to solve the electrokinetic equations which I have already presented in Section 3.3.3. However, because these are a special case of the more general class of mixtures, I present the more general model. As I have shown in Section 3.3 the usual laws of conservation of mass and momentum reads, for a mixtures, as

$$\frac{\partial \rho_k}{\partial t} + \nabla \cdot \rho_k \mathbf{v} = \nabla \cdot D_k \left[\nabla \rho_k + \rho_k \nabla \beta \mu_k^{ex} \right], \tag{5.1}$$

and

$$\frac{\partial}{\partial t} \rho \mathbf{v} = \eta \nabla^2 \mathbf{v} - \nabla p^{id} - \sum_k \rho_k \nabla \mu^{ex} + \mathbf{F}^{ext}. \tag{5.2}$$

To solve these two equations, we propose a model that combines a description of momentum dynamics based on lattice Boltzmann, with a numerical description of the convection–diffusion equation. Quantities are defined on the nodes of a lattice, $\mathbf{r}$, and time evolves in discrete time steps. The lattice is prescribed by specifying its connectivity. The connections of each node are determined by specifying the set of allowed velocities, $\mathbf{c}_i$, where the subindex i runs over all the allowed velocities. Then, each node $\mathbf{r}$ is connected to the nodes $\mathbf{r} + \mathbf{c}_i$.

5.2.1 Diffusion model

For convenience, let us rewrite the convection-diffusion equation, Eq. (5.1), in the form

$$\frac{\partial}{\partial t} \rho_k + \nabla \cdot \rho_k \mathbf{v} = -\nabla \cdot \mathbf{j}_k, \tag{5.3}$$

where the diffusive flux is

$$\mathbf{j}_k = -D_k \left(\nabla \rho_k + \rho_k \nabla \beta \mu_k^{ex} \right). \tag{5.4}$$

For the sake of clarity, we discuss separately the change in density of the species k due to diffusion and to advection. The total change in time of the density is simply the sum of the two contributions.

Diffusion

Let us assume for the time being that the mixture diffuses in a fluid at rest. Equation (5.3) then becomes

$$\frac{\partial}{\partial t} \rho_k = -\nabla \cdot \mathbf{j}_k. \tag{5.5}$$

Integrating both sides of this equation over a volume V_0 and using the Green's formula $\int_{V_0} \nabla \cdot \mathbf{j} dV = \oint_{A_0} \mathbf{j} \cdot \widehat{\mathbf{n}} dA$, we obtain

$$\frac{\partial}{\partial t} \int_{V_0} \rho_k dV = - \oint_{A_0} \mathbf{j}_k \cdot \widehat{\mathbf{n}} dA, \tag{5.6}$$

where $\widehat{\mathbf{n}}$ is the outward unity vector normal to the surface, A_0, enclosing the volume V_0.

As we have pointed out previously, we will consider densities defined on nodes of a lattice and the time evolution evolves at constant time steps. In this case, we can identify the volume V_0 with the volume associated to that node, and A_0 is related to the connectivity of the lattice nodes. Then, Eq. (5.6) states that the change of the total number of particles enclosed in the volume corresponding to node $\mathbf{r}$ equals the sum of the outward fluxes. Such fluxes can only take place by mass transport to the neighboring nodes that are connected to the central node, according to the structure of the predetermined lattice connectivity. Hence,

$$n_k(\mathbf{r}, t+1) - n_k(\mathbf{r}, t) = -A_0 \sum_i j_{ki}(\mathbf{r}), \tag{5.7}$$

where $n_k(\mathbf{r})$ is the number of particles of species k at node $\mathbf{r}$, while $j_{ki}(\mathbf{r})$ accounts for the fraction of particles of species k going to node $\mathbf{r} + \mathbf{c}_i$. If we consider the velocity moving opposite to i, i.e., $\mathbf{c}_{i'} = -\mathbf{c}_i$, we have $j_{ki}(\mathbf{r}) = -j_{ki'}(\mathbf{r} + \mathbf{c}_i)$ because these fluxes are always defined considering that the particles move away from the reference node. This unambiguously show that the fluxes are related to the links joining the connected nodes, rather than being quantities defined on the nodes.

It is worth noting that in the previous balance equation the relevant quantity is the number of particles of species k at node $\mathbf{r}$, $n_k(\mathbf{r})$, rather than its number density, $\rho_k(\mathbf{r})$. If we take the volume of a cell as our unit of volume, then $\rho_k(\mathbf{r}) = n_k(\mathbf{r})$. However, in the presence of solid boundaries this distinction may become relevant. The prefactor A_0 in Eq. (5.7) is related to the geometrical structure of the lattice. Rather than connecting it directly with the area of the Wigner–Seitz cell that can be associated to node $\mathbf{r}$, we derive its magnitude by computing how density diffuses to the neighboring nodes. In Sec. 5.5.1 we will compute explicitly this geometric prefactor for a particular lattice. In the following, when referring to link mobility, we will use the symbol $d_k = D_k A_0$.

Using link fluxes to compute the variation of the densities of the different species avoids approximating the divergence on a lattice, a source of lattice artifacts, and the related potential spurious fluxes that may appear. Moreover, the use of these link fluxes also imposes locally mass conservation to machine accuracy, avoiding the errors caused by the discretization of the spatial gradient operator. We must still provide a prescription to implement the diffusive fluxes. These are, in principle, given by Eq. (5.4) and involve spatial gradients between two neighboring lattice nodes. In equilibrium, $n_k^{eq} \sim \exp[-\beta \mu^{ex}]$ and, as a consequence, Eq. (5.4) predicts that all diffusive fluxes vanish. However, the direct implementation of Eq. (5.4) on a lattice will suffer from discretization errors that will result in small but noticeable spurious fluxes. To eliminate this effect, it is convenient to write the expression for the flux on

a link as

$$\mathbf{j}_k(\mathbf{r},t) = -D_k e^{-\beta\mu_k^{ex}(\mathbf{r},t)}\nabla\left[\rho_k(\mathbf{r},t)e^{\beta\mu_k^{ex}(\mathbf{r},t)}\right], \tag{5.8}$$

because, in this expression, the gradient becomes identically zero when the density distribution corresponds to its equilibrium form. This also holds for the discretized form to be discussed below. Consistent with the idea that the flux can be expressed in terms of link mass fluxes, we propose a symmetrized implementation of j_{ki} involving magnitudes defined in the two connected nodes, $\mathbf{r}$ and $\mathbf{r}+\mathbf{c}_i$. In particular, we write the flux of species k along the link $\mathbf{c}_i$ as

$$j_{ki}(\mathbf{r}) = -d_k\frac{e^{-\beta\mu_k^{ex}(\mathbf{r})}+e^{-\beta\mu_k^{ex}(\mathbf{r}+\mathbf{c}_i)}}{2}\left[\frac{n_k(\mathbf{r}+\mathbf{c}_i)e^{\beta\mu_k^{ex}(\mathbf{r}+\mathbf{c}_i)}-n_k(\mathbf{r})e^{\beta\mu_k^{ex}(\mathbf{r})}}{\Delta_i}\right], \tag{5.9}$$

where $\Delta_i = |\mathbf{c}_i| = |\mathbf{c}_{i'}|$ is the distance between the two neighboring nodes. This symmetrized formulation ensures that, to machine accuracy, $j_{ki}(\mathbf{r}) = -j_{ki'}(\mathbf{r}+\mathbf{c}_i)$, and mass is conserved for the model elementary dynamic processes. Note that, based on the mass conservation expression, Eq. (5.7), the global mass change of node $\mathbf{r}$ is the sum of the link fluxes, j_{ki}. Mass evolution in the diffusive limit is described only on the basis of mass flux divergence, as we have described. In general, the procedure developed based on link fluxes provides a consistent framework to obtain other gradients if needed.

Advection.

Local density can also be altered due to advection if there is a local velocity of the fluid. If, for the time being, we disregard diffusion, the advection mechanisms can be written in the form

$$\frac{\partial}{\partial t}\rho_k = -\nabla\cdot(\rho_k\mathbf{v}), \tag{5.10}$$

where $\mathbf{v}$ is the barycentric fluid velocity. In principle, the change in the number of particles could be computed on the basis of the advection along each link, in a way similar to Eq. (5.7). However, as we will describe in the next section, the model we will introduce provides the velocity at each node, rather than the link velocity. In order to avoid numerical artifacts and spurious diffusion due to the interpolation to get such a link velocity, we propose an alternative implementation of the advection process. We still consider that $n_k(\mathbf{r})$ give us the number of particles in a volume element centered around node $\mathbf{r}$. Since we know the velocity of that node, $\mathbf{v}(\mathbf{r})$, in one step the node will *virtually* displace to $\mathbf{r}+\mathbf{v}(\mathbf{r})$. As a result, the volume associated to node $\mathbf{r}$ will intersect some neighboring cells of the real lattice (see Fig. 5.1). We then distribute the amount of particles n_k into the intersected volumes proportionally to the intersected region. In Fig. 5.1, we depict in shadow the volumes that correspond to the fraction of the density that is transported in the new cells. The advantage of this approach is that it greatly reduces the spurious diffusion that usually results during advection in lattice models. To be more precise, even with the present method, advection will cause some spurious diffusion (proportional to the flow velocity). However, in Sec. 5.5.1 we show that, in practice, this effect is negligible.

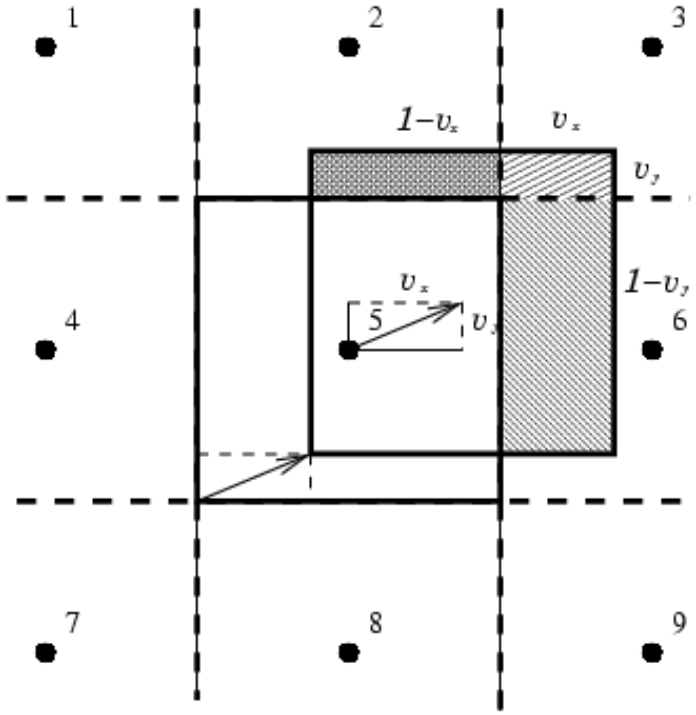

Figure 5.1: Density redistribution due to advection. To advect the charge of a given node (in this case, node number 5) in one time unit, we shift the whole cell with the local velocity vector of that node (v_x, v_y). Next, we displace a fraction of density equal to the area of the cell that is now in the corresponding site. In the graph a fraction of the density equal to the shadowed rectangle area $(v_x v_y)$ goes from cell 5 to cell 3, a fraction $(1 - v_x)v_y$ goes to cell 2, $(1 - v_y)v_x$ goes to cell 6, and $(1 - v_x)(1 - v_y)$ stays at node 5. For the sake of clarity, the figure shows a two-dimensional flow. In practice, the analogous procedure is carried out in 3D.

5.2.2 Lattice Boltzmann method.

In order to simulate the hydrodynamic flow of the fluid, we make use of the lattice-Boltzmann approach which I introduced in Section 2.4. To ease the reading of this manuscript, I will repeat once again the basics of the method.

The lattice-Boltzmann method describes the dynamics of a fluid in terms of the densities of particles that "live" on the nodes of a cubic lattice and have discrete velocities $\{\mathbf{c_i}\}$, where i labels the links between a lattice point $\mathbf{r}$ and its neighbors. The values of the velocities are chosen such that, in one time step, a particle moves along a link from one lattice node to its neighbor. In the Lattice-Boltzmann model, the unit of length is equal to the lattice spacing and the unit of time is equal to the time step. In addition, the unit of mass (or, equivalently, energy) is fixed by the requirement that, in the continuum limit, the transport equations for the lattice

model approach the Navier–Stokes equation. This imposes a relation between the temperature and the speed of sound [see below Eq. (5.14)]. The central dynamic quantity in the lattice-Boltzmann approach is the one-particle distribution function, $f_i(\mathbf{r}, t)$, which describes the probability of having a particle at site $\mathbf{r}$ at time t with velocity $\mathbf{c}_i$. The hydrodynamic variables are obtained as moments of this distribution function over the lattice velocities, $\mathbf{c}_i$; e.g., density and momentum can be obtained as

$$\rho(\mathbf{r}, t) = \sum_i f_i(\mathbf{r}, t), \tag{5.11}$$

$$\mathbf{j}(\mathbf{r}, t) \equiv \rho(\mathbf{r}, t)\mathbf{v}(\mathbf{r}, t) = \sum_i \mathbf{c}_i f_i(\mathbf{r}, t), \tag{5.12}$$

respectively.

In the presence of external forces $\mathbf{F}$, for a particular choice of the shear viscosity, $\eta = 1/6$ in lattice units [8], the general dynamic rule simplifies to [See Section 2.4.1]

$$f_i(\mathbf{r}, t+1) = a^i \left[\rho(\mathbf{r}, t) + \frac{1}{c_s^2} \mathbf{c}_i \cdot (\mathbf{j}(\mathbf{r}, t) + \mathbf{F}) \right]. \tag{5.13}$$

For the sake of convenience, we implement the model with this simplified updating rule. However, it is straightforward to implement the more general form that allows us to impose other values of the viscosity.

By means of a Chapman–Enskog expansion, it can be shown [53] that in the hydrodynamic limit one recovers the Navier–Stokes equation,

$$\frac{\partial}{\partial t} (\rho \mathbf{v}) = \eta \nabla^2 \rho \mathbf{v} - c_s^2 \nabla \rho + \mathbf{F}. \tag{5.14}$$

Since the second term on the rhs is the pressure gradient for an ideal gas, if we fix the temperature such that $k_B T = c_s^2$, we then recover Eq. (5.2) for an ideal mixture. For non ideal mixtures, we will introduce the missing contribution to the pressure gradients as a local external force, $\mathbf{F}$. Because the solutes act onto the solvent exclusively by means of this effective force $\mathbf{F}$, the hydrodynamic limit of the non-ideal-mixture model is obtained by following the same procedure as the one needed for the standard lattice-Boltzmann method for one phase flows [53].

Introducing the mixture non ideality as a local effective force implies that the fluid reacts with the appropriate susceptibility to applied external fields, although in the absence of spatial gradients the equilibrium distribution corresponds to that of an ideal gas. Since we are not concerned with local structure, the model can be regarded as an effective kinetic model, similar in structure to a linearized Vlasov equation. Hence, this approach differs from previous proposals that try to derive the hydrodynamics of non ideal mixtures from kinetic models of mixtures [54] or from a modification of the equilibrium distribution to recover the equilibrium pressure [51, 52].

The peculiarities of the non ideality of the mixture enters through the forcing term ($\mathbf{F}$) in Eq. (5.13). This forcing term can be decomposed into an external field and interaction contributions, $\mathbf{F} = \mathbf{F}^{ext} + \mathbf{F}^{sol}$. This interaction force, as previously described in Section (3.3), has the form $\mathbf{F}^{sol} = \sum_k \rho_k \nabla \mu_k^{ex}$. Using the same approach

that we have used to model the convection-diffusion equation, we can determine the force acting on each link, F_i. Moreover, for the particular case where the diffusion matrix is diagonal,

$$F_i(\mathbf{r}) = k_B T \sum_k \left[\frac{j_{ki}}{D_k} - \frac{n_k(\mathbf{r}+\mathbf{c}_i) - n_k(\mathbf{r})}{\Delta_i} \right]. \tag{5.15}$$

The advantage of using the force exerted on the links is that, again, we keep a symmetric dependence on the neighboring nodes, and, moreover, $F_i(\mathbf{r}) = -F_{i'}(\mathbf{r}+\mathbf{c}_i)$. Yet, in the lattice-Boltzmann update rule, we need the force acting on the node. This force can be obtained averaging the link forces,

$$F_\alpha^{sol}(\mathbf{r}) = \sum_i a^i c_{i\alpha} F_i(\mathbf{r}), \qquad \alpha = \text{x, y, z.} \tag{5.16}$$

Let us now introduce an alternative way of treating the same systems. There are situations, as is the case in electrolytes, where one of the components of the mixture is dominant, and plays the role of the solvent. In this case, we can single out this component, ρ_s, and treat it separately from the rest. In particular, since $\rho_s \gg \rho_k$, we can approximate the overall density by the solvent density ($\rho \simeq \rho_s$), and the overall momentum by the solvent momentum ($\rho v = \sum_k \rho_k v_k \simeq \rho_s v_s$). If we then relate the moments of the distribution function f_i to the solvent density, i.e., $\sum_i f_i = \rho_s$ and $\sum_i \mathbf{c}_i f_i = \rho_s \mathbf{v}_s$ instead of Eqs. (5.11), we impose a constant solvent density in the incompressible regime. Hence, the rest of the components will need to compensate their densities to avoid any net local density variation. Although this incompressibility constraint is not exact, it may be a convenient approximation. From the point of view of the link force, Eq. (5.15), it has the computational advantage that one gets $F_i = \sum_k j_{ki}/D_k$ and it reduces to the link diffusive flux previously computed, Eq. (5.9). In this case the Navier–Stokes equation becomes

$$\frac{\partial}{\partial t}\rho_s \mathbf{v}_s = \eta \nabla^2 \mathbf{v}_s - c_s^2 \nabla \rho_s - k_B T \sum_k [\nabla \rho_k + \rho_k \nabla \beta \mu_k^{ex}] + \mathbf{F}^{ext}, \tag{5.17}$$

and by taking $k_B T = c_s^2$, we recover an appropriate behavior when $\rho_s \gg \rho_k$.

The advantage of this approach is that densities of different species are dealt with on different footing, which may prove advantageous in certain applications, especially when dealing with boundary conditions that act differently on the solvent and solute, as it is the case if dealing with semipermeable membranes. Numerically, in this case there is a net force only when the density distribution deviates from its local equilibrium value, in contrast with the original method, where the density coming from the advection contribution balances the local force. This ensures an additional way to avoid spurious artifacts from the underlying lattice.

5.3 Boundary conditions

If the fluid mixture is confined between walls, or if colloids are added to the mixture, we need to specify how the densities and distribution function will interact with solid

interfaces. To account fully for such an interaction, we need to describe in turn how the distribution function behaves, how the particle number evolves, and how we estimate the interacting force at the surface.

At a solid surface we expect hydrodynamic "stick" boundary conditions to apply. One way to impose these is to apply the so-called "bounce-back rule" on the links. However, the standard version of this procedure (see, for example, Ladd [53]) allows the fluid to leak into the solid. Although this leakage is usually innocuous, there are cases (a typical example being when electrostatics is part of the excess chemical potential) where this leakage may change the density of the solvent inside the solid, leading to a corresponding error in the pressure gradient. There exist alternative bounce-back rules that do not allow for any fluid leakage [55].

The formulation of our model in terms of link fluxes simplifies the implementation of boundary conditions for the fluxes of the different species densities, ρ_k. Since the convection-diffusion equation involves only mass conservation, it is enough to impose that there is no net flux on any link that joins a fluid node and a solid node. We accomplish this by imposing that the diffusive flux $j_{ki} = 0$ on such a link, and that the flux due to advection also vanishes. This second requirement is achieved by a kind of partial bounce-back move: the number of particles that would have been assigned to a solid node after advection is reflected back to its node of origin.

The updating rule, both for the number densities of the convection-diffusion equations and for the lattice-Boltzmann distribution function, requires the evaluation of gradients of chemical potentials. To this end, we need to specify the values of the excess chemical potentials on neighboring nodes, and those may involve the values of the fluid densities in contact with the solid wall. We consider that the relevant value of the density is that in contact with the wall, which is somewhere in between the fluid and the solid node. Such value can be obtained by requiring that it is consistent with the no-flux condition for the link flux of that species. The no flux condition is satisfied requiring [see Eq. (5.9)]

$$n_k(\mathbf{r} + \mathbf{c}_i) = n_k(\mathbf{r}) e^{\beta[\mu_k^{ex}(\mathbf{r}+\mathbf{c}_i) - \mu_k^{ex}(\mathbf{r})]}, \tag{5.18}$$

which should be understood as the extrapolation of the fluid density to ensure the absence of flux diffusion, and, in general, it is an implicit equation to obtain an estimate of the extrapolated number of particles, $n_k(\mathbf{r} + \mathbf{c}_i)$. Note that this fictitious extrapolated density is a property of the link, not of the node.

As we have mentioned in Sec. 5.2, the formulation based on the fluxes is based on the evolution of the number of particles contained in a given volume element. For the fluid nodes in the absence of solid interfaces the particle number is proportional to the number density. This is no longer the case close to a solid wall. This difference is pertinent because the excess chemical potential and the pressure are functions of the number density, ρ_k. While for a wall at rest, one can still consider that the wall is equidistant from the nodes and n_k and ρ_k coincide, for a moving solid surface, the position of the solid boundary will change as it moves. In this case, a coefficient α that establishes how close the solid boundary is to the fluid node should be introduced. In the limiting case that the solid boundary is reaching the neighboring fluid node, the corresponding cell has a volume that is approximately half the volume of a usual cell, hence $\alpha = 1/2$; in the opposite case when the solid surface reaches the solid node one

gets accordingly $\alpha = 3/2$. This coefficient then allows us to relate $n_k = \alpha\rho_k$. Although there exist different ways in which this coefficient may be computed, any smooth function that accounts for the volume change will be enough to avoid abrupt changes in the density when a fluid nodes is absorbed or created by the moving boundary.

5.4 Electrokinetic equations.

In the previous sections we have developed a model to simulate general non ideal fluid mixtures. We will now analyze the special case in which the fluid mixture is an electrolyte. The simplest electrolyte model corresponds to a three-species mixture, two of them being the ionic species, ρ_+ and ρ_- with charges z_+e and z_-e, and the third one being the neutral solvent ρ_s. e is the elementary charge, and z_+ and z_- are the valences of the ions. The local charge can then be expressed as $q(\mathbf{r}) = e[z_+\rho_+(\mathbf{r}) + z_-\rho_-(\mathbf{r})]$.

The hydrodynamic evolution equations for this model electrolyte become, again,

$$\frac{\partial}{\partial t}\rho_k + \nabla\cdot\rho_k\mathbf{v} = D_k\nabla\cdot\left[\nabla\rho_k + z_k\rho_k\nabla\beta\Phi\right], \tag{5.19}$$

$$\frac{\partial}{\partial t}\rho\mathbf{v} = \eta\nabla^2\rho\mathbf{v} - c_s^2\nabla\rho + k_BT\sum_k z_k\rho_k\nabla\Phi, \tag{5.20}$$

and the Poisson equation,

$$\nabla^2\Phi = -4\pi l_B\left[\sum_{k=\pm} z_k\rho_k + \rho_s\right], \tag{5.21}$$

which has been expressed in terms of a dimensionless potential, $\Phi = e\beta\widehat{\Phi}$, while $l_B = \beta e^2/(4\pi\epsilon)$ is the Bjerrum length (the distance at which the electrostatic and the thermal energies are equal), with ϵ the dielectric constant of the fluid. In the previous equation, ρ_s stands for the charge density of the solid surfaces, if there are confining walls or moving suspended particles in the electrolyte. Obviously, ρ_s will be non zero only on those solid surfaces. The Equations (5.19), (5.20), and (5.21) are commonly referred to as the Electrokinetic equations.

The electrostatic potential Φ can be computed using standard techniques. Specifically, we have implemented a successive over-relaxation scheme (SOR) [44], where the Poisson equation is solved as the stationary solution of a diffusion equation (relaxation scheme). To speed up the convergence to the stationary state, one introduces an over-relaxation parameter ω and iterate

$$\begin{aligned}\Phi_{h+1}(\mathbf{r},t) &= \omega\left[\sum_i\left(a_1^i\Phi_h(\mathbf{r}-\mathbf{c}_i,t) + 4\pi l_B\frac{c_S^2}{2}\sum_{\alpha=+,-} z_\alpha\rho_\alpha(\mathbf{r},t)\right)\right] \\ &\quad +(1-\omega)\Phi_h(\mathbf{r},t).\end{aligned} \tag{5.22}$$

The iterative electrostatic potential Φ_h will converges to the Φ solution of the Poisson equation. The gradient of Φ is

$$\nabla\Phi(\mathbf{r}) = -\sum_i a_1^i\Phi(\mathbf{r}-\mathbf{c}_i)\mathbf{c}_i. \tag{5.23}$$

The advantage of this model is that it does not presume a specific type of boundary condition, and can be easily generalized to deal with media of different dielectric constants. Although not as fast as other methods for solving the Poisson equation, it is adequate for our purposes because, once the local equilibrium charge profiles are achieved, the calculation of the disturbed electrostatic potential due to external forces is much less time consuming than the iteration part related to lattice Boltzmann and convection–diffusion; alternative, more sophisticated, variants to solve the Poisson equation numerically can be implemented wherever the standard SOR routine proposed here becomes impractical.

5.5 Validation tests

In order to validate the model that we introduced in the previous section, we compare its predictions against known results. In particular, we verify that the equilibrium charge distribution is properly recovered on the lattice, and that out of equilibrium the different coupling mechanisms between fluid flow and charge inhomogeneities are properly accounted for.

5.5.1 Effective diffusion

As was pointed out below Eq. (5.7), the diffusion coefficient characterizing the discrete version of the diffusion equation is not the same as the link diffusion coefficient d_k but is related to it through a simple geometrical factor A_0 that depends on the type lattice used. A_0 can be evaluated as follows. Consider a situation where the transport of species k is purely diffusive. A density perturbation ρ_0, initially localized at node $\mathbf{r}_0$, will spread in one time step to the connected neighboring nodes. If the process is purely diffusive, we know the amplitude of the second moment of the density variation during this time step and $\sum_i \Delta_i^2 \rho(\mathbf{r}_0 + \mathbf{c}_i, t_0 + 1) = 6D_k\rho_0 = 6A_0 d_k \rho_0$ in a three-dimensional cubic lattice. Let us consider for concreteness the D3Q18 lattice [13], which is the lattice we used in our LB simulation. Since the link fluxes $j_i = d_k\rho_0/\Delta_i$, after one time step the density in each of the six nearest neighbors is $d_k\rho_0$, while the density in each of the other 12 connected nodes is $d_k\rho_0/\sqrt{2}$. As a result, $\sum_i \Delta_i^2 \rho(\mathbf{r}_0+\mathbf{c}_i, t_0+1) = d_k(6+12\sqrt{2})\rho_0$, which implies that $A_0 = 1+2\sqrt{2}$ [or $D_k = d_k(1+2\sqrt{2}]$. Depending on the value of d_k, it might happen that the total density transferred to the neighbors is larger than the initial density. For D3Q18 this gives us an upper bound for the input diffusion coefficient that ensures absolute stability, $d_k \leq 1/(6(1+2\sqrt{2})) = 0.044$. In practice, we find that for all cases that we have analyzed, numerical instabilities related to diffusion become relevant for values of the input diffusion coefficient $d_k \geq 0.05$. In order to perform simulations at higher diffusivities, we need to modify the numerical scheme to simulate the diffusion equation. This instability can be overcome by introducing a multiple-time step technique. To this end, we introduce a smaller diffusion coefficient $d_{it} = d_k/N_{it}$ and iterate N_{it} times the discrete diffusion equation, Eq. (5.7), to advance the densities one time step.

When applying this multiple time step method to solve the lattice diffusion equation, one must compute carefully the force that should be applied to the distribution

function f_i at the end of the time step. In fact, $\mathbf{F}^{sol}$ should be computed at all the intermediate steps. All these contributions should then be added to obtain the total force at the end of the iteration. With this technique, we can vary the diffusion coefficient over several orders of magnitude. For example, in our simulations we could vary D_k from $D_k = 10^{-3}$ to $D_k = 6$ (all in lattice units).

On top of the lattice effects on diffusion itself, advection can also induce spurious diffusion, because the lattice velocities do not coincide, in general, with the local velocity. As a consequence, a concentrated set of particles will spread over the lattice nodes, even if subject to a pure translational motion. Hence, only when the velocity is commensurate with the lattice spacing, both in direction and magnitude, will spurious diffusion be exactly zero. We must then quantify the amount of spurious diffusion. To this end, we consider an ideal binary mixture composed of a solvent with initial uniform density, ρ_s, and a solute with initial density ρ_t. The mixture is contained between two parallel walls that are permeable to the solvent but impermeable to the solute. The fluid is moving with a uniform velocity v perpendicular to the walls. As a result of the impermeability of the walls to the solute, a steady state is reached, determined by the solvent density profile, $\rho_t(x)$, which satisfies

$$\rho_t(x) = \rho_0 \exp\left[-\frac{v}{D^*}(x - x_0)\right], \tag{5.24}$$

where v is the fluid velocity, D^* the effective diffusion coefficient, and ρ_0 the solvent distribution at contact with the wall located at x_0. In Fig. 5.2 we show the effective diffusion coefficient measured by using Eq. (5.24) as a function of the fluid velocity for a range of values of the diffusion coefficient. We plot D^*/D_0 (where D_0 is the diffusion coefficient for a quiescent fluid). In order to show that there exists an intrinsic advection-induced spurious diffusion, we plot in the inset of the same figure the difference between the effective and the input diffusion coefficient for many values of the input diffusion coefficient as a function of the fluid velocity. Because all curves collapse, this graph shows that the diffusion coefficient induced by the advection depends only on the fluid velocity. We observe that the dependence on the (absolute value of) flow velocity is linear with slope 1/2. Following the procedure that we used above to compute the factor A_0, we can derive an expression for the advection-induced diffusion coefficient. In one dimension, a fraction $v\Delta t$ of the density $\rho(x)$ is displaced to the next node, while a fraction $(1 - v)\Delta t$ remains at the original node. The center of mass of the density is displaced by a factor $v\Delta t$. Simple algebra then shows that the second moment of the density variation during a time step is $< \Delta_i^2 >= v(1 - v)$. The flow-induced diffusion coefficient in one dimension is therefore $D^* = (1/2)v - (1/2)v^2$. In three dimensions this expression is readily generalized to yield

$$D^* = \frac{1}{2}\left[v_x(1 - v_x) + v_y(1 - v_y) + v_z(1 - v_z)\right]. \tag{5.25}$$

By choosing a sufficiently low value of the flow velocity, and a sufficiently large value of D_0, we can largely suppress the effect of this advective diffusion.

If, on the other hand, one is interested in large values of the Peclet number ($Pe = vl/D$, where v and l are, respectively, a typical velocity and length of the system and D the diffusion coefficient of the solutes), Eq. (5.25) sets an upper limit. The smallest

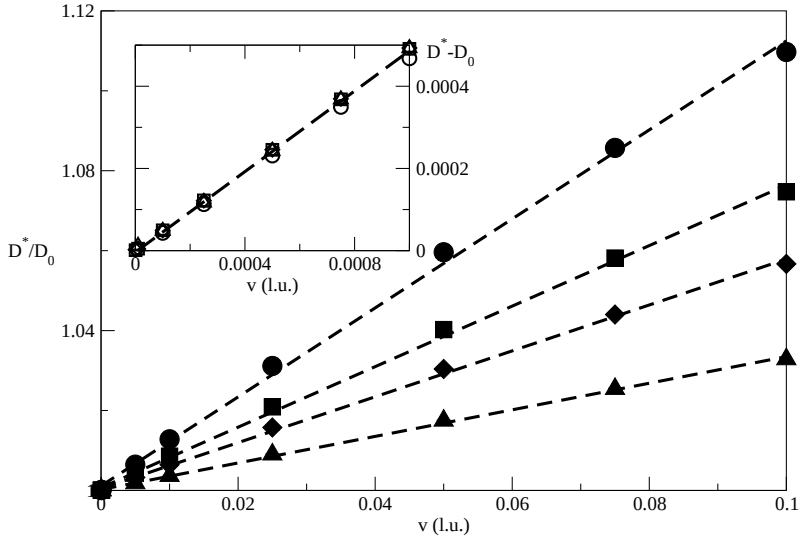

Figure 5.2: In the lattice-Boltzmann model, advection causes some spurious diffusion. The figure shows the computed effective diffusion D^*/D_0 as a function of the fluid velocity for the steady state described in Sec. 5.2.1. The curves are drawn for different diffusion coefficients at zero velocity: $D_0 = 0.38$ (circles), $D_0 = 0.57$ (squares), $D_0 = 0.76$ (diamonds), and $D_0 = 1.34$ (triangles). In the inset we show that the amount of diffusion induced by the flow does not depend on the equilibrium coefficient and has, for small velocities, a linear velocity dependence. Symbols are the simulation results and the dashed line corresponds to the theoretical expression described in the text.

diffusion coefficient achievable is given by the spurious diffusion (we put the proper diffusion coefficient to zero). Then, by substituting the expression for the spurious diffusion into the definition of the Peclet number, we obtain

$$Pe = \frac{vl}{D} \simeq \frac{vl}{\frac{1}{2}v - \frac{1}{2}v^2} = \frac{2l}{1-v}. \tag{5.26}$$

For reasons of flow stability, the quantity 1-v will always be of order 1. Therefore the maximum Peclet number achievable will be $Pe \simeq 2l$. In other words, a tracer will be able to travel a distance twice the obstacle size without feeling any diffusion.

5.5.2 Electrolyte in a slit

Next, we consider a fluid confined between two parallel solid walls at rest, with a constant surface charge. The slit has a width L and the surface density charge is fixed to $\rho(-L/2) = \rho(L/2) = \sigma/2$.

The space between the two slits is occupied by a solvent and counterions. In order to achieve global neutrality, the counterion density is initially set to be uniformly distributed, $\rho(x) = -\sigma/L$, $x \in \{-L/2, L/2\}$.

The actual position of the hydrodynamic and electrostatic solid boundary cannot be resolved within a lattice spacing. In the neutral case, for the viscosity and geometry considered the wall can be assumed to be halfway between two consecutive lattice nodes, as dictated by the bounce-back rule[8]. We will use this position as a reasonable approximation. In fact, the results we describe for a planar slit indicate that for a planar wall the electrostatic position of the wall can be taken as being midway between the boundary nodes. For a non planar interface a separate calibration will be required.

Equilibrium distribution of the counterion density

In equilibrium, a uniform charge density on a flat wall will induce an inhomogeneous equilibrium density profile of the counterions. For this simple geometry, the charge-density profile of the counterions is known analytically known (at least, at the Poisson–Boltzmann level) [22, 49] for an arbitrary surface charge density:

$$\rho(x) = \frac{\rho_0}{\cos^2(Kx)}, \tag{5.27}$$

where $\rho_0 = K^2/2\pi l_B$, K is the solution of the transcendental equation,

$$\frac{KL}{2}\tan\left(\frac{KL}{2}\right) = \pi l_B L\sigma, \tag{5.28}$$

which involves the wall charge density. Since we have an exact solution for the full Poisson–Boltzmann equation for arbitrary values of the wall charge, this geometry is a good case to analyze the limitations of the model dealing with large charges, i.e., beyond the linear Poisson–Boltzmann limit. For low surface charge densities, the linear regime is recovered by linearizing Eq.(5.28), and the parameter K becomes $K_{lin}L = \sqrt{4\pi l_B \sigma}$.

In the opposite limit of high surface-charge density, K saturates at $K_{sat}L = \pi$. We can then quantify the deviation of the fluid from the linearized regime, where the electrostatic interactions are small, by analyzing the departure of KL from $K_{lin}L$.

In Fig. 5.3.A we show the equilibrium counterions distributions in both limits. In our simulations we fixed the Bjerrum length to be 0.4, the channel width to 20 lattice nodes, and we have varied the surface-charge density. In the plot we show the profiles for $K/K_{lin} = 1.01, 1.13$, and 2.01, which correspond to $\sigma = 0.003125$, 0.03125 and 0.3125 in dimensionless lattice units, respectively. The highest value of K is not far from the saturation value. The figure shows that, with the present method, we can indeed reproduce the correct counterion distribution, both in the linear and in the non linear regime. In Fig. 5.3.B we compare the density profiles close to the wall in the non linear regime for two different slit widths. The larger the surface charge the more localized the charge profile will be. The figure shows that increasing the resolution of the lattice does result in a small but significant improvement in the calculation of the charge distribution. Of course, the discrepancy would be greater for a more localized charge profile. In practice, only the computer resources (memory) will set an upper limit for the surface charge density that can be modeled reliably with the present scheme.

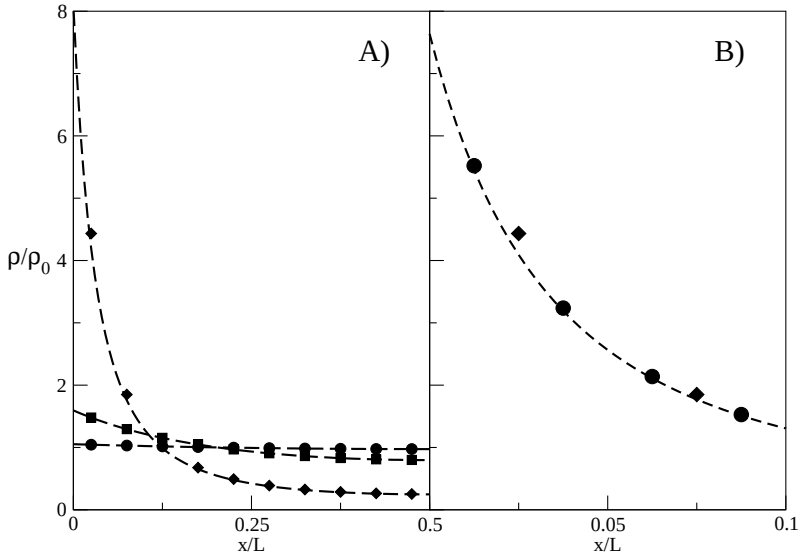

Figure 5.3: Equilibrium distribution of the charge density of counterions (no added salt) in the slit between two charged walls at a distance L. The abscissa measures the distance from the wall in units of L. The local density is expressed in units of the average charge density in the bulk: $\rho_0 = \sigma/L$. A) charge distributions for three values of the dimensionless parameter KL (see the text): $KL = 0.553$ (circles), $KL = 1.57$ (squares), and $KL = 2.77$ (diamonds). In the same figure, we have indicated the corresponding analytical results [Eq.(5.27)] (dashed curves) for a slit of width $L = 20$ lattice spacings. Circles and squares correspond to the linear regime ($K/K_{lin} = 1.01$ and 1.13, respectively), while diamonds are close to the saturation limit ($K/K_{lin} = 2.01$). B) The accuracy of the numerical solution for the charge profile can be improved by increasing the spatial resolution of the lattice, in this case from L=20 (diamonds) to L=40 (circles). Again, the analytical result is shown as a dashed curve. The curves in B correspond to the result for a highly charged surface, $KL = 2.77$ ($K/K_{lin} = 2.01$).

Electro-osmotic flow

Having verified that the model correctly reproduces the equilibrium behavior, we next turn to the calculation of flow caused by an external electric field. We apply a constant external electric field that is parallel to the slit, $E^{||}$. This field causes hydrodynamic flow as it exerts a force on those fluid elements that carry a net charge. If we take y as the component along the walls and refer to x as the coordinate perpendicular to the walls, then, at the Poisson–Boltzmann level, the exact solution for the fluid flow in the steady state can be written as [49]:

$$v_y(x) = \frac{eE^{||}\rho_0}{\eta K^2} \log\left[\frac{\cos(Kx)}{\cos\left(\frac{KL}{2}\right)}\right], \tag{5.29}$$

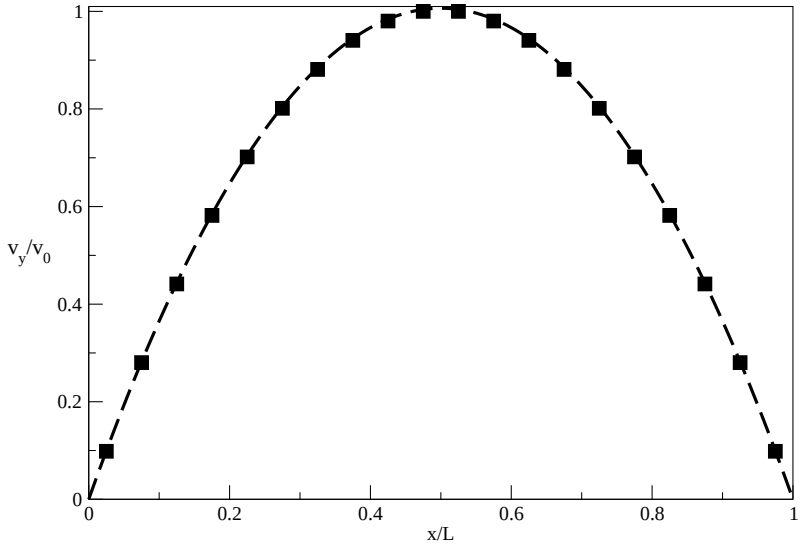

Figure 5.4: Electro-osmotic flow profile in a slit of width $L = 20$ lattice spacings. The surface charge density, $\sigma = 0.003125$ $(K/K_{lin} = 1.01)$, corresponds to the linear regime. The fluid in between the slit contains only counterions. The electric field is along the y direction. It has a strength of 0.1 in units $k_BT/(\Delta l e)$, where Δl is the lattice spacing and e is the elementary charge. The simulation results are compared to the theoretical prediction, Eq. (5.29), shown as a dashed curve.

where η is the shear viscosity of the fluid. In our simulations, we model the constant electric field by taking into account the potential difference that it causes between neighboring lattice nodes [i.e. $\Delta\widehat{\Phi}_{ext}(y) = E^{||}\Delta y$]. Figure 5.4 shows the computed electro-osmotic flow profile in a slit confined by hard walls with a charge density $\sigma = 0.003125$ (in units of the elementary charge per square lattice unit). In the same figure, we also show the analytical solution [Eq. (5.29), with $K/K_{lin} = 1.01$] that is exact in the Debye–Hückel limit. Again, there is good agreement between theory and simulation. This suggests that the effect of electrostatic forces on the hydrodynamic flow is correctly taken into account in the simulations.

5.5.3 Sedimentation velocity

In the previous sections we have seen that the appropriate equilibrium charge distribution is reproduced both in the linear and non linear regimes of the Poisson–Boltzmann equation, and that also a charge distribution induces the correct fluid profiles. We must still show that the opposite coupling works correctly, i.e., we must compute the hydrodynamic drag on a charged object, in the absence of external electrical fields.

To this end, we compute the sedimentation velocity of an array of charged spheres immersed in an electrolyte solution. In this case, the velocity of the colloidal particle induces a fluid flow that determines the steady charge distribution around the sphere.

This charge distribution, in turn, affects the sedimentation velocity of the particle. Hence, all the different couplings between charge, electrostatic potential, and fluid flow are present. Such a scenario has been analyzed previously with a different model [50] and analytically at infinite dilution [27]. As a consequence, we can again check our simulations against known results.

The system that we consider consists of a charged sphere of radius a in a three-dimensional box of size L. Because of periodic boundary conditions, this corresponds to a periodic array of spheres with volume fraction $\varphi = (4\pi a^3/L^3)$. In the simulation, we first allow the electrolyte to equilibrate with the particle at rest in the absence of external forces; hence the system develops its equilibrium double layer. Then, we apply the gravity as an external body force applied to the fluid, i.e., we move in the system of reference of the colloid. In this way we avoid the problem of updating the particle's position due to its motion [13]. By forcing the colloid to be at rest, we will not conserve momentum, but by computing the mean fluid velocity in the steady state (which is reached on a time scale of order $L^2\rho/\eta$), we can obtain the sedimentation velocity.

We have fixed the Bjerrum length to $l_B = 0.4$ and the radius of the sphere to $a = 4.5$ in lattice units. We performed calculations for two different values of the solvent fluid density, $\rho_s = 1$, and $\rho_s = 20$, while the density of the added salt ρ_k was varied between 1.8×10^{-2} and 4×10^{-4}. As we vary the salt concentration, we also change the Debye length from 3.3 to 21. In order to be sure that the equilibrium properties were correct, we have computed the co- and counterions equilibrium-densities-distributions and found very good agreement with the ones predicted by the Debye-Hückel theory for all the Debye lengths considered. In particular, spheres with radius 4.5 lattice units are well described by their approximate lattice representation. Since $\rho_s \gg \rho_k$, we have performed most calculations using the second version of our simulation scheme, as described at the end of Sec. 5.2.2. However, we also performed some simulations using the original model (taking the solvent density as the overall density). The only difference that we observe between the two implementations is a small variation in the numerical value of the sedimentation velocity. However, this difference already shows up for sedimentation of a neutral sphere. It is due to a small change in the fluid viscosity that is caused by a small difference in the overall fluid density in the two implementations. The valency of the macro ion was chosen to be $Z = 10$, which corresponds to the small charge limit. Although our computational scheme should also work outside the Debye–Hückel limit, we restrict ourselves to this regime, because it is only in this limit that we can compare with existing analytical results. Specifically, Booth predicted that the sedimentation velocity, $U_0(Z)$, of a weakly charged sphere of valency Z in the dilute limit can be expressed as [27]

$$\frac{U_0(Z)}{U_0} = 1 - c_2 Z^2, \tag{5.30}$$

where U_0 is the sedimentation velocity of a neutral sphere, and c_2 is a constant that can be computed analytically in the Debye–Hückel limit. For the simplified situation of monovalent co- and counterions, $z_+ = -z_- = 1$, which have the same diffusivity,

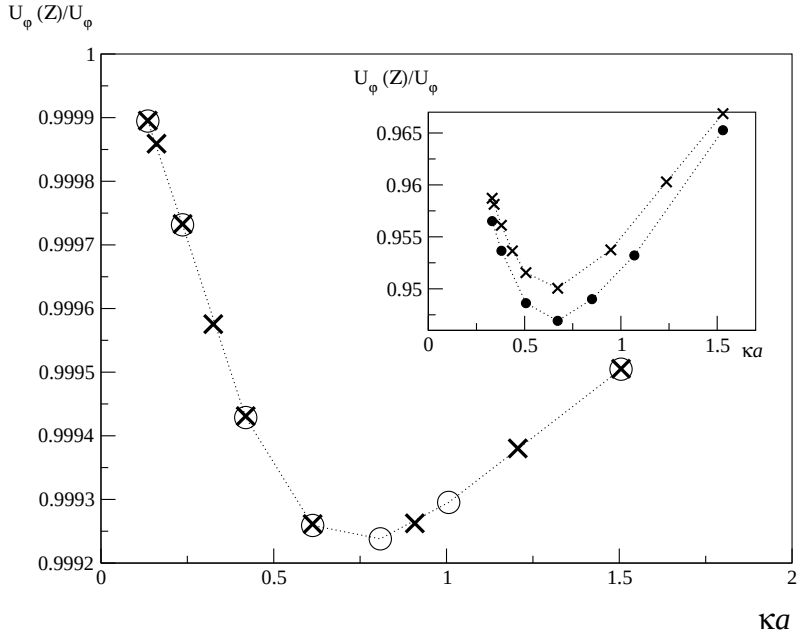

Figure 5.5: Reduced sedimentation velocity of a periodic array of colloids of valency $Z = 10$ in an electrolyte as a function of κa. The figure shows the results for two different values of the ionic diffusion coefficients. The curve for $D_0^{(1)} = 0.95$ (circles) has been rescaled to the curve for $D_0 = 0.19$ (x) according to Eq. (5.31), i.e., $U(D) = U(D_0^{(1)}) \times (D_0^{(1)}/D_0)$. The superposition of the two curves shows that the scaling is obeyed. In the inset we also show the results for a colloid of valency $Z = 100$. However, in this high-charge regime the sedimentation velocity does not scale with the diffusion coefficient in the way predicted by the linearized theory. The dotted lines are a guide to the eye.

$D_+ = D_- = D$, the expression for c_2 simplifies to

$$c_2 = \frac{k_B T l_B}{72\pi a^2 \eta D} f(\kappa a), \tag{5.31}$$

where $f(\kappa a)$ is a linear combination of exponential integral functions [50] and is a function of the inverse Debye length, $\kappa = \lambda_D^{-1} = \sqrt{4\pi l_B \sum_k z_k^2 \rho_k}$. We have checked that the sedimentation velocity scales as predicted with the viscosity. We have also verified that we are indeed in the linear regime where the sedimentation velocity is proportional to the applied gravitational field. In particular, for the two values of the density considered, ρ_s, the linear regime was obtained for forces per unit of volume such that the flow velocity never exceeded 0.1 in lattice units. Figure 5.5 shows the sedimentation velocity of a weakly charged sphere ($Z = 10$) as a function of the inverse Debye screening length. As can be seen from the figure, the sedimentation velocities scales with the ionic diffusivity in the way predicted by Eq.(5.31). The inset in the same figure shows that this scaling breaks down at higher colloidal charges ($Z = 100$), i.e.,

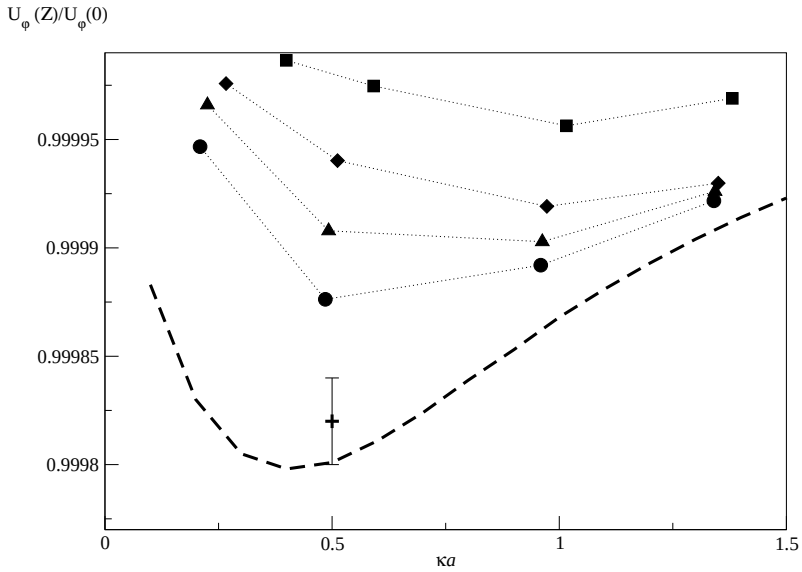

Figure 5.6: Sedimentation velocity of a periodic array of spheres of valency $Z = 10$ and hydrodynamic radius $a = 4.3$. The Bjerrum length $l_B = 0.4$ (in lattice units). The diffusion coefficient of both positive and negative ions is set to $D = 0.19$. We compare simulation results for finite volume fractions, namely 0.0416 (squares), 0.0123 (diamonds), 0.00521 (triangles), and 0.00267 (circles) against the Booth theory, which is valid at infinite dilution (dashed curve). For $\kappa a = 0.5$ we also show the estimated value of the sedimentation velocity at infinite dilution (see the text). The point corresponds to the extrapolation of the law, Eq. (5.33). Within the estimated error, the extrapolated simulation results agree with the predictions of Ref. [27]. The dotted lines are a guide to the eye.

outside the range of validity of the linearized Poisson–Boltzmann description. Figure 5.6 shows the reduced sedimentation velocity $[U_\varphi(Z)/U_\varphi(Z=0)]$ as a function of κa for a range of volume fractions. As the volume fraction decreases, the curves approach Booth's infinite-dilution result, while the minimum sedimentation velocity moves toward the minimum value predicted by theory. In order to compare quantitatively the simulation results with Booth's theory, Eq. (5.30), we must extrapolate the computed values for $U_\varphi(Z)/U_\varphi(Z=0)$ from the finite φ values of the simulations to the infinite-dilution limit, $U_0(Z)/U_0(Z=0)$. For neutral spheres Hashimoto has shown that that the sedimentation velocity converges very slowly to its infinite-dilution value, namely, as [56]

$$\frac{U_\varphi(Z=0)}{U_0(Z=0)} = 1 - 1.7601\varphi^{1/3} + \varphi + O(\varphi^2). \tag{5.32}$$

Ladd has numerically verified this dependence [57]. For charged spheres, due to the electrostatic screening, we still expect that the dominant φ dependence comes from excluded volume; previous results indicate that this is indeed the case [50]. When performing the dilute limit expansion, we therefore decided to single out the major

volume fraction dependence by normalizing the simulation results with the Stokes drag coefficient, i.e., computing the low-density limit of $U_\varphi(Z)/U_0(0)$. As a result, it is reasonable to obtain the same functional dependence on φ as Hashimoto with a slightly different amplitude. Specifically, we expect

$$\frac{U_\varphi(Z)}{U_0(0)} = 1 - (1.7601 + \epsilon)\varphi^{1/3} + O(\varphi^{2/3}), \tag{5.33}$$

where ϵ is much less than one. Eventually, the dilute limit is obtained by extrapolating Eq.(5.33) to $\varphi = 0$.

In Fig. 5.6 we show the extrapolated sedimentation velocities for a particular value of κa. The estimated error in the limiting sedimentation velocity is rather large. It could have been reduced by computing more values of the sedimentation velocity at low volume fractions. In addition, there is some uncertainty in the value of the effective sphere radius. In light of these uncertainties, the agreement with the Booth limit in Fig. 5.6 is gratifying.

5.5.4 Absence of spurious fluxes

We pointed out in Sec. 5.2 that one of the incentives for developing the present model was to eliminate any mixing of continuous-space gradients and discretized gradient operators. The reason is that the inevitable approximations associated with the discretization of gradient operators usually lead to the appearance of spurious mass and momentum fluxes, even in equilibrium. Such spurious fluxes are present, in particular, whenever there exist spatial inhomogeneities related, for example, to the presence of liquid interfaces. In the present approach, we only use lattice-gradient operators that have been constructed such that, in equilibrium, no flow can result. To demonstrate the effect that this has, we compare the present method with an existing "mixed" method. In particular, we consider a spherical colloid of radius $a = 4.5$, at rest in an electrolyte in a cubic box of diameter $L = 20$. The valency of the sphere is $Z = 10$ and the system as a whole is electrically neutral. In Fig. 5.7 we show the projection of the momentum flux in the equatorial plane of the sphere and compare these residual fluxes both for the model introduced in this paper and the model of Ref. [50]. Figure 5.7a shows that spurious currents, although small, are certainly not negligible in this case. Moreover, their magnitude is clearly correlated with the distance to the colloidal particle: the largest currents appear in the region where the spatial gradients are largest. For highly charged spheres (i.e. outside the linear Debye-Hückel regime) these spurious fluxes will become larger. In contrast, in Fig. 5.7b (the present model), the spurious fluxes are at the level of machine precision. In fact, to make them visible at all, we had to multiply the momentum fluxes by a factor 10^{13} relative to the old model. In other words, the residual fluxes are controlled by machine accuracy. Even at this level one cannot detect a correlation between the fluxes and the position of the sphere. We can conclude that the proposed model eliminates the appearance of spurious equilibrium fluxes.

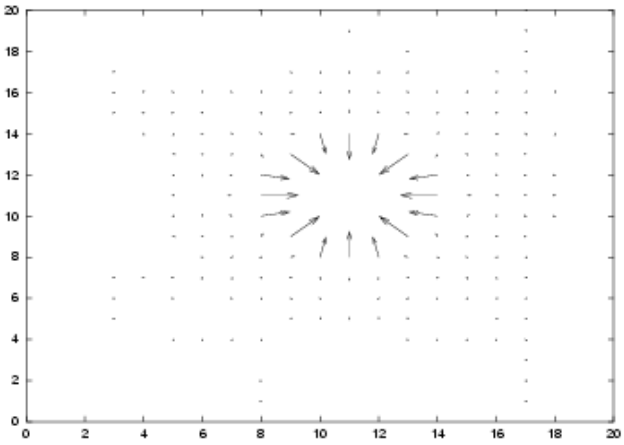

(a)

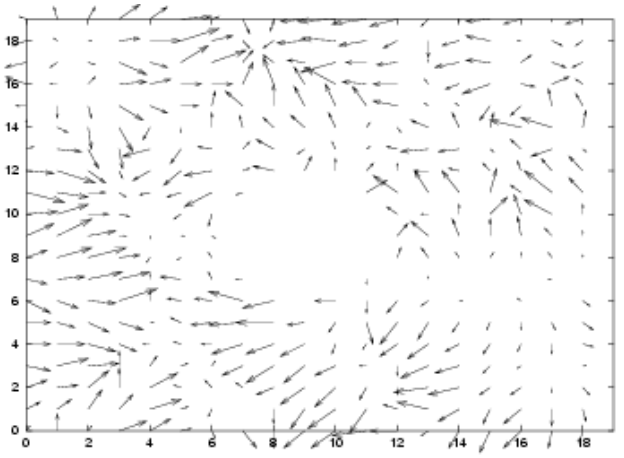

(b)

Figure 5.7: An Illustration of suppression of spurious boundary currents in the present LB model. In the figure we compare the apparent currents in equilibrium for two models: figure (a) gives the results for the model described in Ref. [50]; (b) shows the results for the present model. In both cases we consider a colloidal sphere of radius 2.5 *in a system with a diameter* $L = 20$ *lattice spacings. As there are no external forces acting on the system and the colloid is not moving, the fluid is supposed to be at rest. The figure shows the measured projection of the momentum flux in the equatorial plane of the colloid. In (a), spurious currents are apparent close to the particle surface. The spurious currents in case (b) are much smaller than in case (a). In fact, to make them visible at all, they have been scaled up by a factor* 10^{13} *with respect to case (a). This is an indication that the spurious currents in case (b) have been suppressed down to machine accuracy.*

Conclusions and discussion

We have introduced a new model to simulate the collective dynamics of non ideal fluid mixtures, with a special emphasis on its use to study electrokinetic phenomena. The method relies on a lattice-Boltzmann model, where the interactions are introduced as effective forces. In this respect, our model resembles a Vlasov kinetic model, as opposed to previous kinetic lattice models. In our approach the fluxes between neighboring lattice nodes are the fundamental dynamical objects that couple external fields to both electrical conduction and hydrodynamic flow.

As a result of the symmetric formulation of the flux between neighboring nodes we can impose strict local mass conservation. As a consequence, the present model is free of spurious boundary fluxes that plague all other lattice-Boltzmann models of fluid mixtures. Moreover, a link-based description has the additional advantage that boundary conditions are easily implemented.

Second, by using a multistep approach, we can vary ionic mobilities over many orders of magnitude. This feature of our model allows us to explore electroviscous effects over a wide range of Peclet numbers. We have shown that flow causes spurious advection–diffusion. However, this effect is well understood and can be made negligible in most practical cases.

We have checked the performance of the model by studying equilibrium diffuse layers, showing that it is possible to recover both low- and high-charge density regimes. In the latter, the only limitation is related to computational resources, because a finer grid is required to resolve the narrower charge profiles that develop nearly highly charged walls. To test the coupling of electrostatics and fluid flow, we have computed the sedimentation velocity of a charged sphere. These simulations indicate that the existing theoretical predictions are reproduced in the low-charge, low-density limit. As the charge of the colloid is increased, the simulation results start to deviate from the theoretical predictions that apply in the linearized Poisson–Boltzmann regime.

Even though in the present paper we have focused on electrostatic interactions and, in particular, we have not discussed molecular interactions that favor demixing, such interactions could also be incorporated in the present model.

6 Sedimentation velocity of highly charged spheres

Abstract

In this Chapter, I discuss the sedimentation velocity of a highly charged spherical colloid in an electrolyte. First, I briefly discuss "charge localization" for highly charged colloids. Second, I show the consequences of this localization on the co- and counterions equilibrium charge distributions. I then discuss the reduction in sedimentation velocity of a highly charged sphere. As the surface charge σ is increased, we observe a cross-over from a region where the variation in sedimentation velocity is quadratic in σ, as predicted in the Debye-Hückel limit, to a region where the dependence upon the surface charge is either linear or logarithmic. We argue that this switch to a quasi linear reduction in the sedimentation velocity is related with the increasing localization of the charge distributions. We find that the use of the effective surface charge in the interpretation of the sedimentation velocity of highly charged spheres, improves only marginally the range of applicability of the non-equilibrium theories based on the Debye-Hückel limit.

6.1 Introduction

In this chapter, I exploit the method introduced in Chapter 5 to study the effect of the charge on the sedimentation velocity of a highly charged macroparticle, immersed in an electrolyte. For electrolytic solutions, I already presented the governing equations in Section 3.3. In principle, one could use these equations to compute the distribution of microions near a macroscopic particle. Although solutions are only available in the Debye-Hückel regime, which is valid if the electrostatic potential Φ is everywhere small (i.e. $e\Phi \ll k_B T$). However, even for highly charged particles, there will always be a region where the Debye-Hückel theory is accurate because the electrolyte screens the charge. This region has been used by several authors [58, 59, 60] to extrapolate to the value of the electrostatic potential at contact. For highly charged spheres (see, e.g. [61, 62]) there is an effective accumulation of the counterions near the charged particle. This effect is distinct to Manning condensation [63, 64] which is the phenomenon of charge condensation near charged cylinders. Yet, some of the consequences are similar.

This localized layer is also distinct from the Stern layer. The latter has spatial extension of the order of the radii of the microions and cannot therefore be described in terms of a Boltzmann equilibrium, where the particles are taken to be point like.

The localization mechanism, which we discuss here, is entirely described in terms of the Poisson-Boltzmann formalism.

6.2 Charge localization for non rod-like particles

Let us recall the relevant equations. To simplify the notation we use the dimensionless electrostatic potential $U = (e/k_BT)\Phi$, and the Bjerrum length $l_B = e/4\pi\epsilon k_BT$, where ϵ is the dielectric constant of the medium. The equilibrium concentration for monovalent co- and counterions in the presence of an electric field is approximated by the Boltzmann equilibrium [cf. Eq. (3)]

$$\frac{n_\pm(\mathbf{r})}{n_0} = e^{\mp U(\mathbf{r})}, \tag{6.1}$$

while the electrostatic potential is computed by solving the complete Poisson-Boltzmann equation (PB)

$$\nabla^2 U(\mathbf{r}) = 4\pi l_B n_0 \left[e^{U(\mathbf{r})} - e^{-U(\mathbf{r})}\right]. \tag{6.2}$$

In the Debye-Hückel theory, the electrostatic potential is supposed small ($U \ll 1$), and the exponential in Eq. (6.2) can be approximated as

$$e^{\pm U(\mathbf{r})} \simeq 1 \pm U, \tag{6.3}$$

which leads to the linearized Poisson-Boltzmann equation (LPB)

$$\nabla^2 U(\mathbf{r}) = 8\pi l_B n_0 U(\mathbf{r}). \tag{6.4}$$

Equation (6.4) has the solution for a the potential near a flat, charged surface $U(z) = U_0 \exp(-\sqrt{8\pi l_B n_0}z)$. For a sphere $U(r) = U_0(a/a+r)\exp(-\sqrt{8\pi l_B n_0}r)/r$ (where U_0 is the electrostatic potential at contact and r is measured from the sphere surface). The approximation (6.3) has the consequence that the co- and counterions density distributions, are not given by the full PB solutions

$$\frac{n_\pm^{\mathrm{PB}}(\mathbf{r})}{n_0} = e^{\mp U(\mathbf{r})}, \tag{6.5}$$

but by

$$\frac{n_\pm^{\mathrm{LPB}}(\mathbf{r})}{n_0} = 1 \mp U(\mathbf{r}). \tag{6.6}$$

For small $U(r)$ the two equations are equivalent, but in the presence of an highly charged macroscopic object, the two expressions predict drastically different equilibrium distributions when $|U| > 1$. Nonetheless, due to the screening of the charge, it is still true that, at large enough distances (in practice when, again, $|U| \ll 1$), the linearized Poisson-Boltzmann equation is a good approximation, and the two solutions (6.5) and (6.6) are indistinguishable. Thus, we can define a distance r_0 such that for any $r \geq r_0$, $n_\pm^{\mathrm{LPB}} \simeq n_\pm^{\mathrm{PB}}$. The region of charge accumulation is naturally defined as

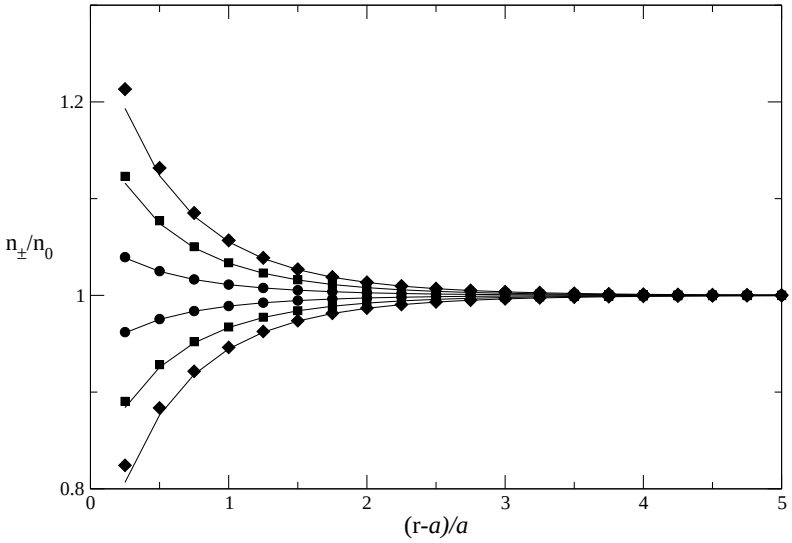

Figure 6.1: Computed $n^{\mathrm{PB}}(r)/n_0$ (symbols) and approximate $n_{\pm}^{\mathrm{LPB}}(r)/n_0 = 1 \mp U^{\mathrm{PB}}$ (continuum lines) for a surface charge 0.005 *(circles),* 0.015 *(squares), and* 0.025 *(diamonds). Distance are measured from the surface of the sphere.*

the region $r \leq r_0$. If, on the other hand, $r_0 = 0$ —in other words, if the LPB gives accurate results in the whole space—there are no localized counterions.

Although the equilibrium distributions of co- and counterions have been known for centuries, we show the result of a computer simulation for an array of spheres with a twofold purpose. On the one hand, we use them to illustrate the difference between the full and the linearized Poisson-Boltzmann equations. On the other hand, we will use these equilibrium properties as an explanation for the non equilibrium dependence of the sedimentation velocity upon the surface charge. The details of the simulation method are presented in Chapter 5. The array is made of spheres of radius $a = 4$ at the volume fraction 1.2×10^{-3}, with Bjerrum length $l_B = 0.4$, $\kappa a = 1$, and (for future reference) the diffusivity of the ions making the 1-1 electrolyte is $D = 0.038$.

We directly computed the n^{PB}, while we the n^{LPB} are obtain from Eq. (6.6). Because for the potential $U(r)$ we substituted the numerical solution of the non-linear PB, in fact, our $n_{\pm}^{\mathrm{LPB}}$ is only an approximate solution of the LPB. Strictly speaking the electrostatic potential should be consistently computed from the LPB. However, this does not constitutes a serious approximation in that, although n^{LPB} and n^{PB} are very different, because of the exponential present in Eq. (6.5), the electrostatic potential Φ^{LPB}, solution of the LPB, will not differ too much from the Φ^{PB}, solution of the full PB. In Figure 6.1 we show the co- and counterions equilibrium distribution functions for a weakly charged spheres with increasing surface charge (the symbols represents the n^{PB}, while the continuous lines the n^{LPB}). For the smallest value of the surface charge ($\sigma = 0.05$), the two curves are indistinguishable, which shows that the LPB gives, in this limit, a very accurate representation of the full PB. When the surface

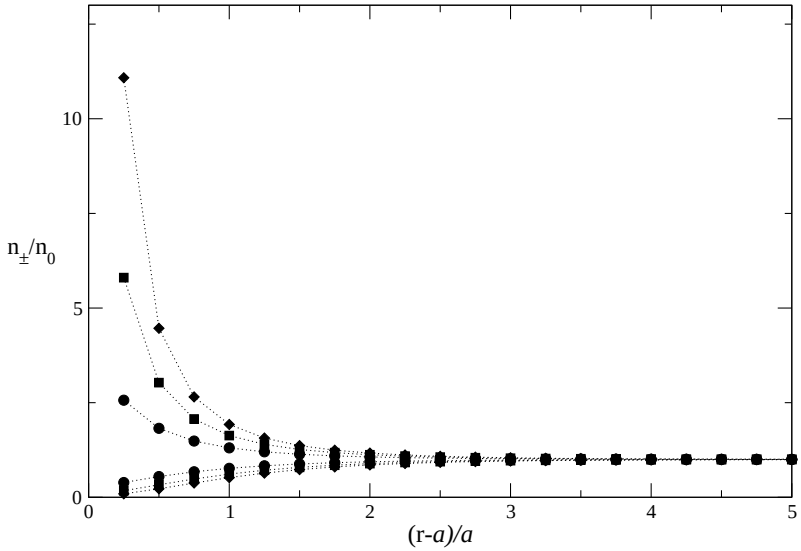

Figure 6.2: $n_{\pm}^{\mathrm{PB}}(r)/n_0$ *for a moderately charged sphere of surface charge* 0.12 *(spheres),* 0.25 *(squares), and* 0.37 *(diamonds). The dotted lines are a guide to the eye.*

charge is small, a minor modifications of the uniformly distributed distribution density is sufficient to screen the colloid charge and both co- and counterions participate, with a comparable quantitative role, in the screening. It is important to remember that the equilibrium distribution function of the counterions (coions) is given by the competition between the electrostatic attraction (repulsion) and the entropy, the latter of which favors an homogeneous distribution of the densities (see also Chapter 3).

When the surface charge increases, the combined effect of electrostatics and entropy becomes visible through an asymmetric equilibrium distributions of the microions. On average, the counterions, being closer to the sphere, will feel a higher electric field. This effect starts to manifest itself at the larger value of surface charge in Figure 6.1 and it is definitely visible in Figure 6.2. In this figure, we can see the asymmetric distribution of the co- and counterions due to the competition between entropy and Coulomb interaction. Such an asymmetric distribution, will never be present in the linearized Poisson-Boltzmann equation because of Eq. (6.6).

If we keep increasing the surface charge (Figure 6.3), we can observe (see also the inset) that the coion density hardly changes with increasing surface charge, because most of the extra charge is already screened by the counterions near the sphere. The concentrations of counterions, on the contrary, keeps increasing with increasing surface charge, but only near the surface. It is as if all the extra counterions, needed to maintain charge neutrality, are localized near the surface.

In this last scenario, it is apparent that the result for n^{LPB} and n^{PB} are drastically different. This is shown in Figure 6.4a, where the continuous curve represents $1 \pm U^{\mathrm{PB}}(r)$. Near the surface, the LPB even predict an (unphysical) negative number

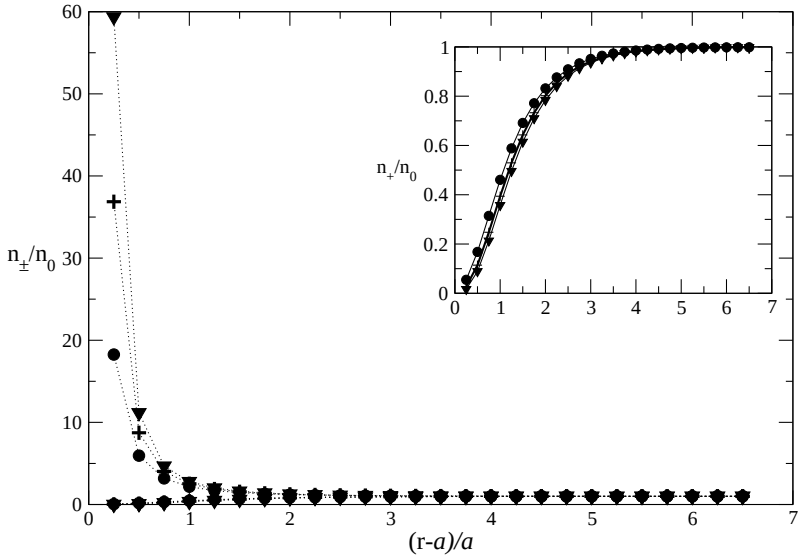

Figure 6.3: $n_{\pm}^{\mathrm{PB}}(r)/n_0$ *for a highly charged sphere of surface charge* 0.48 *(spheres),* 0.75 *(squares), and* 0.99 *(diamonds). In the inset we show the coion density near the surface of the sphere. The dotted lines are a guide to the eye.*

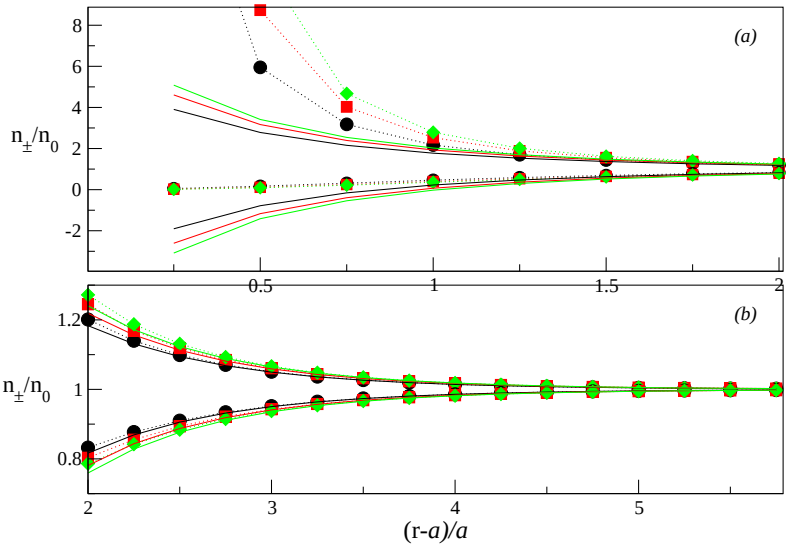

Figure 6.4: Computed $n^{\mathrm{PB}}(r)/n_0$ *(symbols with dotted lines as a guide to the eye) and approximate* $n_{\pm}^{\mathrm{LPB}}(r)/n_0 = 1 \mp U^{\mathrm{PB}}$ *(continuum lines) for a charged sphere of surface charge* 0.48 *(circles),* 0.75 *(squares), and* 0.99 *(diamonds). We show in detail the region where the approximate and exact equilibrium distribution densities disagree (a) and the one where they agree (b). Distances are measured from the surface of the sphere.*

density of coions. Nevertheless, even in this limiting scenario, there exists a distance beyond which the LPB approximation gives a good estimate for the charge distributions (Fig. 6.4b).

6.3 Sedimentation velocity

In the present section we consider how the sedimentation velocity depends on the surface charge σ; with special attention to high surface charges. Let us begin by recalling the sedimentation theory given in Chapter 3. Booth [27] predicts that the sedimentation velocity $V(Z)$ of a weakly charged sphere of valency Z can be expressed as

$$\frac{V(Z)}{V(0)} = 1 - c_2(\kappa a)Z^2, \tag{6.7}$$

$$c_2(\kappa a) = \frac{k_B T l_B}{72\pi a^2 \eta D} f(\kappa a), \tag{6.8}$$

where $V(0)$ is the sedimentation velocity of a neutral sphere, c_2 is computed in the Debye-Hückel limit for the simplified situation of a symmetric 1-1 electrolyte, and $f(\kappa a)$ was explicitly given in Section 3.2.2. κ is the inverse Debye length, $\kappa = \lambda_D^{-1} = \sqrt{4\pi l_B \sum_k z_k^2 n_k}$ and we make use of the dimensionless length κa. We fix $\kappa a = 1$ (the value around which the effects of electrohydrodynamics is the largest) and study the surface charge dependence of

$$\Upsilon(\sigma) \equiv 1 - \frac{V(Z)}{V(0)} = A\sigma^2. \tag{6.9}$$

In Equation (6.9) $A = c_2(1)(4\pi a^2)^2$, while $\sigma = Z/(4\pi a^2)$ is the surface-charge density of the sphere. In Figure 6.5 we show the computed $\sigma-$dependence of $\Upsilon(\sigma)$. For weakly charged colloid, the prediction of the Booth theory [Eq. (6.9)] is qualitatively confirmed, as shown in the inset of the graph. However, a completely different surface-charge dependence is present for highly charged spheres. Specifically, we observe a cross-over region (from values of the surface charge ranging from $\sigma \simeq 0.1$ to $\sigma \simeq 0.4$) followed by a region where the increase in Υ is approximately linear with σ. Although, to our knowledge, this behavior is not well understood in general, Ohshima *et al.* [65] give an analytic formula valid in the limit $\kappa a \to \infty$ where they predict a constant value for an infinitely charged sphere.

For surface charges of the order of 0.1 there is no symmetry between the co- and counterions densities. It seems likely that the observed behavior of $\Upsilon(\sigma)$ reflects the behavior of the microion densities.

We can make a 1-1 correspondence with the three regimes already identified. In the low charge limit, where the theory predicts the observed σ^2 dependence, both equilibrium co- and counterions distributions are equally modified by the Coulomb force due to the charged sphere. In the cross-over region (between $\sigma \simeq 0.1$ and $\sigma \simeq 0.4$), the equilibrium charge distributions corresponding to the one of Figure 6.2, where the coion equilibrium distributions changes only slightly upon increasing the surface charge. Finally, upon further increasing the surface charge, we enter the region of

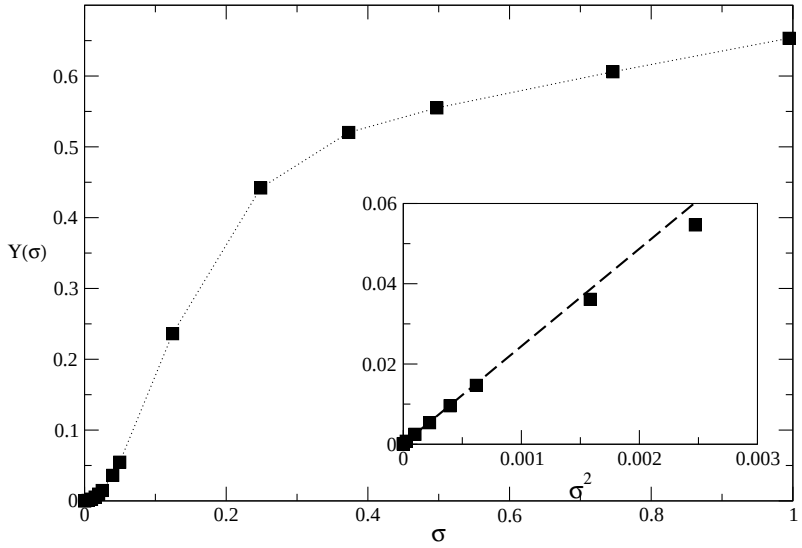

Figure 6.5: $\Upsilon(\sigma)$ *(symbols) as function of the surface charge* σ*, for* $\kappa a = 1$*. The dotted line is a guide to the eye. In the inset we show* $\Upsilon(\sigma)$ *for low value of* σ *versus* σ^2*; the inset show that the quadratic dependence, predicted by the Booth theory, is obtained. In the inset the dashed line is a linear fit of the simulation results for* $\sigma^2 < 0.001$*. The region between* $\sigma \simeq 0.1$ *and* $\sigma \simeq 0.4$ *is a cross-over region between the quadratic dependence of* Υ *with* σ *and a more linear one.*

charge "localization", where the coion equilibrium distributions hardly change upon incrementing the surface charge (see the inset of Figure 6.3). This suggest that, for large σ, only the counterion contributes to a further slowing down of the sedimentation velocity.

To test this idea, we repeated the simulation for a system with no-added salt. In Figure 6.6 we compare $\Upsilon(\sigma)$ for a system with and without added salt. The figure shows, that for surface charge larger than $\sigma \geq 0.5$ both curves have an approximately linear profile, although with a slightly different slope: $\simeq 0.2$ for the added salt curve and $\simeq 0.25$ for the no-salt curve. We should not expect quantitative agreement because, in the added salt case, the flow is, of course, also influenced by the coions.

Although, for the salt and the no-salt systems, we observed a similar dependence of $\Upsilon(\sigma)$ on σ for high surface charge, at small σ this is no longer true as shown in Fig. 6.7. In the inset, we show the exponent α, defined as the derivative of the log-log plot of $\Upsilon(\sigma)$, of the region close to $\sigma \simeq 0$. The inset shows that while the added-salt system has a quadratic dependence upon the surface charge, the no-salt one appears to have a dependence that is close to cubic.

Another strong indication that only the counterions are responsible for the reduction in the sedimentation velocity in the high surface regime comes from an experimental paper by Schumacher and Van de Ven [66]. These authors performed a series of sedimentation experiments for different types of salt, and showed that, for highly

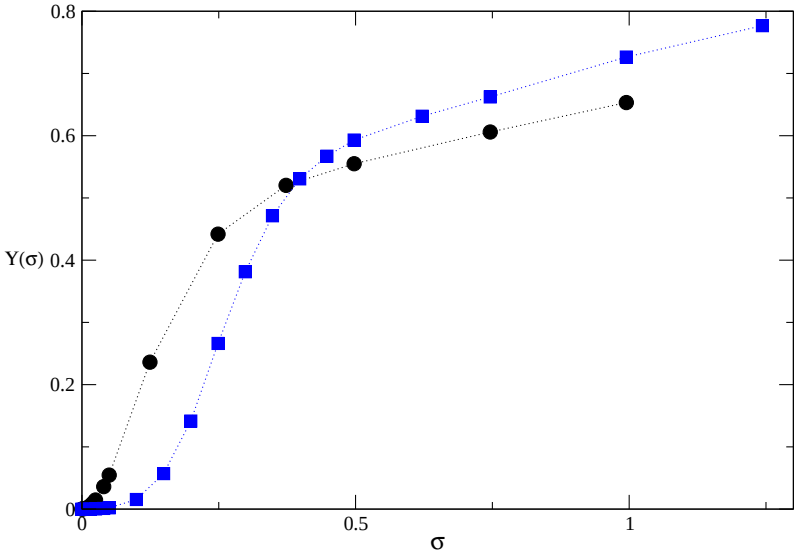

Figure 6.6: $\Upsilon(\sigma)$ as function of the surface charge σ, for $\kappa a = 1$ for a system with added salt (circles) and for a no-added salt one (squares). The dotted lines are guide to the eye.

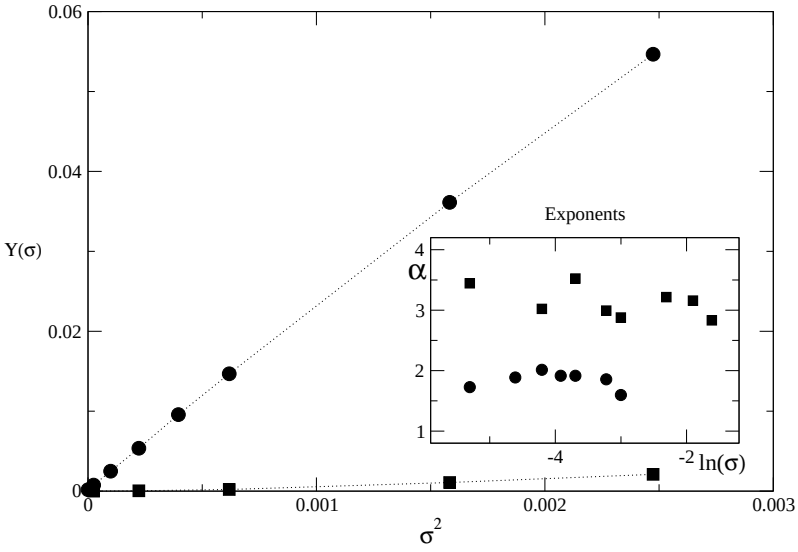

Figure 6.7: Comparison of the low-surface-charge dependence of $\Upsilon(\sigma)$ for a added- (sphere) and a non-added salt (squares) system. for $\kappa a = 1$. Lines are guide to the eye. The two system shows a different low-surface-charge dependence. In the inset we show the exponent of a supposed algebraic decay; the added salt system (sphere) shows the σ^2 dependence upon the surface charge predicted by the Booth theory, while the no-salt system shows a σ dependence closer to cubic.

charged colloidal spheres, the reduction in the sedimentation velocity does not depend on the properties (the diffusivity) of the coions.

6.4 Effective surface charge

In the previous section, I discussed the surface charge dependence of the sedimentation velocity of a sphere. However, sedimentation experiments are usually interpreted in terms of the Booth theory. Often, however, the surface charge of the experimental colloids is too high for the Booth/Ohshima theory to hold. In the absence of alternatives, the linear theory is still used. To fit experiments, one must assign an effective charge to the colloids. However many papers are skeptical about the usefulness of the concept of effective surface charge [24]. The standard procedure to define an effective surface charge is to use the relation between surface charge and electrostatic potential at contact U_0 (often referred to as the ζ potential) which is valid in the Debye-Hückel theory [31], i.e.

$$\frac{e\Psi_0}{k_BT} = \frac{e\widetilde{\sigma}\lambda_D}{\epsilon k_BT} \tag{6.10}$$

where Ψ_0 and $\widetilde{\sigma}$ are the dimensional electrostatic potential at contact and surface charge, respectively. Equation (6.10) is conveniently expressed by means of dimensionless quantities as

$$U_0 \equiv \zeta = 4\pi l_B \lambda_D \sigma. \tag{6.11}$$

In the high charge regime, however, this relation does not hold. Due to the presence of the condensed region of counterions, in fact, the ζ potential is smaller than the value given by the Eq. (6.11) [67]. One can the define an effective surface charge σ^* such that

$$\sigma^* \equiv \frac{\zeta}{4\pi l_B \lambda_D}. \tag{6.12}$$

To obtain the ζ potential, from the region where the LPB is a good approximation of the full PB, one extrapolates the electrostatic potential at contact, assuming that it retains the functional dependence predicted by the LPB (for spheres, the Yukawa potential). This would be meaningful if the sedimentation velocity would retain the charge dependence predicted by Booth and Ohshima [Eq. (6.7)] with respect to this effective surface charge. If a saturation value for the surface charge is reached, then the same would hold for the sedimentation velocity. In the following, we show that this expectation is, in fact, not supported by our numerical solution of the non-linear equations.

Figures 6.8, 6.9, and 6.10, show $U(r)/4\pi l_B\lambda_D$—which for $r = 0$ is the surface charge of the sphere [see Eq.(6.11)]—for increasing values of σ in the low, medium and high charge regimes, respectively. We observe that as Eq. (6.11) holds for weakly charged colloids, but this is no longer true for medium and highly charged colloids. In the same figures, we show the extrapolated values of the electrostatic potential, assuming that the Yukawa potential is valid everywhere. In other words, we fit the exact electrostatic potential where $\Phi \ll 1$ extrapolating to $r = 0$ with

$$U(r) = U_0 \frac{a}{a+r} e^{-\kappa r}, \tag{6.13}$$

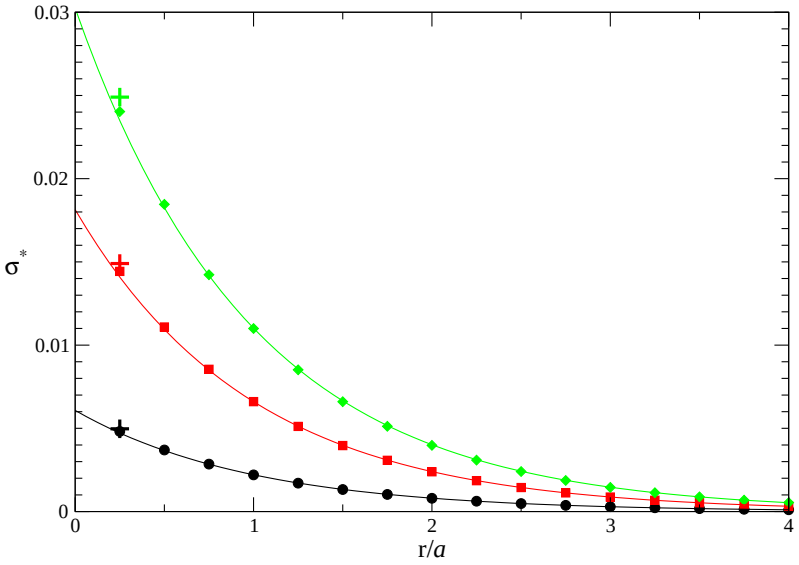

Figure 6.8: Effective surface charge for a weakly charged colloid. We plot $U(r)/4\pi l_B\lambda_D$ (such that $U(0)/4\pi l_B\lambda_D \equiv \zeta/4\pi l_B\lambda_D = \sigma^*$) for nominal surface charges equals to $\sigma = 0.005$ (spheres), $\sigma = 0.015$ (squares), and $\sigma = 0.025$ (diamonds). The symbols represent the computed electrostatic potential, while the continuous lines represents the extrapolation to contact of LPB (for this particular values of σ LPB holds everywhere). The plus symbols show the actual value of the surface charges.

where, again, the distance is measured from the surface of the sphere. The only adjustable parameter in this extrapolation procedure is U_0. It is, at first sight, very surprising that this approximate expression for the electrostatic potential is accurate even in the vicinity of the spheres, as one can see by comparing the continuous lines with the points. On the other hand, the fact that the expression relating ζ and σ is not accurate should not surprise the reader, because Eq. (6.11) assumes a weakly charged colloid, with little or no influence of the microions.

To test whether this renormalization of the surface charge leads to good agreement between the computed sedimentation velocities and the theory of Booth, we plot $V(Z)/V(0)$ versus σ^*. In Figure 6.11 we show the Booth prediction versus the surface charge. The three different curves represent three different ways of computing the surface charge. The spheres symbols is a repetition of the curve in Figure 6.5, where in the abscissa we plot the actual surface charge. Then, there are two ways of defining an effective surface charge by means of Eq. (6.12). The first, by using the computed electrostatic potential given by the full PB (filled diamonds symbols in the figure); the second, by using the approximate electrostatic potential given by the extrapolation from the solution of the LPB (open square symbols in the figure). Although the curves with the effective surface charge are somewhat closer to the Booth theory prediction, they still do not show a σ^2 dependence. Because we can compute all the

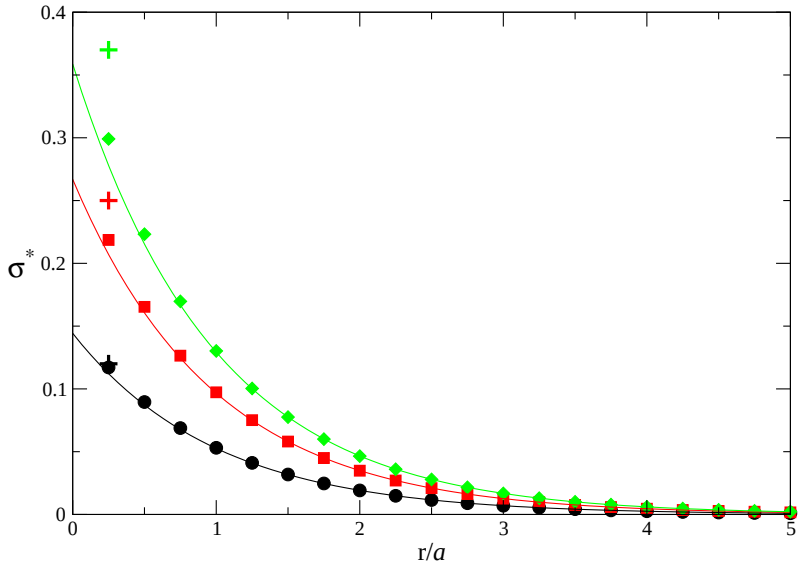

Figure 6.9: Same as Fig. 6.8 for surface charges $\sigma = 0.12$ *(spheres),* $\sigma = 0.25$ *(squares), and* $\sigma = 0.37$ *(diamonds).*

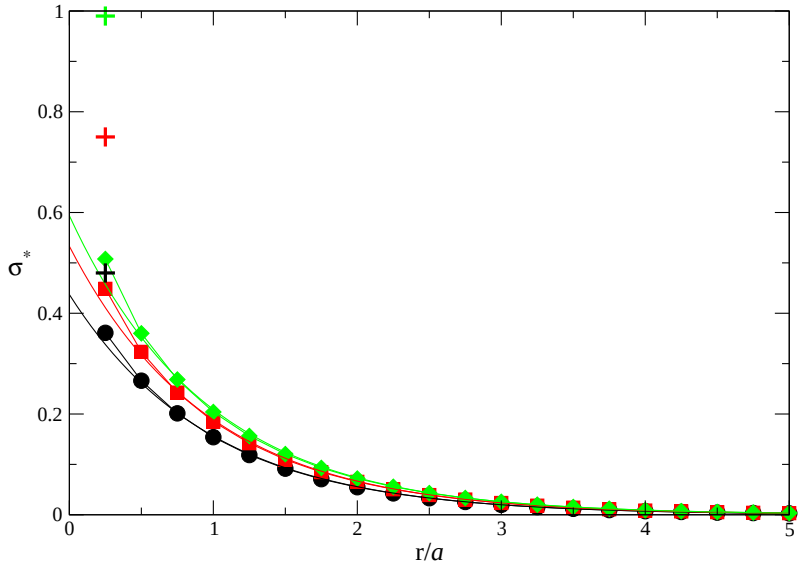

Figure 6.10: Same as Fig. 6.8 for high surface charge: $\sigma = 0.48$ *(spheres),* $\sigma = 0.75$ *(squares), and* $\sigma = 0.99$ *(diamonds).*

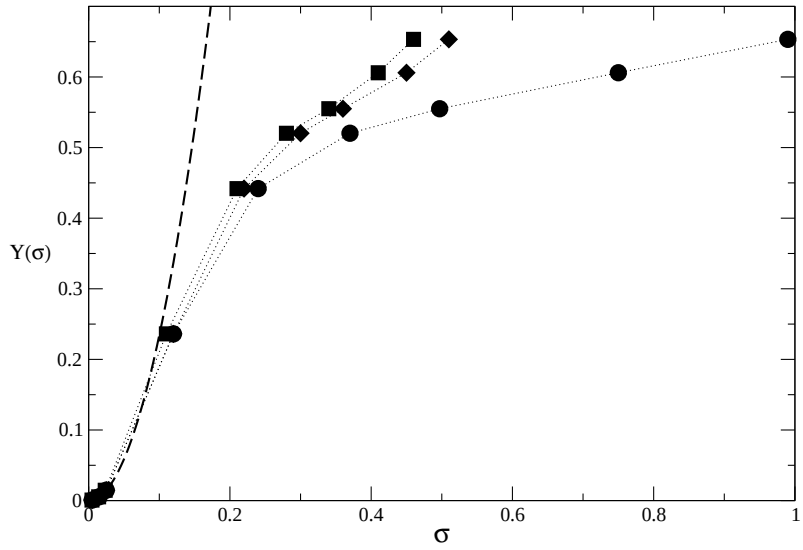

Figure 6.11: $\Upsilon(\sigma)$ *versus* σ *as predicted by Booth (dashed curve), and the computed* $\Upsilon(\sigma)$ *versus (1) the imposed surface charge (circles), and versus the surface potential computed by means of Eq. (6.12) where the* ζ *potential is (2) computed from the non-linear PB (diamonds) or (3) extrapolated by assuming a Yukawa-like form (squares). We observe that although the surface charge renormalization improves the agreement of the Booth theory with the computed sedimentation velocity, the disagreement is still substantial. The lines joining the simulation points are guide to the eye.*

relevant quantities, we can pinpoint the origin of this mismatch. While the electrostatic potential approximation is quite accurate, the approximated expression for the microion distributions, which is implicit in the use of the linear Poisson-Boltzmann equation, breaks down.

Although not self consistent, a better estimate for the sedimentation velocity could be obtained by making use of the approximate electrostatic potential of the Debye-Hückel theory, while using the full Poisson-Boltzmann distributions to compute the microion distributions. In more formal terms, instead of using

$$n_{\pm}^{\mathrm{LPB}}(r) = n_0 \left[1 - \mp U^{\mathrm{LPB}}(r)\right] \tag{6.14}$$

as an approximation for

$$n_{\pm}^{\mathrm{PB}}(r) = n_0 e^{\mp U^{\mathrm{PB}}(r)} \ , \tag{6.15}$$

We propose to use

$$n_{\pm}(r) = e^{\mp U^{\mathrm{LPB}}(r)}. \tag{6.16}$$

As we argued that the the co- and counterions cloud at the equilibrium determine the sedimentation velocity of the macroparticle, we define a phenomenological procedure to compute an effective charge compatible with this idea. From our computer simulations,

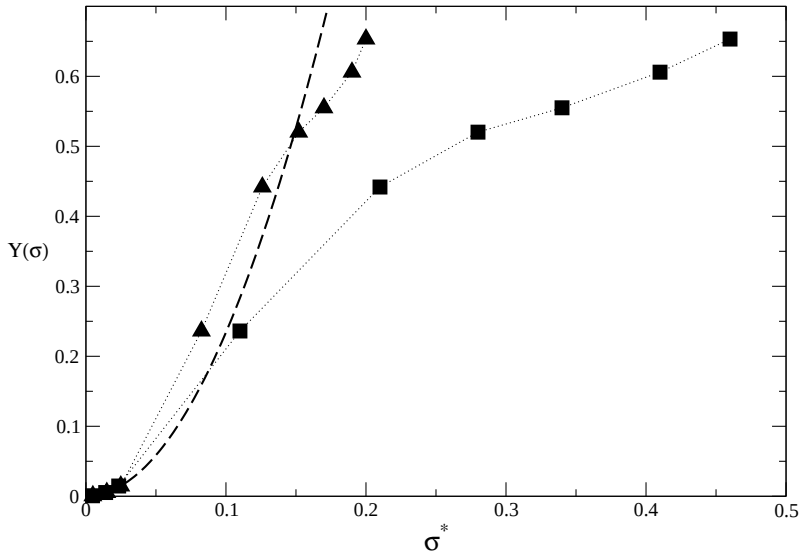

Figure 6.12: $\Upsilon(\sigma)$ *versus* σ *as predicted by Booth (dashed curve), and the computed* $\Upsilon(\sigma)$ *versus* σ *computed by means of the phenomenological procedure described in the text (triangles). It is also redrawn* $\Upsilon(\sigma)$ *corresponding to the type (3) in Fig. 6.11 (squares).*

we obtain the values for $n_{\pm}^{\mathrm{PB}}$ and of U^{PB}. Then we compute the linearized microion distributions by means of Eq. (6.6) ($n_{\pm}^{\mathrm{LPB}}(r) = n_0\,[1 \mp U(r)]$). We can now re-compute the electrostatic potential by substituting n^{LPB} with n^{PB}. In other words, we compute $\mp U^*(r) = ln[n_{\pm}^{\mathrm{LPB}}(r)/n_0]$. Note that $U^*(r)$ is just a convenient (yet arbitrary) way of defining an effective electrostatic potential. Finally, we define $\zeta \equiv U^*(0)$ and obtain a renormalized surface charge using Eq. (6.12). We show the result for the sedimentation velocity in Figure 6.12. Clearly this method, although it gives a better estimate of the sedimentation velocity has no solid foundation. A proper analysis would require the repetition of the original Booth (or Ohshima) treatment by using the substitutions which we are proposing.

7 Sedimentation velocity of charged disks

Abstract

In this chapter, I present simulation results for the sedimentation velocity of charged disks. We explicitly took into account the hydrodynamic and electrostatic interactions and the deviation from the equilibrium position of the double layer.

In order to analyze the effect of the shape of the disk, the results are compared with those for a sphere with equal surface and charge. The results show that the reduction in the sedimentation velocity for disk-like macro particles has a different dependence on κa than spheres. An analysis of the behavior of highly charged disks (beyond the scope of the linearized Poisson Boltzmann equation) shows that the charge dependence of the sedimentation velocity of disks is similar to that of spheres. Our results suggest that the disks become hydrodynamically more symmetric at high charge.

7.1 Introduction

In this chapter I present calculations on the electrokinetics of charged disks. Such systems are of both theoretical and experimental interest. Because disks are not spherically symmetric, they provide an ideal model system to study the effect of the shape on the coupling between electrostatic and hydrodynamic response of a macroscopic particle. In fact, several theoretical studies suggest that there may be non-trivial coupling effects due to shape asymmetries [68, 69].

From a practical viewpoint, there are several charged disk-like and rod-like molecules that are biologically relevant. The most important of these is DNA. In the literature (see, for example, [70]), the hydrodynamic properties of hard rods and hard disks are claimed to be relevant for unerstanding the electrophoretic mobility of, for example, DNA. However, Ref. [70] concerns with purely neutral particles, and hence does not take the coupling between hydrodynamics and electrostatics into account. Since DNA is highly charged under physiological conditions, a systematic study of the electrohydrodynamic properties of highly charged particles is relevant for a better understanding of the motion of charged polyelectrolytes.

Many natural and synthetic clays (e.g. laponite) constitute another class of real systems that can be modeled as charged disks.

With our simulation method, we were able to study the dynamics of charged particles with arbitrary shapes in electrolytes at the Poisson-Boltzmann level, thus ne-

glecting charge correlation effects. For many systems this is not a serious limitation, in particular if the electrolyte contains no polyvalent ions.

7.2 Electrokinetic model

We will analyze a simple geometry in which one disk-like colloidal particle of radius a and height h sediments due to the action of a uniform external field. The disk has an overall charge $Q = Ze$, where Z is its valency and e is the elementary unit of charge, a radius a and aspect ratio $p = 2a/h$. The disk is assumed to be suspended in a symmetric electrolyte. For the sake of simplicity, we assumed that both co- and counterions have the same mobility and valency. The fluid mixture is characterized locally by density of the solvent ρ_s and by the densities of the electrolyte microions $\rho_\pm$. The latter determine also the local fluid charge, $q(\mathbf{r}) = ze[\rho_+(\mathbf{r}) - \rho_-(\mathbf{r})]$. We will restrict ourselves to monovalent electrolytes, where $z = 1$.

The dynamics of the overall system is governed by the electrokinetic equations, which specify how fluid momentum is accelerated due to local charge accumulation, while local fluid velocity in turn affects the convection of electrolyte densities. We rewrite these equations from Section 3.3 as

$$\frac{\partial}{\partial t}\rho_k = -\nabla \cdot \mathbf{j}_k \quad k = +, - \tag{7.1}$$

$$\frac{\partial}{\partial t}(\rho \mathbf{v}) = \eta \nabla^2 (\rho \mathbf{v}) - \nabla p + \frac{k_B T}{e} q \nabla \Phi. \tag{7.2}$$

$$\mathbf{j}_k = -\rho_k \mathbf{v} + D_k \left[\nabla \rho_k + z_k \rho_k \nabla \Phi\right] \tag{7.3}$$

where D_k stands for the diffusivity of each electrolyte. In the case of symmetric electrolytes all D_k are the same. $\Phi \equiv \hat{\Phi}/(e\beta)$ stands for a dimensionless electrostatic potential. Φ satisfies the Poisson equation

$$\nabla^2 \Phi = -4\pi l_B \left[\sum_{k=\pm} z_k \rho_k + \rho_w\right], \tag{7.4}$$

where $l_B = \beta e^2/(4\pi\epsilon)$ is the Bjerrum length (with $\epsilon = \epsilon_0 \epsilon_r$ denoting the medium dielectric constant), while ρ_w refers to the charge density due to embedded solid objects, either colloids of solid walls.

Equation (7.1) is simply a conservation law and (7.3) is the constitutive equation. Together with the incompressibility condition $\nabla \cdot \mathbf{v} = 0$, Eq. (7.2) corresponds to the Navier-Stokes equations for an incompressible, isothermal electrolyte at vanishing Reynolds number. η is the shear viscosity. In the presence of a gravitational field, the corresponding force must be added to the right-hand side of Eq. (7.1).

7.2.1 Simulation method

As a simulation method, we employed the lattice-Boltzmann method described in Chapter 5.

We took the lattice spacing as the unit of length, and the time step as the unit of

time. We fixed the kinematic viscosity to $\nu = 1/6$ to render the simulation algorithm simpler [8]. The solvent density is taken as unity, $\rho_s = 1$, the (gravitational) body force was fixed to be 10^{-6} (in the usual lattice units), which is well inside the linear response regime and generates fluid velocities of the order of 10^{-8}. The electrolyte diffusivity is set to $D = 0.19$. Spurious diffusion due to advection is negligible (see Chapter 5). The values of the diffusivity and of the flow velocity result in Péclet numbers smaller than 10^{-1}. For these low Péclet numbers we do not expect to observe a large distortion of the electric diffuse layer. In the simulations described in subsequent sections we vary the salt density in the range between 7×10^{-4} and 5×10^{-3} as a way to control the diffuse layer width.

7.3 Sedimentation of neutral disks

Before assessing the role of electrostatics on the sedimentation of non-spherical particles, we need to analyze the sedimentation of hard disks within lattice Boltzmann since, contrary to the case of spheres, there are no analytic expressions for the sedimentation velocity of an isolated hard disk with finite aspect ratio. In order to validate our computer simulations, we then used analytical theories available for the sedimentation velocity of infinitesimally thin disks [71, 72].

We simulated disks with two different nominal aspect ratios $p = 10$ and $p = 5$, corresponding to disks of lateral dimension $h = 2$, and radii $a = 10$ and 5, respectively. However, because the solid particle is identified as the midpoint between the links joining fluid and solid nodes, the hydrodynamic shape of the object may differ slightly from the nominal one. We need, hence, to calibrate the shapes of the disks to avoid spurious lattice artifacts entering the subsequent numerical analysis. An unambiguous way to determine these effective sizes (the hydrodynamic radius and height), is to measure the friction coefficients of the particles and then use known formulae that relate the friction coefficients to the particles' sizes. In addition, a second complication arises in computer simulations. Since we use periodic boundary conditions, we measure in practice the friction coefficient of a regular array of particles at volume fraction $\varphi = \pi a^2 h / L^3$, where L is the simulation box lateral size. Hence, one needs to generate a series of simulations with increasing box size in order to extrapolate the infinitely diluted friction coefficients for a neutral disk. An analogous procedure will be needed to study the sedimentation velocity of a charged disk in the dilute limit.

7.3.1 Friction coefficients

To compute the sedimentation velocity of the disk, we placed it on the lattice and performed the simulations in the frame of reference centered on the disk. We then applied a body force to the fluid equal and opposite to the gravitational force acting onto the disk and measured the total fluid velocity at the steady state v_F. Because this velocity is equal and opposite to the sedimentation velocity of the particle $U_d = -v_F$, we can relate the sedimentation velocity to the friction coefficient via the formula $U_d = F_g/\xi$, where U_d is the sedimentation velocity of the disk, ξ is the friction coefficient, and F_g is the gravitational force. As the disk is not spherically symmetric, we studied

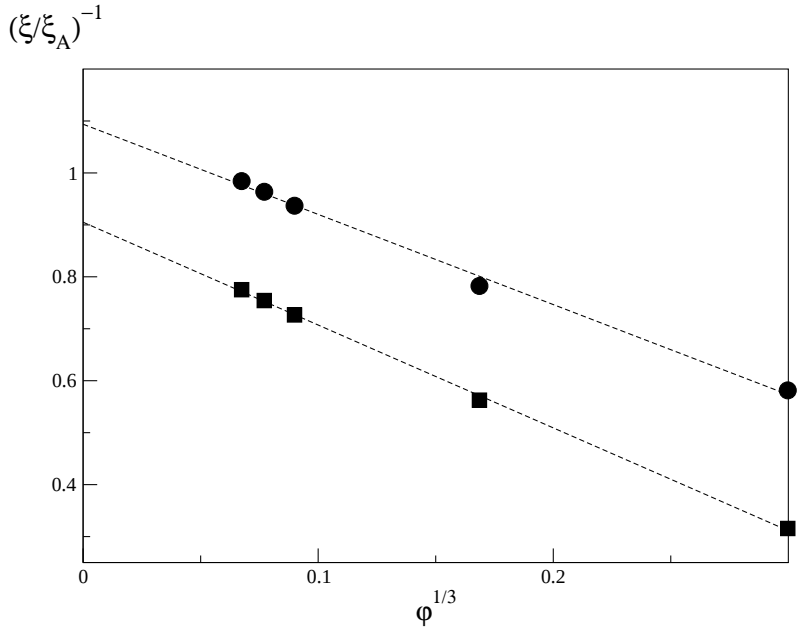

Figure 7.1: Edgeside (circles) and broadside (squares) friction coefficients for a sedimenting neutral disk of aspect ratio $p = 5$ as function of the array's volume fraction. The friction coefficients are normalized by the friction coefficient of a sphere with radius $R = a$ of the cylinder, i.e. $\xi_0 = 6\pi\eta R$. The dashed lines are linear fits.

the friction coefficients along the two principal axes, respectively the edgewise and broadside friction coefficients.

Hashimoto [56] has shown that the friction coefficient of an array of hard spheres scales as $(\xi/\xi_0)^{-1} = 1-1.76\varphi^{1/3}+\varphi+O(\varphi^2)$, indicating that, to lowest order in volume fraction, the decrease in velocity is controlled by the number density of the particle array. Hence, we expect the same functional dependence to hold for neutral disks. As can be seen from Fig. 7.1, the simulations do indeed suggest a $\varphi^{1/3}$ dependence of the friction coefficient. Then we used this functional dependence to extrapolate to infinite dilution. In Figure 7.1 we show the edgeside and broadside friction coefficients for the neutral disk with $p = 5$ at various volume fractions, normalized by the Stokes friction coefficient of a sphere with the same area, i.e. by $\xi_A \equiv 6\pi\eta R$, $R = \sqrt{a(a+h)/2}$. From this plot we derived the friction coefficients ξ_{edge} and ξ_{broad} for an isolated disk. It is known that the friction coefficient of an infinitely thin disk, which corresponds to the limit $p \to \infty$, becomes identical to that of an oblate spheroid with the same aspect ratio between its main axis [72]. There exists numerical evidence indicating that for a (finite) not too small value of p, the friction coefficient of a disk does not deviate much from that of an oblate ellipsoid at intermediate and large aspect ratios, and numerical simulations results have been published for the analogous problem of disk diffusion [70]. Hence, we can use those estimates to assess

$\xi_A = 6\pi\eta R$	p=5		p=10	
	Simulation	Oblate spheroid	Simulation	Oblate spheroid
ξ_{edge}/ξ_A	0.91	0.9	0.93	0.85
ξ_{broad}/ξ_A	1.1	1.06	1.19	1.11
ξ_{edge}/ξ_{broad}	0.83	0.84	0.78	0.77

Table 7.1: Friction coefficients of an isolated disk in edgeside and in broadside motion normalized by the Stokes friction coefficient $\xi_A = 6\pi\eta R$ of a sphere with equal surface area, i.e. with radius $R = \sqrt{a(a+h)/2}$ (a it the radius of the cylinder). We compare the computed value of the friction coefficients with approximate theoretical values for an oblate spheroid with the two axis equal to the disk radius and to the disk height. We studied two disks with aspect ratios $p = 5$ and $p = 10$, respectively.

the hydrodynamic shape of the neutral disks.

We summarize the results for the normalized friction coefficients for disks of two aspect ratios in Table 7.1. For the disk with $p = 5$, we conclude that, to a good approximation, the hydrodynamic radius and height correspond to the nominal ones. The numerical values obtained for the larger disk ($p = 10$) are less satisfactory than for the shorter one. This may seem surprising, since for a larger object the disagreement between the nominal and hydrodynamic size is expected to decrease. However, the ratio between the perpendicular and parallel frictions $\xi_{\text{edge}}/\xi_{\text{broad}}$ do agree with the value estimated on the basis of the nominal size, suggesting that the deviations come mostly from uncertainties related to finite volume fraction. Hence, we conclude that, also for this shape, the disagreement between the two sizes is negligible, and ascribe the deviations to interactions with the periodic images. Such interactions are larger for the more asymmetric disk (especially for broadside sedimentation), taking into account that for the two disks the simulations have been run at equal volume, rather than at comparable volume fractions.

7.4 Sedimentation velocities of charged disks: effect of charge

Before discussing the computed sedimentation velocities of charged disks, I briefly recall the sedimentation velocity theory for weakly charged spheres presented in Section 3.2.2. Booth [27](and Ohshima *et al.* [28]) predict that the sedimentation velocity of an isolated sphere $U_s(Z)$ is a quadratic function of the sphere charge which can be expressed as

$$\frac{U_s(Z)}{U_s(0)} = 1 - c_2(\kappa R)Z^2, \tag{7.5}$$

where $U_s(0)$ is the sedimentation velocity of a hard sphere in the dilute limit, and the pre-factor c_2, for a symmetric 1-1 electrolyte is, in the Debye-Hückel theory,

$$c_2(\kappa R) = \frac{k_B T l_B}{72\pi R^2 \eta D} f(\kappa R), \tag{7.6}$$

R is the radius of the sphere and $\kappa = \sqrt{4\pi l_B \sum_k z_k^2 \rho_k}$ is the inverse Debye length which characterizes the size of the electrical double layer. The function $f(\kappa R)$ is presented in Section 3.2.2.

We expect that the dependence on colloidal charge given by Eq. (7.5) will also hold in the Debye-Hückel limit for disks since they differ from the spheres only in the hydrodynamic properties, which in turn only enter in the factor $c_2(\kappa R)$. To test this hypothesis, we computed $1 - U_d(Z)/U_d(0)$ for disks. If the behavior of disks is similar to that of spheres, this function should be linear in Z^2. The inset of Fig. 7.2 shows $1 - U_d(Z)/U_d(0)$ as function of Z^2 for two disks with aspect ratios $p = 5$ and $p = 10$. We fixed the Debye screening length so that $\kappa a = 1$. Moreover, because the dilute-limit expansion procedure is computationally expensive, we performed the simulations at constant volume fraction, $\varphi = 7.2 \times 10^{-4}$ for the disk with $p = 5$, and $\varphi = 2.9 \times 10^{-3}$ for $p = 10$. Hence, we assume that Eq. (7.5) is generalized to finite volume fraction, with the sedimentation velocity normalized by the sedimentation velocity of hard disks at the corresponding volume fraction. The inset of the figure clearly displays the expected dependence on disk charge both for edge and broadside sedimentation.

7.4.1 High charge regime

In many cases of practical interest, colloidal particles are highly charged (for disks particles see [73]). In this regime the theoretical framework put forward by Booth breaks down. To analyze the behavior of the sedimentation in this regime, we performed simulations for the sedimentation of charged disks at constant volume fraction, where we varied the disk charge over a wider range. In Figure 7.2 we plot again $1 - U_d(Z)/U_d(0)$ as function of the surface charge $\sigma = eZ/\left[2\pi a(a+h)\right]$. One can identify the quadratic dependence discussed above, a crossover region from surface charge densities between 0.1 and 0.4, and, eventually, a more linear regime. This behavior is consistent with the numerical results on the sedimentation velocity of charged colloidal spheres (see Chapter 6) which also showed a deviation from Booth's predictions for surface charge densities around 0.1. The crossover takes place in the same range for both parallel and perpendicular sedimentation.

If one compares the deviation of the sedimentation velocity for edge- and broadside motion, as displayed in Fig. 7.2, we can see that the sedimentation velocity decreases faster for edgeside motion regardless of the aspect ratio, which indicates that the electrokinetic coupling is stronger for this orientation. In the same figure, we also show the decrease in sedimentation velocity for a sphere of radius $R = 4.2$, which shows the same dependence on surface charge as that of the disks. If one now compares the sedimentation velocity of disks for two aspect ratios, one observes that, at high charges, $1 - U_d(Z)/U_d(0)$ for both disks approach each other.

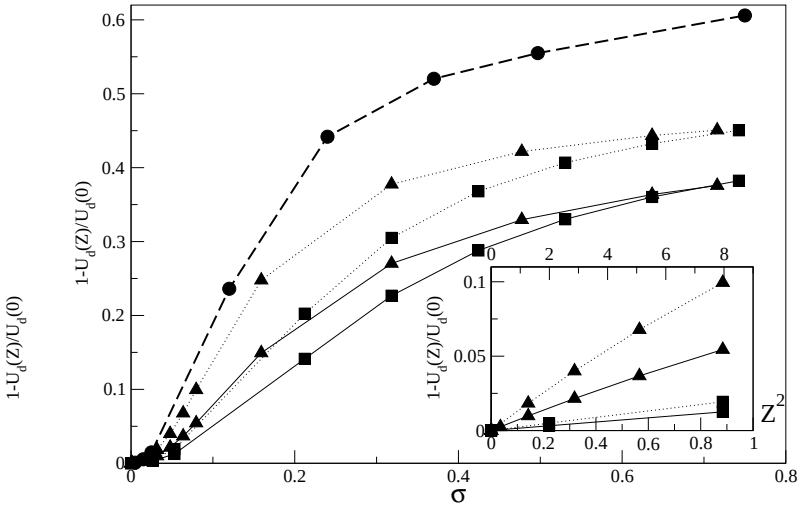

Figure 7.2: Surface charge dependence of $1 - U_d(Z)/U_d(0)$ *for a disk with aspect ratio* $p = 5$ *(squares) and* $p = 10$ *(triangles) in edgeside (dotted lines) and broadside (continuum lines) motion. For comparison, we also show the behavior for a sphere with radius* $R = 4.2$ *(circles). In the inset, we show the surface charge dependence for weakly charged disks; the lower scale refer to the disk with* $p = 5$*, while the upper one to the disk with* $p = 10$*. For disks the quadratic dependence upon the charge is confirmed. In the inset the lines are linear fits, while in the figure are a guide to the eye.*

7.5 Sedimentation velocities of charged disks: volume fraction dependence

We have already shown that for an ordered array of hard spheres the initial volume fraction dependence enters through the number density, and hence should scale as $\varphi^{1/3}$. In Chapter 5, we have verified that this functional dependence also holds for charged spheres, provided that the system is diluted enough such that there is no significant overlap of the double layers. For disks we expect the $\varphi^{1/3}$ dependence to hold under the same circumstances. In order to test whether there is a detectable effect of the overlap of electric double layers of different disks, we have computed the normalized friction coefficients for disks of aspect ratio $p = 5$ as a function of the volume fraction, for volume fractions up to 10%, for different widths of the diffuse layer.

In Figure 7.3 we show the results for a weakly charged disk, both for edgeside and broadside motion. Note that, in the dilute limit, the friction coefficients will depend on κa due to the electrohydrodynamic interaction. For edgeside motion the convergence to the dilute limit is slower, indicating a stronger coupling between disks; we attribute this to the fact that the distance of closest approach coincides with the external field direction. Although for $\kappa a = 1/2$ and high volume fractions the diffuse layers overlap, the effect of the diffuse layer is minimal with respect to the volume fraction dependence, as evidenced by the larger differences between edgeside and broadside

sedimentation. Hence, at small volume fractions the dependence is, in all cases, $\varphi^{1/3}$, and a subsequent decay at intermediate volume fractions is strongly influenced by excluded volume effects. Despite this general trend, there is a remaining dependence on κ superimposed and hence, the amplitudes in the volume fraction dependence of the friction coefficients will depend on the details of the electro-hydrodynamic coupling.

The dependence upon κ becomes more visible in Fig. 7.4, where we display the friction coefficients of highly charged disks. Although here the dependence on κ becomes more relevant, as the volume fraction increases its relevance diminishes, suggesting that at intermediate and large volume fractions the effect of the overlap of diffuse layers is less important than the interplay between electrolyte structure and hydrodynamic friction. On the other hand, at small enough volume fractions, the dependence is always consistent with $\varphi^{1/3}$, although deviations from such a behavior set in earlier.

This fact indicates that the dilute limit is harder to reach at higher charges. Moreover, since in the limit of an infinitesimally narrow double layer the sedimentation friction coefficient should coincide with that of a hard disk at infinite dilution, the smaller values observed for narrower double layers already at high dilution indicate that at small volume fractions there is a strong electrokinetic coupling. It is important to keep in mind that the values of κ are computed on the basis of the electrolyte densities in the bulk. This means that, if the counterions density added to the salt to ensure charge neutrality—i.e. $\rho_- = -Z/V_\mathrm{f}$, where Z is the valency of the sphere and V_f the volume occupied by the electrolyte—is much larger than the amount of salt, the system behaves as if the electrolyte were made of counterions only. Hence, κ^{-1} does not describe the typical screening length any longer. For our simulations this phenomenon only becomes important for the highest volume fractions (typically $\varphi > 0.08$). This means that our dilute-limit expansions (performed at much lower volume fractions) is not affected by this complication.

7.6 Sedimentation velocity of charged disks: effect of the diffuse layer

After having analyzed the role of charge and volume fraction, we want to address the effect of the relevance of the width of the double layer on the sedimentation velocity of disks. We will use the analysis of the previous section to extrapolate the infinite dilution limit $U_d(Z)$ from a series of sedimentation velocities $U_d(Z, \varphi)$; in this way, we can compare simultaneously the role of diffuse layer width and volume fraction. We scale the sedimentation velocities by the sedimentation velocities of isolated charged-neutral disks $U_d(0)$, values that we have obtained in Section 7.3.1. The ratio $U_d(Z)/U_d(0)$ measures the reduction is the sedimentation velocity of one charged disk due to its electrokinetic interaction with the electrolyte. The reduction in sedimentation velocity in the dilute limit is interesting theoretically (because we can compare with analytic results for weakly charged spheres). However, in experiments the reduced sedimentation velocity $U_d(Z, \varphi)/U_d(0, \varphi)$ at finite φ is the relevant one. For simplicity, in the remaining part of this section, we will be writing $U_d(Z)$ instead of $U_d(Z, \varphi)$ but, unless explicitly stated, the volume fraction dependence is always assumed.

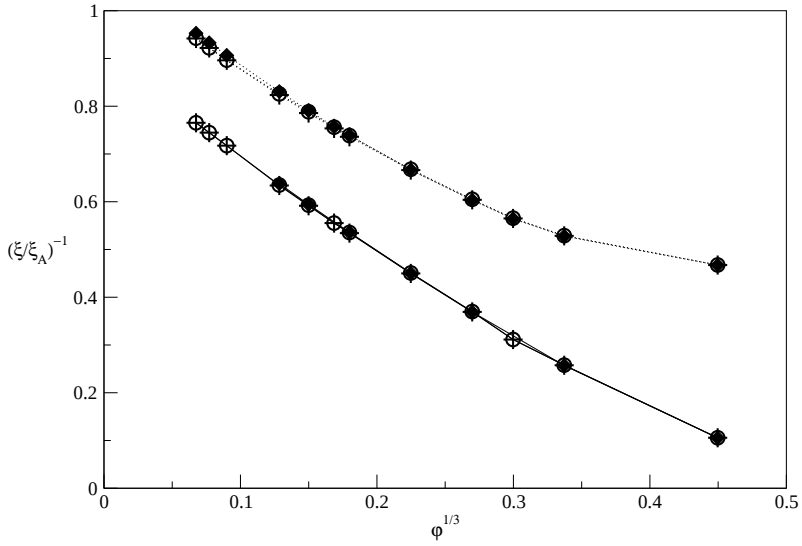

Figure 7.3: Volume-fraction-dependent normalized friction coefficients for a disk with radius $a = 5$, *aspect ratio* $p = 5$, *and valency* $Z = 10$ *for* κa *equal to* 0.5 *(spheres),* 0.8 *(pluses), and* 2.1 *(filled diamonds). The upper curves are for the edgeside friction coefficient, while the lower curves are for a broadside friction coefficient. The curves are normalized by the friction coefficient of a sphere with equal surface area* $\xi_A = 6\pi\eta\sqrt{a(a+h)/2}$ *(see Table 7.1 for the correspondent neutral values). Lines are drawn as a guide to the eye.*

In Figure 7.5(a), we show the normalized sedimentation velocity as a function of the double layer width for a disk with aspect ratio $p = 5$ in edgewise motion, for different volume fractions. For infinitely thin and infinitely broad diffuse layers, the sedimentation velocity should coincide with that of a charged-neutral disk, and hence the curve should approach one for both small and large κa, as indeed observed. The decrease at intermediate values of κa enters as a result of the interplay between hydrodynamic dissipation and electrolyte diffusion. The largest effect is observed when the size of the double layer is of the order of the largest dimension of the disk, i.e. $\kappa a \sim 1$. The effect increase with decreasing volume fraction, consistent with the discussion in the previous section. Already at volume fractions around 1%, the changes in normalized sedimentation are negligible. The minimum velocity also depends on volume fraction, an effect which is consistent with previous findings for spheres [74]. A similar behavior is observed in Fig. 7.5(b), where broadside sedimentation for a weakly charged disk is depicted. It is interesting to note that the decrease in sedimentation velocity is slightly smaller. We can ascribe this effect to the fact that the distorted double layer contributes a bit less to the hydrodynamic friction because the wider side of the disk is exposed to a region where the velocity gradients are smaller.

In Figures 7.6(a) and 7.6(b), we show the sedimentation velocity for a weakly charged disk with a higher aspect ratio $p = 10$. The trends are the same as for the smaller disk, although the minimum velocity seems to depend on aspect ratio, and is

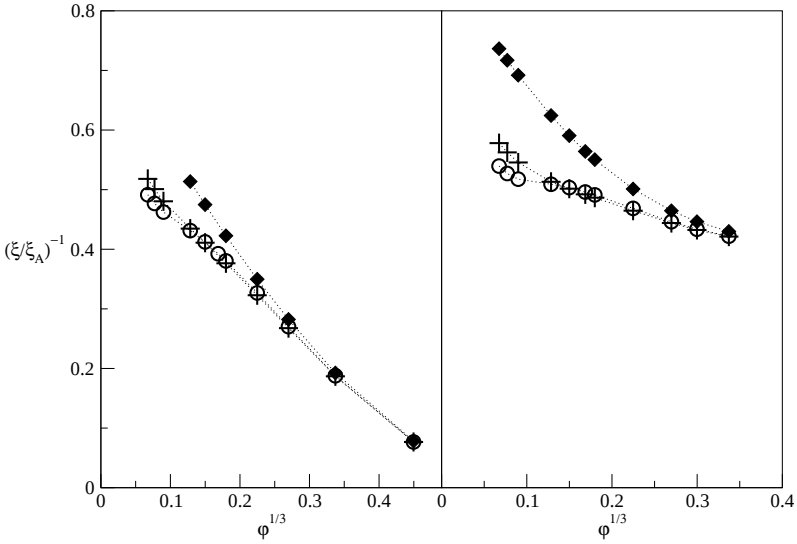

Figure 7.4: Volume-fraction-dependent normalized friction coefficients for a disk with radius $a = 5$ *and aspect ratio* $p = 5$ *and valency* $Z = 100$ *or* κa *equal to* 0.5 *(spheres),* 0.8 *(pluses), and* 2.1*(filled diamonds). a) Edgeside friction coefficient; b) Broadside friction coefficient. In all cases, curves normalized by the friction coefficient of a sphere with equal surface area* $\xi_A = 6\pi\eta\sqrt{a(a+h)/2}$ *(see Table 7.1 for the correspondent neutral values). Lines are drawn as a guide to the eye.*

achieved now for slightly narrower double layers. The reduction in absolute terms is now smaller, but this is simply due to the lower surface charge density as compared with the smaller disk. It is worth mentioning that, while for the disk with $p = 5$ we reached the limiting diluted value for $U_d(Z)/U_d(0)$, for the disk with $p = 10$ we had to perform the dilute-limit extrapolation. This different volume fraction dependence confirms that a large asymmetry among the various sizes of a macroscopic particle makes the dilute limit harder to obtain.

In Figure 7.7 we show the sedimentation velocity for a highly charged disk, normalized by the sedimentation velocity of uncharged disks at the same volume fraction. Although, again, the relevance of the electrokinetic coupling in the sedimentation velocity diminishes upon increasing volume fraction, the coupling between electric friction and velocity dissipation becomes much more dominant now. The sedimentation velocities decrease by almost 50% its value, and the range of $\kappa a'$swhere appreciable deviations from the behavior of the uncharged disk is observed is wider than in the case of weakly charged disks. As mentioned earlier, because for $\varphi >$ 0.08 the counterion density is much larger than the coion density, κ^{-1} no longer relates to the space decay of the charge-density distributions. In Figure 7.8 we also show the sedimentation velocity for an highly charged disk with $p = 10$ which confirms the same observation.

In all the previous figures, we have observed that the reduction in sedimentation velocity for edgewise motion is larger than for broadside motion, with differences up

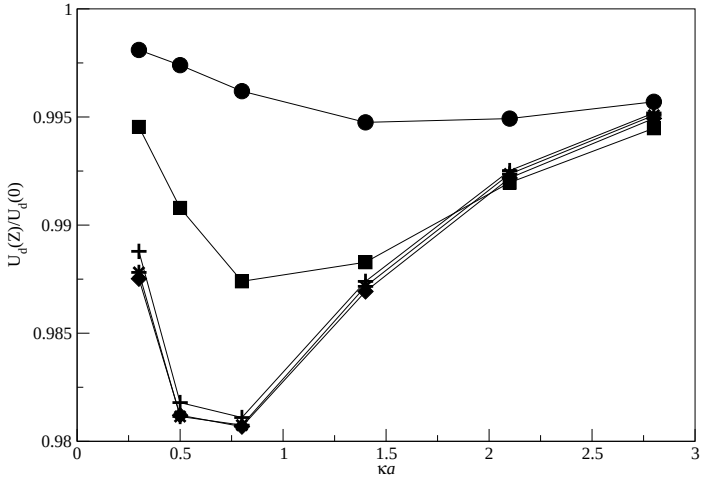

(a) Edgeside motion

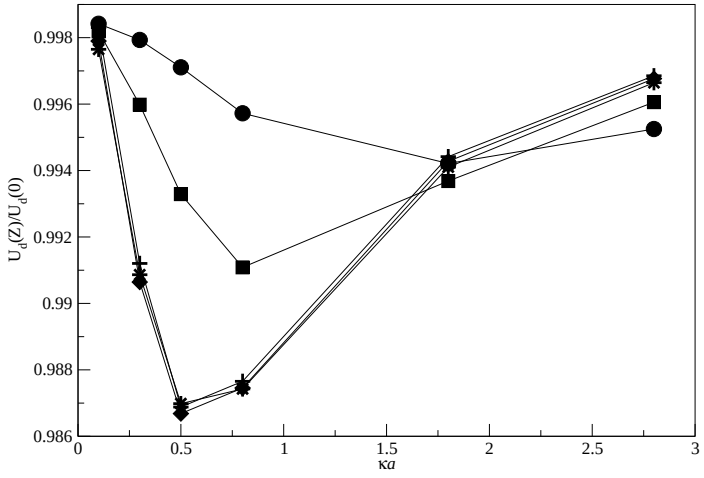

(b) Broadside motion

Figure 7.5: Normalized sedimentation velocity of a charged disk with aspect ratio $p = 5$, radius $a = 5$, and valency $Z = 10$. The different simulation points correspond to $\varphi = 3.8\times10^{-2}$ (circles), 4.8×10^{-3} (squares), 7.3×10^{-4} (pluses), 4.6×10^{-4} (stars), and 3.1×10^{-4} (diamonds). (a) Edgeside motion; (b) Broadside motion. Lines are drawn as a guide to the eye.

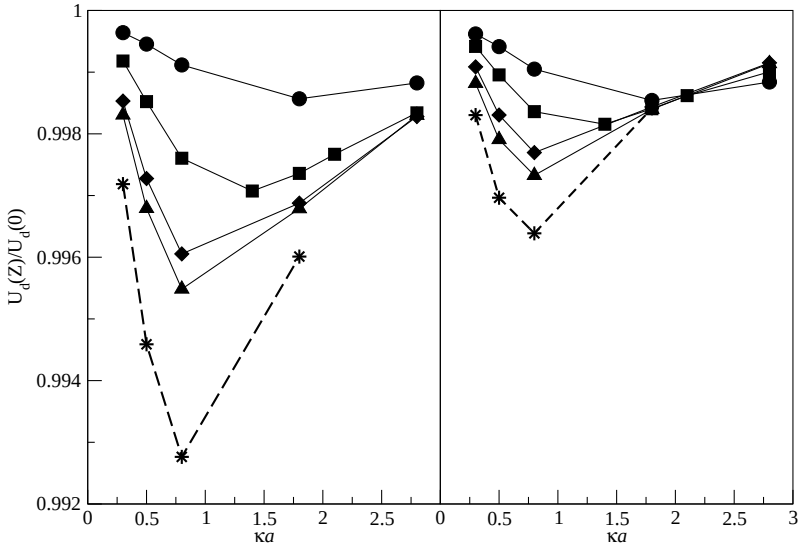

Figure 7.6: Normalized sedimentation velocity of a charged disk with aspect ratio $p = 10$, radius $a = 10$, and valency $Z = 10$. Different curves: $\varphi = 1.9 \times 10^{-2}$ (circles), $\varphi = 6.5 \times 10^{-3}$ (squares), $\varphi = 2.9 \times 10^{-3}$ (diamonds), and $\varphi = 1.8 \times 10^{-3}$ (triangles), and the correspondent dilute limit extrapolation (stars). Left: Edge side motion; right: Broad side motion. Lines are drawn as a guide to the eye.

to around 20% for wide double layers. This effect can be intuitively understood in terms of the different forces felt by the electric double layer in the two configurations. For edgeside sedimentations, most of the diffuse layer is exposed to the flow induced by the sedimenting array of disks. In confront, for broadside motion, most of the electric double layer is located in a region where the fluid velocity is small and is not subject to large gradients. One would then naively expect that this difference will be enhanced by an increase of the surface charge. However, the relative difference, in fact, decreases with disk charge. Hence, we there must be non-trivial couplings of the electrostatic restoring force to the flow field surrounding the disks. This is qualitatively illustrated in Figs. 7.9 and 7.10, where we show the velocity fields generated by a sedimenting disk for edge and broadside motion. It is clear that in the latter most of the diffuse layer is in a region of smoothly varying velocity, while the former it is exposed to larger velocity gradients. More interestingly, by comparing the flow fields past the weakly and the highly charged disk, we observe that the hydrodynamic shape of the particle become more isotropic. In order to fully understand this mechanism, more detailed simulations of the flow patterns are necessary; in fact, intuitively, one would expect that, due to charge accumulation near the particle (induced by the highly charged disk), the region where the fluid is affected by the charge of the disk becomes narrower.

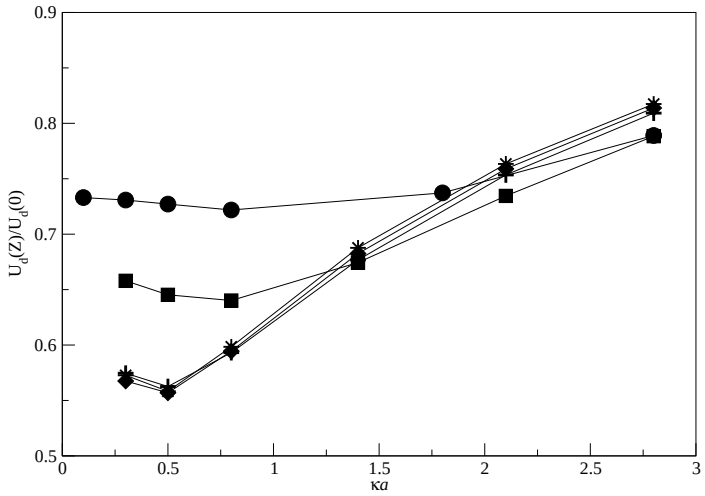

(a) Edgeside motion

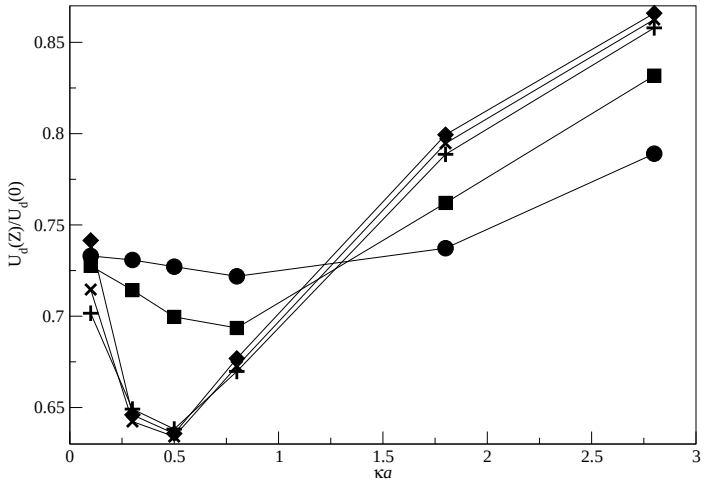

(b) Braodside motion

Figure 7.7: Normalized sedimentation velocity of a charged disk with aspect ratio $p = 5$, *radius* $a = 5$, *and valency* $Z = 100$. $\varphi = 3.8{\times}10^{-2}$ *(circles),* $4.8{\times}10^{-3}$ *(squares),* $7.3{\times}10^{-4}$ *(pluses),* 4.6×10^{-4} *(stars), and* 3.1×10^{-4} *(diamonds).(a) Edgeside sedimentation; (b) broadside sedimentation. Lines are drawn as a guide to the eye.*

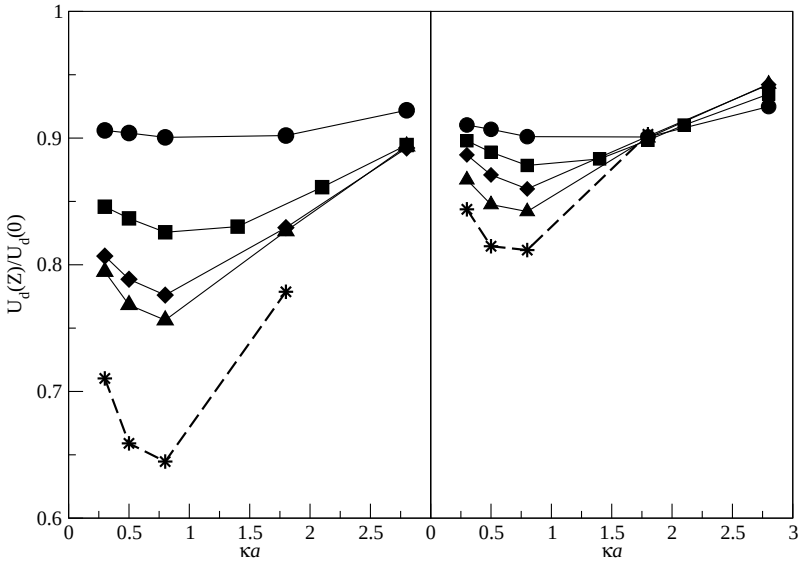

Figure 7.8: Volume-fraction-dependent reduction in the sedimentation velocity of a charged disk with aspect ratio $p = 10$, radius $a = 10$, and valency $Z = 100$. The plot on the left refers to a disk sedimenting along its edge side, while the right part along its broad side. The different curves correspond to volume fractions $\varphi = 1.9 \times 10^{-2}$ (circles), 6.5×10^{-3} (squares), 2.9×10^{-3} (diamonds), 1.8×10^{-3} (triangles), and the corresponding dilute limit extrapolation (dashed line with star symbols). Lines are drawn as a guide to the eye.

7.7 Sedimentation velocity of charged disks: shape effects.

When attempting to quantify the importance of the shape in disk sedimentation, we face the problem that one cannot change the shape of a disk without changing either the surface charge density or the overall particle charge. Then, because the electrostatic field next to a particle is proportional to the surface charge σ, a change in the surface area will change the electric field surrounding the particle, making impossible to isolate the effect of shape change. On the other hand, keeping σ constant by varying the overall particle charge is not a solution either since the reduction in sedimentation velocity does depend also on Z [see Eq. (7.5)]. As a result, we will have to modify both valency and volume (to keep the surface area constant) to disentangle charge effects from effects arising from shape changes. However, even if we take care of this problem, we can only compare each disk with the corresponding sphere, because the two disks we study have different areas.

In order to compare equals with equals, we computed the scaled sedimentation velocity $U_d(Z)/U_d(0)$, where $U_d(Z)$ is the sedimentation velocity of an isolated particle with valency Z, and $U_d(0)$ is the velocity of the same object in the absence of charge.

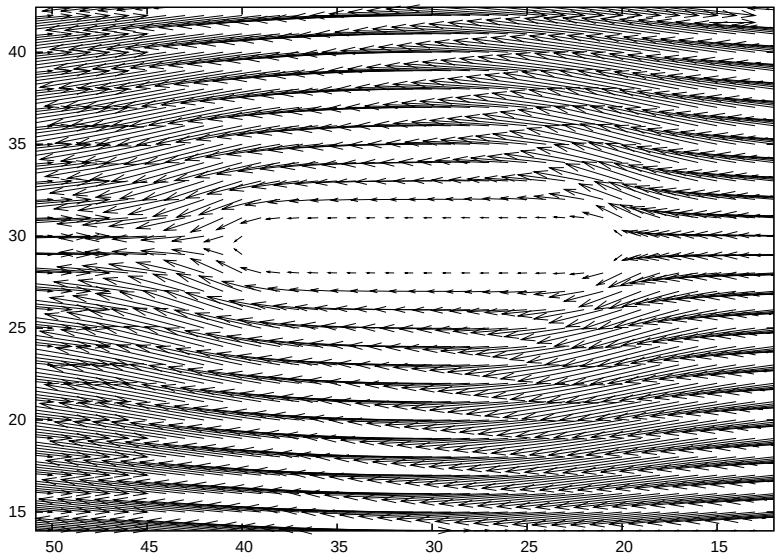

(a) Z=10

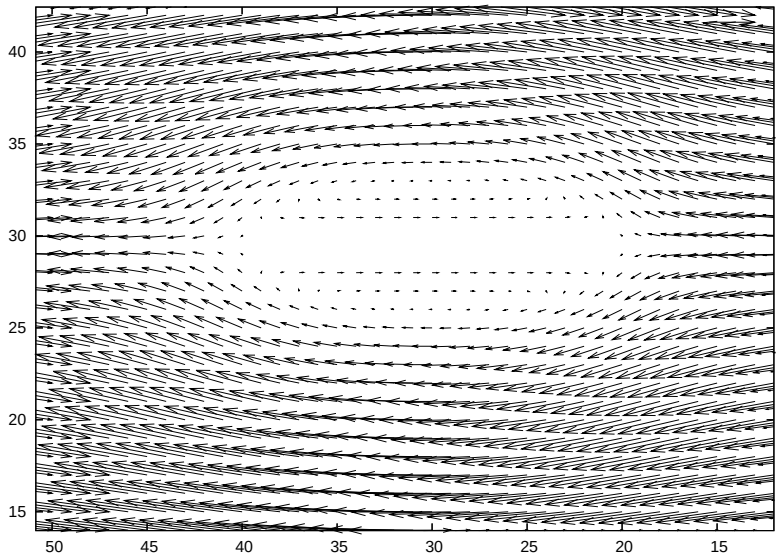

(b) Z=100

Figure 7.9: 3D flow fields near a charged disk sedimenting along its edge side *projected on the plane perpendicular to the disk passing through the center of the disk. The magnitude of the velocities has been conveniently scaled to render them visible.*

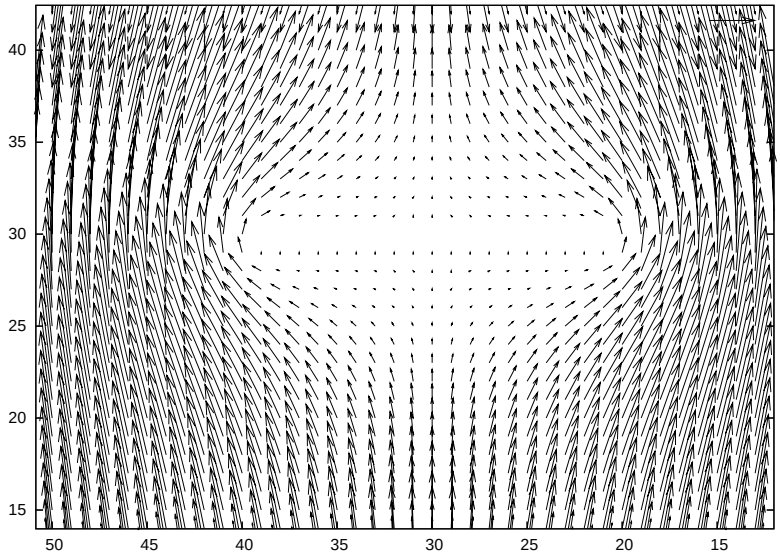

(a) Z=10

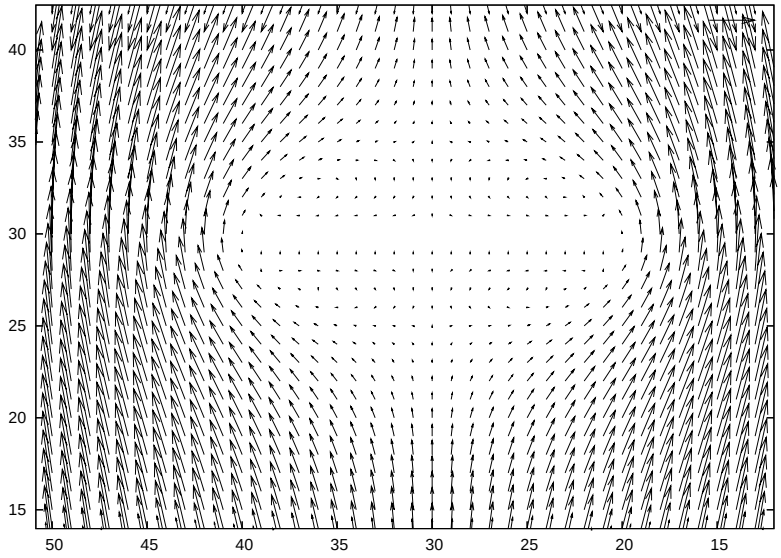

(b) Z=100

Figure 7.10: 3D flow fields near a charged disk sedimenting along its broad side *the projected on the plane perpendicular to the disk passing through the center of the disk. The magnitude of the velocities has been conveniently scaled to render them visible.*

We then compared $U_d(Z)/U_0(0)$ with the corresponding normalized sedimentation velocity of a sphere with valency Z and the same surface area $U_s(Z)/U_s(0)$. In this way we eliminate the effect of size on the settling velocity, disentangling shape from size effects.

For weakly charged particles, we can make use of Booth's prediction to analyze the results. To this end, rather than studying the scaled velocity directly, we have found fruitful to consider $[1 - U_d(Z)/U_d(0)]/Z^2$, which is the coefficient c_2 [see Eq. (7.6)] in the case of a sphere. It is a direct measure of the electrokinetic reaction induced by the electric double layer. Since we have argued in Section 7.4 that the charge dependence of disks is the same as the one observed for spheres in the Debye-Hückel limit, the previous ratio is a quantitative way of assessing the role of shape on the sedimentation velocity.

In Figs. 7.11(a) and 7.11(b), we show $[1-U_d(Z)/U_d(0)]/Z^2 \equiv c_2^d$ for disks with two aspect ratios and small charge, $Z = 10$ both for edge and broadside sedimentation. c_s^d is expressed in units of $A_2^s \equiv k_B T l_B / \left(72\pi D\eta a^2\right)$, in such a way that it simplifies to the universal function $f(\kappa a)$ predicted by Booth. For weakly charged disks and thin double layers, the decrease in velocity does not depend strongly on size. This is consistent with Smoluchowski's theory for electrophoresis 3.2.3, which predicts that the electrophoretic velocity of particles with the same zeta potential (the electrostatic potential at contact) is independent of the particle shape if $\kappa a \to \infty$. However, the deviation from the Smoluchowski limit appears at narrower double layers for broadside motion. Hence, shape affects significantly the sedimentation velocity of suspended particles. Moreover, in the case of asymmetric objects, the orientation of the particle also affects the velocity. For both broadside and edgeside sedimentation, the electrokinetic coupling of a disk is always smaller than the decrease for an equivalent sphere. One can clearly see that the decrease in velocity for broadside motion is smaller than for edge motion.

In the high charge regime we use the same quantity, c_2^d, to assess the role of shape, although we know that the Booth theory fails in this case. In Figures 7.12(a) and 7.12(b) we show c_2^d, again for two aspect ratios. In the thin diffuse layer limit, our data are consistent with Smoluchowski theory, and we observe again a departure from the results for a sphere upon increasing the width of the electric double layer. The maximum effect is observed for electric-double-layer widths of the order of the longest object length, and, again, the decrease for broadside motion is smaller than for edgewise motion. This is consistent with the description given above, that the disk become more isotropic.

By comparing Figs. 7.12(a) and 7.12(b), the reader might conclude that the reduction in sedimentation velocity is higher for the disk with a smaller aspect ratio. However, one should not overlook the fact that two disks have the same valency and therefore very different surface charges $\sigma_{p=5} \simeq 3.4 \times \sigma_{p=10}$. To show how much the surface charge affects c_2, we show c_2 for the disk with $p = 10$ also at $Z = 300$. Even though the surface charge of this disk is still lower than the surface charge for the other disk, the electrokinetic effect is already more pronounced.

In Fig. 7.13 we show the effective Stokes radius $[R_{\text{eff}} \equiv F/\left(6\pi\eta U\right)]$, where F is the magnitude of the external force acting on the disk. For small charges, the effective radius depends weakly on the double layer width, and is larger for the edgeside

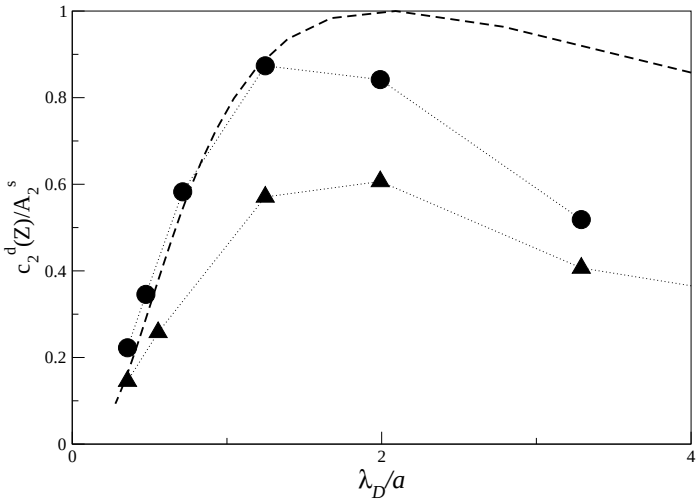

(a) p=5

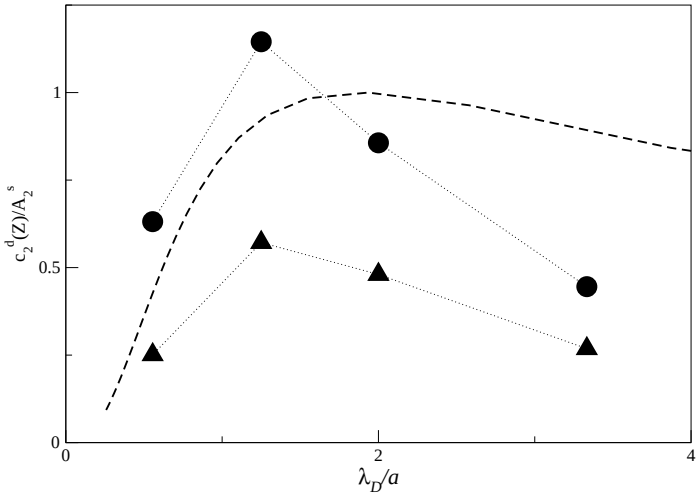

(b) p=10

Figure 7.11: Dilute limit of the normalized reduction in the sedimentation velocity of a disk in edgeside motion (spheres) and broadside motion (triangles) compared with the analytic theories valid for a sedimenting sphere of equal surface area (dashed curve) as function of the reduced electric double layer thickness. Disks and spheres have valency $Z = 10$. Subfigure (a) refers to a disk with aspect ratio p=5, and Subfigure (b) to p=10. Lines joining the simulation points are drawn as guide to the eye.

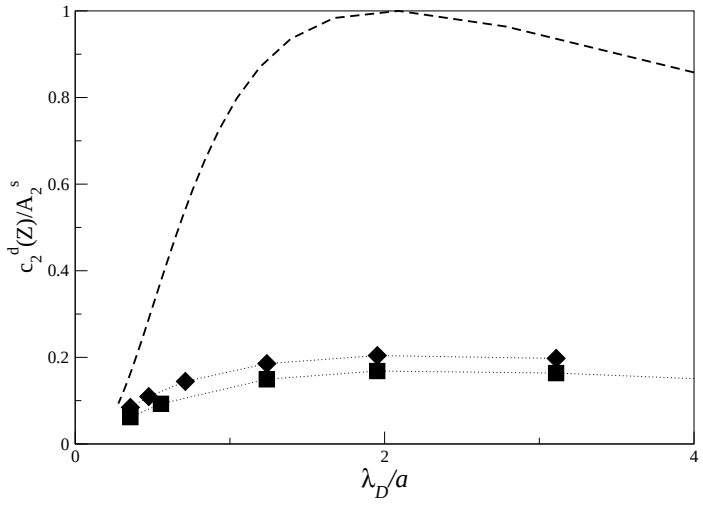

(a) p=5

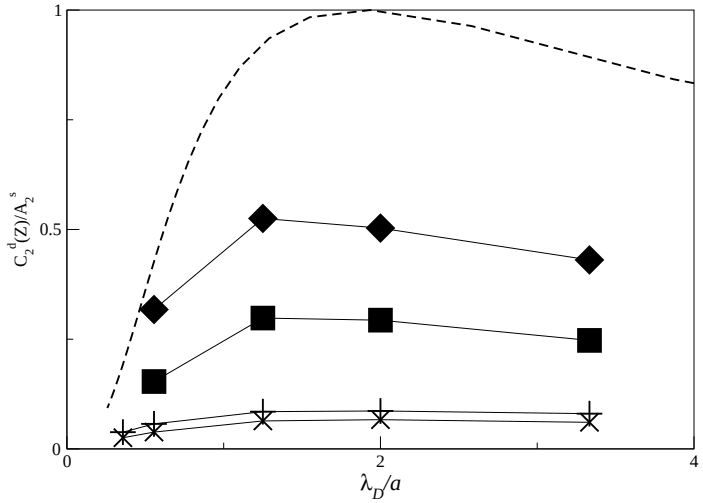

(b) p=10

Figure 7.12: Dilute limit of the normalized reduction in the sedimentation velocity of a charged disk in edgeside motion (diamonds) and broadside motion (squares) compared with the analytic theories valid for a weakly *charged sedimenting sphere of equal surface area (dashed curve) as function of the reduced electric double layer thickness. Subfigure (a) refers to a disk with aspect ratio p=5, and Subfigure (b) to p=10. Disks have and spheres have valency $Z = 100$, which correspond to a surface charge $\sigma = 0.45$ for the disk with $p = 5$ and to $\sigma = 0.13$ for the disk with $p = 10$. In Subfigure (b) we also show the same simulation for a disk surface charge $\sigma = 0.40$ for the disk with $p = 10$ in edgeside (+) and broadside (x) sedimentation. Lines joining the simulation points are drawn as a guide to the eye.*

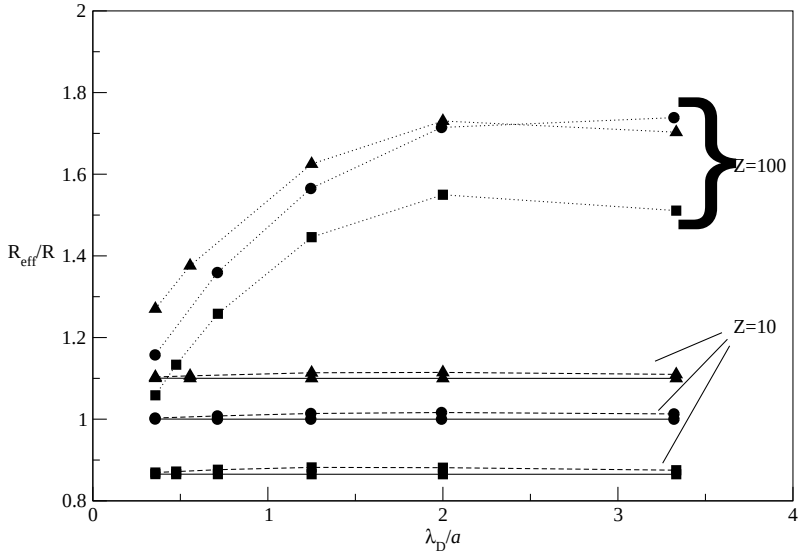

Figure 7.13: Effective hydrodynamic radius of a disk divided by the radius R of a sphere with equivalent surface as a function of the inverse Debye length in units of the disk radius. Disk with $p = 5$ in edgeside (square) and broadside (triangle) motion; sphere with same surface (circle). Uncharged objects (drawn line), $Z = 10$ (dashed curve) and $Z = 100$ (dotted line). The lines are drawn as a guide to the eye.

motion, as can be expected. At high charges the behavior is qualitatively different. The effective radius depends on the width of the double layer for $\lambda_D/a < 2$. For larger λ_D/a it tends to level off. As the diffuse layer broadens, the effective size that characterizes the sphere and the disk in broadside motion tend to converge, leading to a same effective shape for wide layers.

The physical origin of this effect is already implicit in Figs. 7.9 and 7.10. These figures show the velocity fields around the disk for both orientations. Different flow fields develop around the sedimenting disk for low and high surface charge.The flow profiles look more isotropic for high Z, therefore one might expect that for high Z, the friction coefficients of a disk approach that of a sphere with the same Z .

Discussion

In this chapter I analyzed lattice-Boltzmann simulations of the sedimentation of an array of charged disks. We treated the electrolyte at the Poisson–Boltzmann level, while we incorporated the relevant hydrodynamic coupling between the solvent and the dissolved electrolyte. Using the lattice-Boltzmann method, our approach allows us to model highly charged particles, and arbitrary κa values, which enlarges the regime of parameters that can be analyzed.

To our knowledge, no exact analytical expressions exist for the sedimentation ve-

locity of isolated neutral disks and finite thickness; hence, we validated the numerical accuracy of our approach with approximate expressions (exact for infinitesimally thin disks).

We studied the role of shape, volume fraction, charge, and ionic strength on the sedimentation velocity. We find that in the linearized Debye-Hückel regime, the sedimentation velocity has the same functional dependence on volume fraction and surface charge as that for spheres. At fixed κa, we studied the surface charge dependence of the disk sedimentation velocity, from which we observed that in the high-charge regime, the accumulation of charge near the disk surface layer decreases the effect of electrokinetic coupling on the sedimentation velocity, and also shows that such accumulation becomes more relevant as the disk becomes more anisotropic .

We have shown that the geometrical anisotropies of neutral disks are reduced by the presence of the electric double layer, especially for highly charged disks. In fact, we have seen that when the double layer is exposed to larger velocities, the reduction in sedimentation velocity is larger. Hence, this mechanism tends to generate a more symmetric disk response.

8 Electrophoretic mobility of charged-neutral model proteins

Abstract

At the isoelectric point the electrophoretic mobility of a molecule vanishes. This is usually seen as an indicator that the molecule is then uncharged. But, as is well known, neutral molecules may move under the influence of an electric field. The reason is that their electric multipole moments are usually nonzero.

In this case, the interaction of the electric diffuse layer with an external electric field can give rise to a non-zero electrophoretic mobility even for neutral macro-particles. There is experimental evidence that this is indeed the case and theories exist that account for the phenomenon in certain limits. However, the complexity of the equation governing electrophoretic mobility rules out analytical solutions for the general case.

We have computed the electrophoretic mobility of spherical colloids with zero electric monopole but non-zero higher-order electric multipole moments in an electrolyte. Hydrodynamic interactions are explicitly taken into account. First, we discuss the dependence of the electrophoretic mobility upon the Debye screening length and on the magnitude of the electric quadrupole. Next, we present calculations of the electrophoretic mobility of a neutral sphere with vanishing quadrupole electric moments.

8.1 Introduction

Electrophoresis is among the more important tools utilized to separate proteins, DNA, polyelectrolytes, and in general macroscopic charged particles [75, 76]. The basic physical mechanism that makes it work is simple. If we place a charged particle in an electric field, it will move because of the direct electrostatic interaction. In an electrophoretic device, proteins will stop at their isoelectric points (the pH concentration where the charge of the proteins is zero), and one can discriminates proteins with a different isoelectric point. However, one faces the problem that many proteins have the same isoelectric point and separating them becomes difficult. There are attempts to circumvent this problem adding polyelectrolytes to the proteins, thus changing their bare charge [77]. On the other hand, because it is known that the proteins have non uniform charge distributions and irregular shapes, it is believed that unpredicted response to electric fields could arise due to a subtle interplay of the hydrodynamic interaction and the electric double layer (EDL) of the proteins. Unfortunately, because the governing equations are complex, exact analytical formulae are in general

unavailable. Classic theories, in fact, describe only uniformly charged spheres, where (after the pioneering works of Hückel and Smoluchowski) Henry formulas can be used ([24] and references therein). Moreover, it is difficult to find papers regarding the electrokinetic properties of non-uniformly charged spheres or of non spherical particles; especially when these non uniformities are of comparable size of the Debye screening length. A notable exception is provided by the work of Anderson [78], who studied the electrophoretic response of a charged sphere due to its quadrupole moment, and, in the context of microfluidics, one finds works were the effect of shape on the electrohydrodynamic properties of particles is studied [69, 68].

In order to treat these intriguing and experimentally relevant interactions, which are especially important for colloids of asymmetric shapes and asymmetric charge distributions, we developed the lattice-Boltzmann method that I presented in Chapter 5. Using that technique, in this chapter, I can regard a study of the electrophoretic response of a sphere with non uniform charge distributions.

8.2 Model system

The system we study is composed of a neutral sphere with charged patches immersed in an electrolyte made of two ionic species and a neutral species. Because of the patches, the surface charge of the sphere, and the electrostatic potential at contact (usually referred to as the ζ potential), are not constant and vary with position. Therefore, the microions in solutions feel a local electrostatic potential that will attract or repel them. Important length scales in the system are the radius of the sphere and the thickness of the EDL (the Debye screening length), determined by the ionic strength of the electrolyte.

For the case of non-uniformly charged particles there is another relevant length scale, which determines whether or not the system will react to an external electric field. This length scale is the average size of the patches. When the screening length is much larger than the average patch width, we expect little electrophoretic response, because most microions feel the field due to many patches, and these fields tend to cancel. If, instead, the screening length is smaller than the average patch size, the diffuse layer will be able to follow the charge variation on the particle and can react to an external electric field.

8.2.1 Electric multipole moments

In this work, we study simple charge configurations with specific low order electric multipole moments. We took a sphere of radius R and cut it by a number of parallel planes perpendicular to the sphere radius. In a Cartesian coordinate system with origin in the center of the sphere, the equations of these planes are $x = x_{\mathrm{i}}$, with $-\mathrm{R} < x_{\mathrm{i}} < \mathrm{R}$ and $i = 1, ..., \mathrm{N}$, where N is the number of planes. With this procedure, we identified $\mathrm{N}+1$ sphere's slices and we attributed to each of them a uniform charge density $\rho(\mathbf{r}) = \mathrm{e}\rho_j$, with $\mathbf{r} \in j^{th}$ slice, where e is the elementary charge and ρ_j is a number density.

In terms of the charge density $\rho(\mathbf{r})$,

$$\mathrm{q} = \int \rho(\mathbf{r}) d\mathbf{r} \tag{8.1}$$

is the electric monopole moment,

$$\mathbf{p} = \int \mathbf{r}\rho(\mathbf{r}) d\mathbf{r} \tag{8.2}$$

is the dipole moment,

$$Q_{ij} = \int \left(3\mathrm{r}_i\mathrm{r}_j - \mathrm{r}^2\delta_{ij}\right) \rho(\mathbf{r}) d\mathbf{r} \tag{8.3}$$

is the quadrupole moment in components and, as the charge distribution is cylindrically symmetrical

$$\int r^n \rho(r) \mathrm{P}_n(\cos\theta) \mathrm{d}^3 r \tag{8.4}$$

is the generic multipole of order n, where $P_n(\cos\theta)$ is the Legendre polynomial of order n (see, for example, [79, 80]). From its definition [Eq. (8.3)], it follows that the electric quadrupole moment is symmetric ($Q_{ij} = Q_{ji}$), and traceless ($\sum_i Q_{ii} = 0$).

Fixing the electric monopole corresponds to one constraint to the charge distributions ρ_j. Fixing the dipole, and fixing the quadrupole adds two more constraints. When we fix these electrical moments of the sphere, we must ensure to have enough degrees of freedom (in our model the degrees of freedom are the x_i's and the ρ_j's) to satisfy the constraints. We always imposed charge neutrality, i.e. $q = 0$.

8.3 Electrophoretic mobility of a sphere with an electric dipole.

We begin by computing the electrophoretic mobility of a neutral sphere consisting of two oppositely charged hemispheres with charge $\mathrm{q} = \pm \mathrm{e}Z$. Because of the symmetry of this charge distribution, the monopole and the quadrupole moments are both zero. By construction, the sphere has non zero odd multipole moments.

For symmetry reasons, the electrophoretic mobility of such a sphere should vanish. As a test to our method, we verify that this is true for any value of the Debye length. In Figure 8.2 the filled circles represent the electrophoretic mobility of this sphere and observe that it, indeed, does have a zero electrophoretic mobility.

8.4 Electrophoretic mobility of a quadrupole

Anderson [78] has shown that for a sphere with $\kappa a \gg 1$ the electrophoretic mobility depends only the monopole and quadrupole moments of the zeta potential

$$\mathbf{U} = \frac{\epsilon}{\eta}\left[\langle\zeta\rangle\,\mathbf{I} - \frac{1}{2}\mathbf{P}\right] \cdot \mathbf{E}_\infty, \tag{8.5}$$

but not upon higher order moments.

In our simulation, we studied the electrophoretic mobility parallel to the symmetry axis of the patched sphere. In other words, we apply an electric field $\mathbf{E}_\infty = \hat{i}\mathrm{E}_\infty$ and the x component of the electrophoretic mobility will be $\mu_x = \mathrm{v}_x/\mathrm{E}_\infty$. Equation (8.5) it then reads

$$\mu_x = \frac{\epsilon}{\eta}\left(\zeta - \frac{1}{2}\mathrm{P}_{xx}\right). \tag{8.6}$$

In Ref. [78] the moments are computed as integral over the surface of the sphere. Because we work at low surface charged spheres, we can use the linearized Poisson-Boltzmann equation such that the relation between zeta potential and surface charge becomes linear ($\zeta = \sigma\lambda_D/\epsilon$). Hence we can rephrase the result of Anderson in terms of the charge multipole moments. To verify this dependence and to compute the electrophoretic mobility for an arbitrary EDL thickness, we performed a series of simulations where the quadrupole moment was non zero. We used three types of charge distributions.

The first one [see Fig. 8.1(a)] is analogous to the one described in the previous section, but the sphere is now divided into two non equal parts by a plane with equation $x = \xi$, where $0 < \xi < R$. Because of this asymmetry, the sphere has a non zero quadrupole moment Q_{xx}. We varied Q_{xx} by varying ξ. The total charge of the two parts is $q_1 = -eZ$, and $q_2 = -eZ$, however, because the volumes of the two parts is different, the charge densities of the two sides is different, in other words: $\rho(\mathbf{r}) = eZ/V_1$ for $x < \xi$, while $\rho(\mathbf{r}) = eZ/V_2$ for $x > \xi$, where $\mathbf{r}$ is inside the sphere, and V_1 and V_2 are the volumes of the two parts. For the second charge distribution [see Fig. 8.1(b)] we have used two parallel planes of equations $x = -\xi$ and $x = \xi$, with $0 < \xi < R$. We assigned a positive charge to the two symmetric external slices and a negative charge for the internal slice, i.e we set $\rho(r) = eZ/2V_1$ for $x < -\xi$ or $x > \xi$, and $\rho(r) = -eZ/V_2$ for $-\xi < x < \xi$. Again V_1 denotes the volumes of the external slices and V_2 is the volume of the internal slice. With the third and last configuration [see Fig. 8.1(c)] we broke also the cylindrical symmetry by cutting the sphere in two parts with one other plane perpendicular to the planes $x = \pm\xi$. We assigned a positive charge to the region defined by $x < -\xi$, $y > 0$ and $x > \xi$, $y < 0$, and a negative charge to the rest of the sphere. Again we assigned the charges uniformly in the two regions such to ensure charge neutrality.

In Figure 8.2, we show the electrophoretic mobility as determined in our computer simulation as function of the dimensionless parameter κa. For all these three charge distributions we varied ξ. We observe that in the limit $\kappa a \to 0$, the electrophoretic mobility tends to zero. This result is consistent with the Hückel [29] result for a uniformly charged sphere. In this limit, the EDL is so diffuse that it does not affect the motion of the particle; the electrophoretic mobility is, in fact, completely due to the direct Coulomb interaction between the charged particle and the external electric field. Hence, for $\kappa a \to 0$, the electrophoretic mobility of the patched sphere is essentially that of a neutral sphere and it vanishes.

In the opposite limit, i.e. when $\kappa a \to \infty$, we expect Eq. (8.6) to hold. In Figure 8.2, the curves seems to tend toward a plateau value. Because of the discrete nature of the lattice-Boltzmann model, we cannot study the limit $\kappa a \to \infty$ directly as we should expect discretization errors when κ^{-1} (in lattice units) < 1. Only by going to

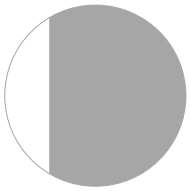

(a) Charge configuration 1

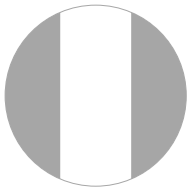

(b) Charge configuration 2

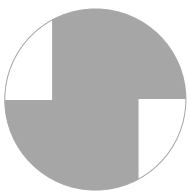

(c) Charge configuration 3

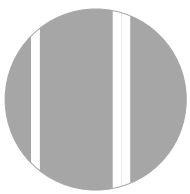

(d) Charge configuration with quadrupole zero

Figure 8.1: Cartoon representation of the charge configurations. The configurations corresponding to the cartoons (a), (b), and (c) have a vanishing charge but non-zero electric quadrupole moment, while the charge configuration corresponding to (d) have also a vanishing quadrupole moment (see text for a detailed description of the charge configurations).

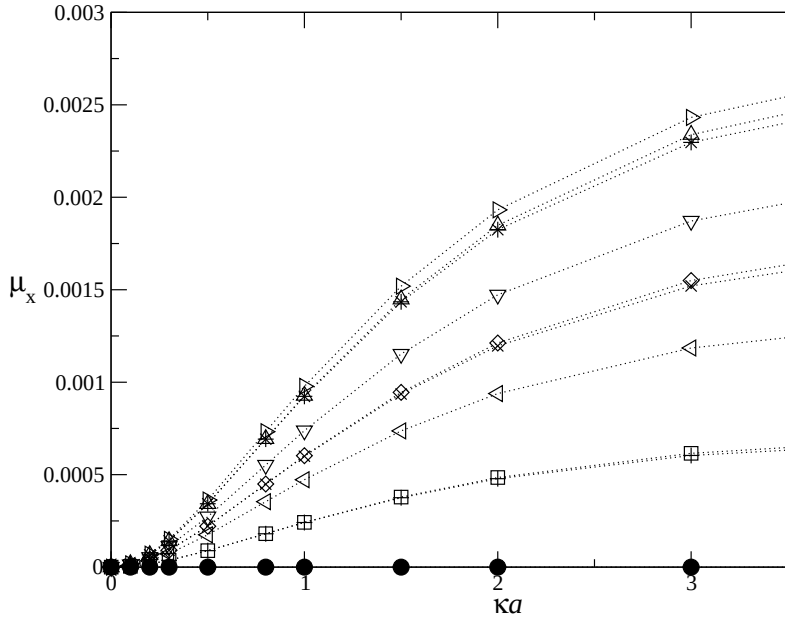

Figure 8.2: Electrophoretic mobility of a patched, neutral sphere. The filled circles, represent the electrophoretic mobility of a sphere with non-zero dipole moment, but all the even electric moments null; as expected $\mu_x = 0$ for all values of κa. The other curves correspond to the three charge distributions defined in the text for various values of Q_{xx}. We plot the curves for Charge Configuration 1 with Q_{xx} 5.96 (squares), 14.6 (diamonds), and 23.2 (triangles up; for Charge Configuration 2 with Q_{xx} 11.7 (triangles left), 18.0 (triangles down), and 24.6(triangles rigth); Charge Configuration 3 with Q_{xx} 5.96 (plus), 14.7 (exes), and 23.2 (stars). Dotted curves are a guide to the eye.

higher resolutions (larger sphere radii) we can study larger κa values. But this rapidly becomes prohibitively expensive. There is another reason to expect a discrepancy with the theoretical values of Eq. (8.6): the periodic boundary condition of a computer simulation. Because of the boundary condition, the actual system we simulates is a periodic cubic array of spheres at the volume fraction $\varphi = \mathrm{V}_{sph}/\mathrm{L}^3$, where V_{sph} is the volume of the sphere and L the simulation box size. One should do a size analysis by increasing the box size L until the sphere electrophoretic velocity reaches an asymptotic value. This procedure could in principle be performed but it also requires large computer resources because the velocity of an array of spheres decays as slow as $\varphi^{1/3}$ to the velocity of a single sphere. A detailed analysis of the volume fraction dependence of the electrostatic mobility is outside the scope of this chapter.

In Figure 8.3 we show that the electrophoretic mobility depends linearly on the quadrupole for all values of κa studied, consistent with Eq. (8.6). The slopes of the curves converge to an asymptotic value for increasinf values of κa, as predicted by Eq. (8.6).

If the linear dependence is valid, we can collapse all the curves onto a master curve by dividing them by the electric quadrupole moment Q_{xx} of the sphere. We show in Fig. 8.4 the outcome for this procedure. The curves mostly superimpose but there are still discrepancies left. If the only electric moments responsible for the electrophoretic mobility were to be the monopole and the quadrupole, the curves should exactly superimpose, especially for high values of κa. In the remainder of this chapter, we argue that these differences are due to the effect of higher order electric moment.

8.5 Electrophoretic mobility of a colloid with zero quadrupole

In this section, we show that in our simulations, even a neutral sphere with zero electric quadrupole moment has a finite electrophoretic mobility. If Eq. (8.5) were valid, such a charge distribution should not generate any electrophoretic mobility. Hence, the observed mobility is either due to the fact that we work at finite κa or it is due to discretization errors.

To create the charge distribution, we began by attributing a uniform charge density $\mathrm{q}(r) = -eZ_1$ to all the lattice nodes belonging to the sphere. Then, we placed on all the nodes inside the sphere with $x = -x_1$ or $x = x_2$ a positive charge $q(r) = eZ_2$. Z_1 and Z_2 are fixed by the constraint of charge neutrality. Upon varying the values of $x_1$and x_2 we can generate several charge distributions with various electric quadrupole moments. To create a charge distribution with zero electric quadrupole moment, we linearly added two of these charge distributions. Specifically, for a sphere of radius $a = 4.2$, we made the first charge distribution by fixing $x_1 = -3$, $x_2 = 2$ and number charge $Z_1 = Z$. The second distribution satisfied $x_1^{'} = -3$, $x_2^{'} = 1$, and charge density $Z_1^{'} = 0.3 \times Z$ (Z_2 is constrained by the condition of charge neutrality of each of the configurations separately). The hexadecapole electric moment H is then proportional to Z. In Figure 8.1(d) we show a cartoon of the charge configuration obtained with such a procedure.

In Fig. 8.5 we show the electrophoretic mobility of such a sphere with a hexade-

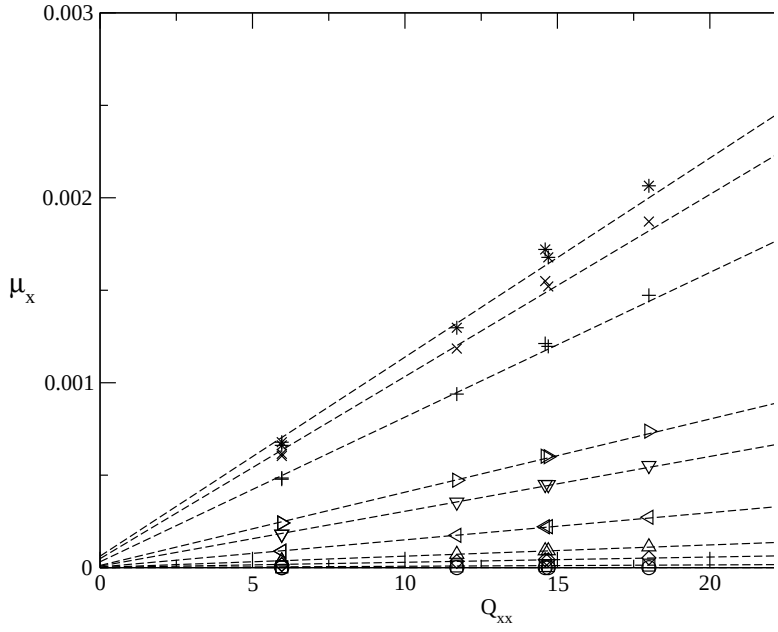

Figure 8.3: Linear dependence of the electrophoretic mobility on the electric quadrupole moment. The symbols correspond to the simulation results showed in Fig. 8.2 for κa equals to 0.001 *(circles),* 0.1 *(squares),* 0.2 *(diamonds),* 0.3 *(triandgels up),* 0.5 *(triangles left),* 0.8 *(triangles down),* 1 *(triangles right),* 2 *(plus),* 3 *(x's),* 4 *(stars). The dashed lines are linear fits.*

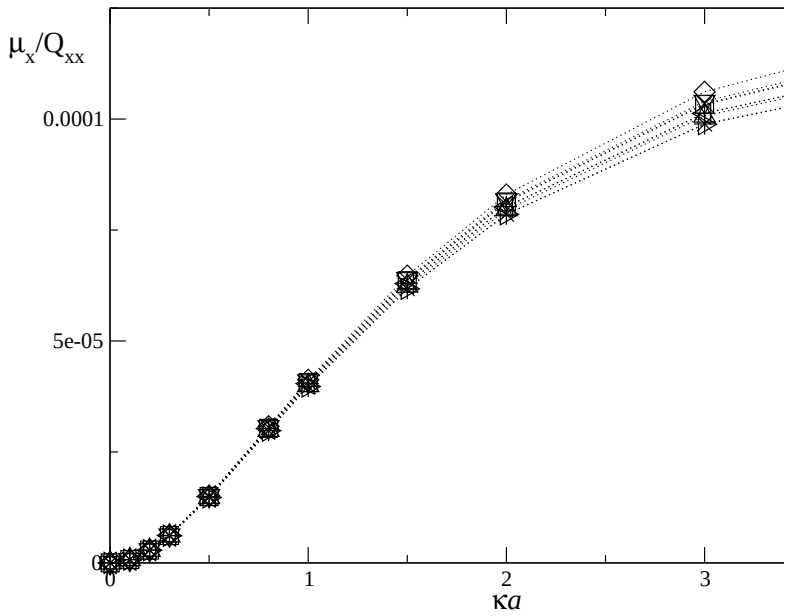

Figure 8.4: Electrophoretic mobility normalized by the electric quadrupole moment corresponding to the charge distributions of Fig. 8.2. The curves mostly superimpose with only a small discrepancy left at the higher values of κa. Dotted curves are a guide to the eye.

capolar charge distribution. The figure shows that even a sphere with vanishingly quadrupole moment appears to have a non-zero electrophoretic mobility. The figure suggests that the electrophoretic mobility levels off at higher values of κa than for quadrupoles.

This slow saturation may be due to the fact that the size of the charged patches in our hexadecapolar particles are quite small [$O(1)$ lattice spacings]. We expect asymptotic behavior only if $\kappa a \gg 1$ and $\kappa\delta \gg 1$, where δ is the smallest dimension of the patch.

We are now faced with a problem. In the limit $\kappa a \to \infty$, the Anderson calculations predict a vanishing electrophoretic mobility. If we assume this to be the case, we are faced with the question why our data do not seem to approach this limit. One possible answer is that at much larger κa values than we can probe, the electrophoretic mobility goes down again. Another possibility is that, precisely at large κa values, our result are sensitive to the lattice discretization. We stress that Anderson's result applies to a sphere. To reproduce it we would have to consider the limit $\delta/c \gg 1$, $\kappa a \gg 1$ where δ/c is the patch size in lattice units.

In order to obtain an indication on this limit, we performed one more simulation doubling the sphere radius while leaving the box sized unchanged to save computer time. The new computer simulation will then suffer a large volume fraction dependence (for neutral sphere, the decay to the dilute limit is of order $\varphi^{1/3}$). Because the discretization of the sphere is now slightly different, we have to change the charge distributions as well. In this larger sphere, the stripes contains two lattice nodes, thus we have $x_1 = -6,\ -5$, $x_2 = 3,\ 4$, and $Z_1 = Z$, while $x_1^{'} = -6,\ -5$, $x_2^{'} = 1,\ 2$, and $Z_1^{'} = 0.4256 \times Z$.

In Figure 8.6 we compare the electrophoretic mobility of the two spheres. We observe that the electrophoretic mobility is smaller in the case of a better lattice resolution. Thus it seems that the electrophoretic mobility decreases with increasing sphere resolution. This observation suggests that the electrophoretic mobility, which we measure for a neutral sphere with vanishing quadrupole electric moment, is due to the approximate representation of a sphere on a lattice.

To show the effect of the sphere with hexadecapolar charge distribution on the electrolyte, in Figures 8.7 and 8.8 we show the flow pattern surrounding this sphere in an electric field for two width of the electric double layer. In Figure 8.7, the Debye screening length is $\lambda_D \simeq 10$ lattice units ($\kappa a \simeq 1$), for which the charge distribution densities will not follow the abrupt variation of the surface charge. Hence, upon applying an electric field, only a small flow is generated.

In Figure 8.8, instead $\lambda_D \simeq 1$ ($\kappa a \simeq 8$) such that the microion charge distribution density will follow the surface charge variation up to around one lattice spacings. Hence, upon applying an electric field, oppositely charged microions will feel an electrostatic force oppositely directed. The end result is the formation of vortices near the sphere. In the limit of an infinitesimally thin double layer, because the Anderson's theory predicts a vanishing electrophoretic mobility, all these vortices must cancel out.

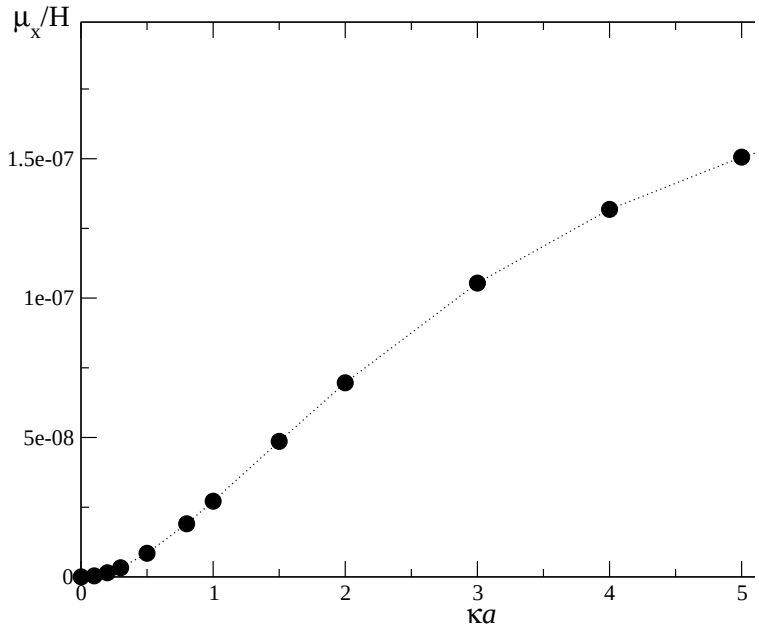

Figure 8.5: Electrophoretic mobility of a charged neutral sphere with zero electric quadrupole moment. The electrophoretic mobility is entirely due to the electric even multipoles of order higher than the quadrupole. The dotted curve is a guide to the eye.

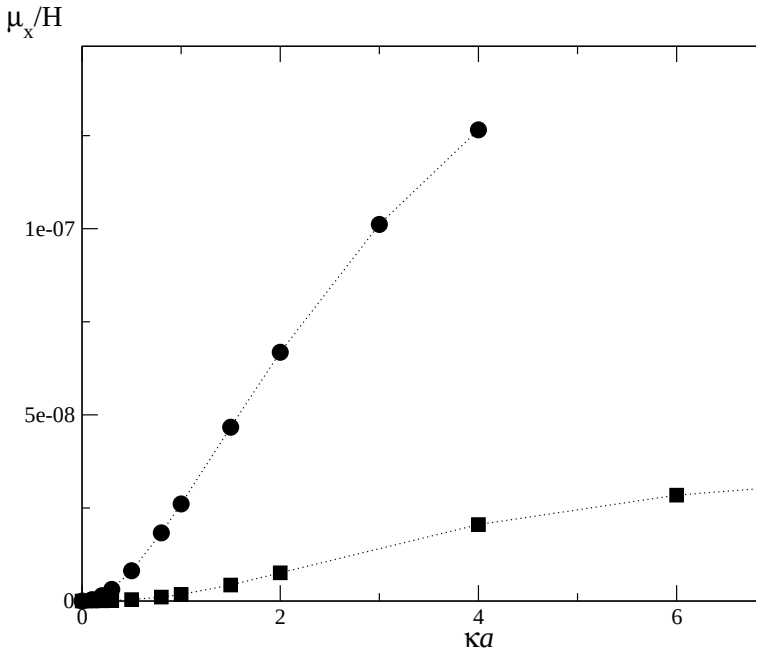

Figure 8.6: Effect of the increase in the lattice resolution on the electrophoretic mobility of a charged neutral sphere with zero electric quadrupole moment. We compare a sphere of radius $a = 4.2$ l.u. (circles) with a sphere of radius $a = 8.4$ l.u. (squares). The electrophoretic mobility levels off while increasing the lattice resolution. With the second sphere, at for an equal value of the Debye screening length we obtain a dimensionless κa twice as large. Dotted curves are a guide to the eye.

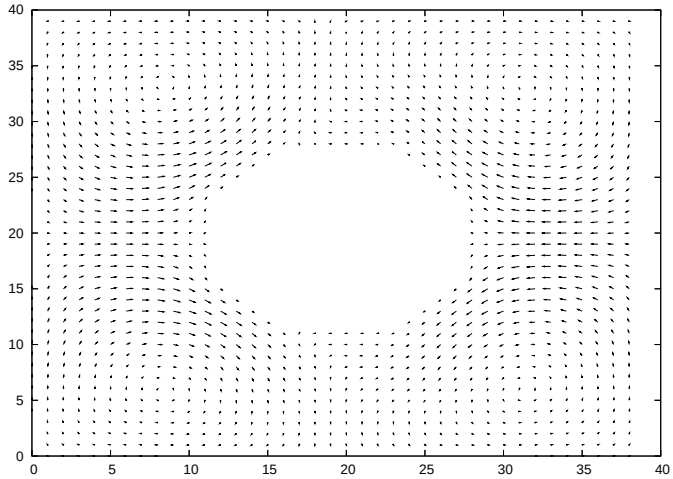

Figure 8.7: Flow profile surrounding a neutral sphere with a non vanishing hexadecapole electric moment and vanishing lower order electric moment. The sphere has radius $a = 8.4$ and $\kappa a = 0.8$. The width of the double layer is too large to follow the charge distribution on the sphere and we observe an almost symmetric flow pattern. The vortices are due to the hydrodynamic interaction of the sphere with its periodic images. The magnitude of the flow velocity is in arbitrary units.

Conclusions

In this chapter, I showed how the electrophoretic mobility (EM) of a neutral sphere, at finite volume fraction, depends on the electric multiple moments and on the Debye screening length. First, I presented the EM of a neutral sphere with different electric quadrupole moments. I then showed that at every value of κa the EM depends linearly on the electric quadrupole moment. I then showed the results for the EM of a neutral sphere with a vanishing quadrupole moment. We observed a non vanishing EM at intermediate values of κa. Because this results seemed in contrast with Anderson's analytical result, we increased the size of the particle for studying the dependence of the EM of spheres with hexadecapolar charge distribution on the particle size and for being able to reach a higher values of κa. The result for the larger sphere indicates that the measured EM mobility may depend on the non perfect lattice representation of spheres. Nonetheless, we showwed that the Anderson result is strictly valid only for perfect spheres, which are rarely present in biology. Hence, in order to fully understand electrophoresis experiments on biologically relevant particles, one need to analyze in detail the coupling of non-uniform surface charges with the hydrodynamic interaction of non spherical particles. However, for time reasons, we did not have the opportunity to tackle these interesting and relevant systems.

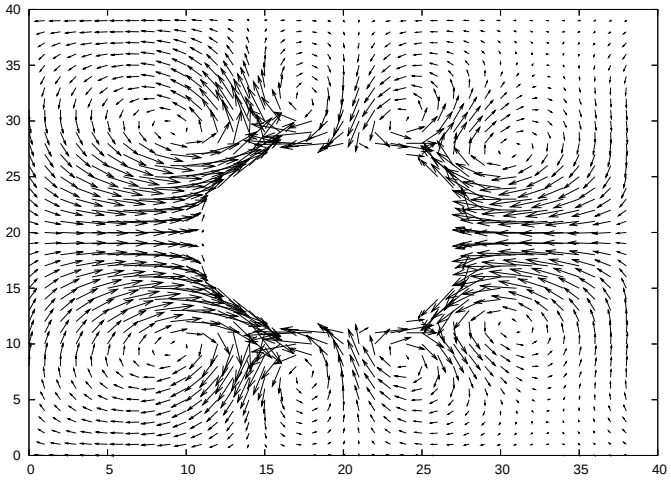

Figure 8.8: Flow profile surrounding a neutral sphere with vanishing electric quadrupole moment but a non vanishing hexadecapole electric moment. The sphere has radius $a = 8.4$ and the electric double layer with is given by $\kappa a = 8$. The width of the double layer is thin and it follow the charge distribution on the sphere. We observe the formation of vortices in correspondence with the charge distribution variation. The flow pattern develop a non trivial pattern. The magnitude of the flow velocity is in arbitrary units (the multiplying factor is the same as in Fig. 8.7).

A Problems with a multi-component lattice-Boltzmann description of an electrolyte

Abstract

This chapter describes some technical problems that arise when constructing a lattice-Boltzmann method to solve the electrokinetic equations. We start with an analysis of Ref. [50] that derived the lattice-Boltzmann equations by means of a Chapman-Enskog multi-scale analysis. As shown in Ref. [50] the Smoluchowski and the Navier-Stokes equations come out naturally as a long time limit of the microscopic rule. However, in this chapter I point out how a modification of the algorithm is necessary in order to achieve a truly tunable diffusivity. Secondly, I show how the algorithm fails to achieve a perfect balance at boundary nodes giving rise to small spurious currents. Although these spurious currents are shared by all the lattice Boltzmann implementations of multi-phase flows they have, to my knowledge, not yet received proper treatment. Although corrections of the spurious flows is possible, the implementations of such corrections remains impractical.

A.1 Lattice Boltzmann method for solving the electrokinetic equations

There are several ways to derive lattice-Boltzmann schemes. In Chapter 5, we considered a "bottom up" scheme—i.e. a scheme where one imposes all the required conservation laws locally, at the microscopic level of the single nodes. However, other schemes that are closely linked to the macroscopic equations, are often used (see for example [81, 51, 52, 54, 82]). In particular, Ref. [50] describe a "top-down" approach—i.e. an approach where the microscopic rules are defined taking care to recover the proper macroscopic behavior on the large length scale and long time scale—approach to lattice-Boltzmann simulation of the electrokinetic equations. Below, I briefly discuss this approach.

The model system under study is the one presented in Chapter 3. Let us briefly review it. The electrolyte is made of two oppositely charged (micro) ionic species ρ_+ and ρ_-, and a neutral solvent neutral species ρ_s. The governing equations are the electrokinetic equations (see Section 3.3)

$$\frac{\partial}{\partial t}\rho_\alpha = -\nabla\cdot\mathbf{j}_\alpha \quad \alpha = +,- \tag{A.1}$$

$$\frac{\partial}{\partial t}\left(\rho\mathbf{v}\right) = \eta\nabla^2\left(\rho\mathbf{v}\right) - \nabla p - k_B T\sum_\alpha z_\alpha\rho_\alpha\nabla\Phi. \tag{A.2}$$

$$\mathbf{j}_\alpha = -\rho_\alpha \mathbf{v} + D_\alpha \left[\nabla \rho_\alpha + z_\alpha \rho_\alpha \nabla \Phi\right] \tag{A.3}$$

where D_α and z_α stand for the diffusivity and valency of each ionic species, respectively. The total density ρ is defined by $\rho = \sum_\alpha \rho_\alpha$,while the total fluid velocity $\mathbf{v}$ is given by $\mathbf{v} = (\sum \rho_\alpha \mathbf{j}_\alpha)/\sum_\alpha \rho_\alpha$. $\Phi \equiv \hat{\Phi}/(e\beta)$ is the dimensionless electrostatic potential, which satisfies the Poisson equation

$$\nabla^2 \Phi = -4\pi l_B \left[\sum_{\alpha=\pm} z_\alpha \rho_\alpha + \rho_w\right], \tag{A.4}$$

where l_B is the Bjerrum length, ϵ the medium dielectric constant, and ρ_w the charge density due to solid objects suspended in the electrolyte. For a more detailed description of the model we refer the reader to Chapter 3.

In Reference [50] all three species are represented in a lattice-Boltzmann model (LB). To this end, one must define three single-particle distribution densities n_i^α, $\alpha = +, -, s$ and their evolution equations. The computer memory required for such a simulation (which, for big systems, constitutes one of the bottlenecks of a LB) is hence three times the one required by a standard one-phase LB. On the other hand, there would an advantage: the macroscopic transport coefficients of the microions (for instance their diffusivity) will naturally emerge as a continuum limit of the microscopic evolution rules by means of a Chapman–Enskog procedure.

The post-collision distributions $n_i^{\alpha\star} = n_i^\alpha + \Delta(n)$ are not the one of the standard lattice-Boltzmann method [cf. Eq. (2.42)] but are:

$$n_i^{\alpha\star}(\mathbf{r}, t^\star) \quad = \quad a_0^i \rho_\alpha(\mathbf{r}, t)\left(1 + \frac{1}{c_{\mathrm{S}}^2 \rho'(\mathbf{r}, t)} \mathbf{j}(\mathbf{r}, t) \cdot \mathbf{c}_i\right). \tag{A.5}$$

The factor a_0^i is the usual weighting factor which, for the D3Q18 lattice is equal to 1/12 for the $\mathbf{c}_i$ of speed 1 and equal to 1/24 for the velocity with speed $\sqrt{2}$. The propagation step is simply

$$n_i^\alpha(\mathbf{r} + \mathbf{c}_i, t+1) \quad = \quad n_i^{\alpha\star}(\mathbf{r}, t^\star), \tag{A.6}$$

and at the boundary nodes the bounce-back rule has to be used.

In this modified lattice-Boltzmann equation, also the densities ρ_α and total fluid momentum $\mathbf{j} = \rho\mathbf{v}$ have a modified expression, which takes into account the coupling of the electrostatic potential with the ionic species ρ_+ and ρ_-:

$$\rho_\alpha(\mathbf{r}, t+1) = \sum_{i=0}^{18} \left[n_i^\alpha(\mathbf{r}, t+1) - \frac{z_\alpha}{2} a_0^i \rho_\alpha(\mathbf{r} - \mathbf{c}_i, t) \nabla\Phi(\mathbf{r} - \mathbf{c}_i, t) \cdot \mathbf{c}_i\right] \tag{A.7}$$

and

$$\mathbf{j}(\mathbf{r}, t+1) = \sum_{\alpha=1}^{3} \left[\sum_{i=1}^{18} n_i^\alpha(\mathbf{r}, t+1)\mathbf{c}_i - c_s^2 z_\alpha \rho_\alpha(\mathbf{r}, t+1)\nabla\Phi(\mathbf{r}, t+1)\right], \tag{A.8}$$

where $z_s = 0$. Equations (A.7) and (A.8) are only justified in retrospect by a showing that, in the continuum limit, the electrokinetic equations are recovered.

In Reference [50], also a rest probability density was considered, with weight γ_s. This weight could (in principle) be varied to tune the diffusivity. However, the method turned out to be strictly valid only for the special case γ_s=1 [83]; therefore I have written the equations accordingly.

A.1.1 Continuum limit

On a lattice, the Taylor expansion [84] of a function $f(\mathbf{r}-\mathbf{c}_i, t-1)$ takes the form:

$$f\left(\mathbf{r}-\mathbf{c}_i, t-1\right) = f\left(\mathbf{r}, t\right) - \left(\partial_t + w_i \mathbf{c}_i \cdot \nabla\right) f\left(\mathbf{r}, t\right) + \frac{1}{2}\left(\partial_t + w_i \mathbf{c}_i \cdot \nabla\right)^2 f\left(\mathbf{r}, t\right) + o\left(\partial^3\right), \quad \text{(A.9)}$$

where the w_i's are weights determined by the following summation rules:

$$\sum_{i=1}^{N} a_0^i w_i = 1 \quad \text{(A.10)}$$

$$\sum_{i=1}^{N} a_0^i w_i \mathbf{c}_i = 0 \quad \text{(A.11)}$$

$$\sum_{i=1}^{N} a_0^i w_i \mathbf{c}_i^2 = c_s^2, \quad \text{(A.12)}$$

where N is the connectivity of the lattice.

In order to perform the Chapman–Enskog expansion, let us substitute the equations for the one-particle distribution functions in the equations defining the hydrodynamic fields ρ_α and $\mathbf{j}$. The equation for the density becomes

$$\begin{aligned} \rho_\alpha(\mathbf{r}, t) &= \sum_i^N a_0^i \left[\rho_\alpha(\mathbf{r}-\mathbf{c}_i, t-1) + \frac{\mathbf{j}_\alpha(\mathbf{r}-\mathbf{c}_i, t-1)\cdot \mathbf{c}_i}{c_s^2} + \right. \\ &\left. + \frac{z_\alpha}{2}\rho_\alpha(\mathbf{r}-\mathbf{c}_i, t-1)\nabla\Phi(\mathbf{r}-\mathbf{c}_i, t-1)\cdot\mathbf{c}_i\right], \end{aligned} \quad \text{(A.13)}$$

while the one for the partial currents $\mathbf{j}_\alpha = \rho_\alpha \mathbf{j} / \sum_\alpha \rho_\alpha$ is

$$\mathbf{j}_\alpha\left(\mathbf{r}, t\right) = \sum_{i=1}^{N} a_0^i \left[\rho\left(\mathbf{r}-\mathbf{c}_i, t-1\right)\mathbf{c}_i + \frac{\mathbf{j}_\alpha\left(\mathbf{r}-\mathbf{c}_i, t-1\right)}{c_{sv}^2}\cdot\mathbf{c}_i\mathbf{c}_i\right] - c_s^2 z_\alpha \rho\left(\mathbf{r}, t\right)\nabla\phi\left(\mathbf{r}, t\right). \quad \text{(A.14)}$$

Next, we should Taylor expand the previous equations and compute the macroscopic fields. I list the expansion of the single terms present in the previous expressions:

$$\begin{aligned} \sum_{i=1}^{N} a_0^i f\left(\mathbf{r}-\mathbf{c}_i, t-1\right) &= \sum_{i=1}^{N} a_0^i \left[f - \partial_t f - w_i\mathbf{c}_i\cdot\nabla f + \frac{1}{2}\left(\partial_t + w_i\mathbf{c}_i\cdot\nabla\right)^2 f + ...\right] \\ &= \sum_{i=1}^{N} a_0^i \left[f - \partial_t f + \frac{1}{2}\partial_t^2 f + \frac{1}{2} w_i \mathbf{c}_i^2 \nabla^2 f + ...\right] \\ &= f - \partial_t f + \frac{1}{2}\partial_t^2 f + \frac{c_s^2}{2}\nabla^2 f; \end{aligned} \quad \text{(A.15)}$$

$$\sum_{i=1}^{N} a_0^i f\left(\mathbf{r}-\mathbf{c}_i, t-1\right)\mathbf{c}_i = \sum_{i=1}^{N} a_0^i \left[f - \partial_t f - w_i\mathbf{c}_i\cdot\nabla f + \frac{1}{2}\left(\partial_t + w_i\mathbf{c}_i\cdot\nabla\right)^2 f + ...\right]\mathbf{c}_i$$

$$
\begin{aligned}
&= \sum_{i=1}^{N} a_0^i \left[-w_i \mathbf{c}_i \cdot \nabla f + w_i \partial_t \mathbf{c}_i \cdot \nabla f \right] \mathbf{c}_i \qquad \text{(A.16)}\\
&= \left(-\nabla f + \partial_t \nabla f \right) \sum_{i=1}^{N} a_0^i w_i \mathbf{c}_i^2 \\
&= \left(-\nabla f + \partial_t \nabla f \right) c_{sv}^2;
\end{aligned}
$$

$$
\begin{aligned}
\sum_{i=1}^{N} a_0^i \mathbf{j}\left(\mathbf{r} - \mathbf{c}_i, t-1\right) \cdot \mathbf{c}_i \mathbf{c}_i &= \sum_{i=1}^{N} a_0^i \left[\mathbf{j} - \partial_t \mathbf{j} - w_i \mathbf{c}_i \cdot \vec{\nabla} \mathbf{j} - \frac{1}{2} \left(\partial_t + w_i \mathbf{c}_i \cdot \vec{\nabla} \right)^2 \mathbf{j} + ... \right] \cdot \mathbf{c}_i \mathbf{c}_i \\
&= \sum_{i=1}^{N} a_0^i \left[\mathbf{j} - \partial_t \mathbf{j} + \frac{1}{2} \partial_t^2 \mathbf{j} + \frac{1}{2} w_i^2 \left(\mathbf{c}_i \cdot \vec{\nabla} \right)^2 \mathbf{j} \right] \cdot \mathbf{c}_i \mathbf{c}_i \qquad \text{(A.17)} \\
&= \left(\mathbf{j} - \partial_t \mathbf{j} + \frac{1}{2} \partial_t^2 \mathbf{j} \right) \sum_{i=1}^{N} a_0^i \mathbf{c}_i \mathbf{c}_i + \nabla^2 \mathbf{j} \sum_{i=1}^{N} a_0^i w_i^2 \frac{\mathbf{c}_i^2 \mathbf{c}_i \mathbf{c}_i}{2} \\
&= \left(\mathbf{j} - \partial_t \mathbf{j} + \frac{1}{2} \partial_t^2 \mathbf{j} + \frac{\nabla^2 \mathbf{j}}{6} \right) c_s^2.
\end{aligned}
$$

If we substitute Eqs. (A.15), (A.16), and (A.17) into Eqs. (A.13) and (A.14), we obtain the following macroscopic equations for the hydrodynamic fieldsρ_α and $\mathbf{j}_\alpha$:

$$
\begin{aligned}
\partial_t \rho_\alpha &= \frac{1}{2} \partial_t^2 \rho_\alpha - \nabla \cdot \mathbf{j}_\alpha + \partial_t \nabla \cdot \mathbf{j}_\alpha + \frac{c_{\mathrm{S}}^2}{2} \left(\nabla^2 \rho_\alpha + z_\alpha \nabla \cdot \rho_\alpha \nabla \Phi \right), \qquad \text{(A.18)} \\
\partial_t \mathbf{j}_\alpha &= -c_\alpha^2 \nabla \rho_\alpha + c_{\mathrm{S}}^2 \partial_t \nabla \rho_\alpha + \frac{1}{2} \partial_t^2 \mathbf{j}_\alpha + \frac{1}{6} \nabla^2 \mathbf{j}_\alpha - c_{\mathrm{S}}^2 z_\alpha \rho_\alpha \nabla \Phi. \qquad \text{(A.19)}
\end{aligned}
$$

A.1.2 Chapman Enskog procedure

The Chapman-Enskog procedure allows to separate the time scales at which the different mechanisms of mass and momentum transfer occurs. Specifically, we expect the following phenomena [9]

1. relaxation to local equilibrium on time scales $O(\epsilon^0)$
2. density perturbation propagating as sound waves on time scales $O(\epsilon^1)$
3. diffusive and advective effects on time scales $O(\epsilon^2)$

Thus, the time and space derivatives are expressed as

$$
\begin{aligned}
\nabla &= \epsilon \nabla_1 \qquad \text{(A.20)} \\
\partial_t &= \epsilon \partial_{t_1} + \epsilon^2 \partial_{t_2}. \qquad \text{(A.21)}
\end{aligned}
$$

If we substitute Eqs. (A.20) and (A.21) into Eq. (A.18), we obtain

$$
\begin{aligned}
\left(\epsilon \partial_{t_1} + \epsilon^2 \partial_{t_2} \right) \rho_\alpha &= \frac{1}{2} \left(\epsilon \partial_{t_1} + \epsilon^2 \partial_{t_2} \right) \left(\epsilon \partial_{t_1} + \epsilon^2 \partial_{t_2} \right) \rho_\alpha - \\
&\quad - \epsilon \nabla_1 \cdot \mathbf{j}_\alpha + \left(\epsilon \partial_{t_1} + \epsilon^2 \partial_{t_2} \right) \epsilon \nabla_1 \cdot \mathbf{j}_\alpha + \qquad \text{(A.22)} \\
&\quad \frac{c_{\mathrm{S}}^2}{2} \left[\left(\epsilon \nabla_1 \right) \left(\epsilon \nabla_1 \right) \rho_\alpha + z_\alpha \epsilon \nabla_1 \cdot \left(\rho_\alpha \epsilon \nabla_1 \Phi \right) \right].
\end{aligned}
$$

Keeping only terms up to second order in ϵ, Eq. (A.22) simplifies to

$$\begin{aligned}\left[\epsilon\partial_{t_1}+\epsilon^2\partial_{t_2}\right]\rho_\alpha &= -\epsilon\nabla_1\cdot\mathbf{j}_\alpha+\epsilon^2\left[\frac{1}{2}\partial_{t_1}^2\rho_\alpha+\partial_{t_1}\nabla_1\cdot\mathbf{j}_\alpha\right]\\ &+ \epsilon^2\frac{c_s^2}{2}\left(\nabla_1^2\rho_\alpha+z_\alpha\nabla_1\cdot\rho_\alpha\nabla_1\Phi\right),\end{aligned}\tag{A.23}$$

while Eq. (A.19) becomes

$$\begin{aligned}\left[\epsilon\partial_{t_1}+\epsilon^2\partial_{t_2}\right]\mathbf{j}_\alpha &= -\epsilon c_s^2\left[\nabla_1\rho_\alpha+z_\alpha\rho_\alpha\nabla_1\Phi\right]+\\ &+ \epsilon^2\left[c_{\mathrm{S}}^2\partial_{t_1}\nabla_1\rho_\alpha+\frac{1}{2}\partial_{t_1}^2\mathbf{j}_\alpha+\frac{1}{6}\nabla_1^2\mathbf{j}_\alpha\right].\end{aligned}\tag{A.24}$$

Let us now identify the different mechanisms of mass and momentum transfer. At the ϵ scale we obtain

$$\partial_{t_1}\rho_\alpha = -\nabla_1\cdot\mathbf{j}_\alpha,\tag{A.25}$$

$$\partial_{t_1}\mathbf{j}_\alpha = -c_s^2\left(\nabla_1\rho_\alpha+z_\alpha\rho_\alpha\nabla_1\Phi\right).\tag{A.26}$$

Eq. (A.25) is the continuity equation for mass conservation. By taking the sum over s on both sides of Eq. (A.26) one obtains the "fast" part of the linearized Navier–Stokes equation for the total mass current $\mathbf{j}$:

$$\partial_{t_1}\mathbf{j}=-c_{\mathrm{S}}^2\sum_\alpha\nabla_1\rho_\alpha-c_{\mathrm{S}}^2\sum_\alpha z_\alpha\rho_\alpha\nabla_1\Phi.\tag{A.27}$$

On the ϵ^2 scale we have

$$\partial_{t_2}\rho_\alpha = \frac{1}{2}\partial_{t_1}^2\rho_\alpha+\partial_{t_1}\nabla_1\cdot\mathbf{j}_\alpha+\frac{c_s^2}{2}\left(\nabla_1^2\rho_\alpha+z_\alpha\nabla_1\cdot\rho_\alpha\nabla_1\hat{\Phi}\right),\tag{A.28}$$

$$\partial_{t_2}\mathbf{j}_\alpha = c_{\mathrm{S}}^2\partial_{t_1}\nabla_1\rho_\alpha+\frac{1}{2}\partial_{t_1}^2\mathbf{j}_\alpha+\frac{1}{6}\nabla_1^2\mathbf{j}_\alpha.\tag{A.29}$$

In Equation (A.28) I collect ∇_1 and obtain

$$\begin{aligned}\partial_{t_2}\rho_\alpha &= \frac{1}{2}\partial_{t_1}^2\rho_\alpha+\partial_{t_1}\nabla_1\cdot\mathbf{j}_\alpha+\frac{c_s^2}{2}\nabla_1\cdot\left(\nabla_1\rho_\alpha+z_\alpha\rho_\alpha\nabla_1\hat{\Phi}\right)\\ &= \frac{1}{2}\partial_{t_1}^2\rho_\alpha+\partial_{t_1}\nabla_1\cdot\mathbf{j}_\alpha-\frac{1}{2}\nabla_1\cdot(\partial_{t_1}\mathbf{j}_\alpha)\\ &= \frac{1}{2}\partial_{t_1}^2\rho_\alpha+\frac{1}{2}\partial_{t_1}\nabla_1\cdot\mathbf{j}_\alpha,\end{aligned}\tag{A.30}$$

which by means of Eq. (A.25) gives

$$\partial_{t_2}\rho_\alpha=0.\tag{A.31}$$

This equation expresses the fact that the diffusion has already relaxed on the faster time scale t_1. This, however, is not the relevant time scale at which a diffusion process has to take place. Moreover, the diffusion coefficients will be linked to the fast degrees of freedom and it will not be possible to vary them. Let us go back to the microscopic evolution equation and add an extra term to obtain, on the t_2 time scale, a diffusive term. The correction amounts to the addition of the term

$$D_\alpha\sum_i^N a_0^i\left[-\frac{\nabla\rho_\alpha(\mathbf{r}-\mathbf{c}_i,t-1)}{c_s^2}-\frac{z_\alpha}{2}\rho_\alpha(\mathbf{r}-\mathbf{c}_i,t-1)\nabla\Phi(\mathbf{r}-\mathbf{c}_i,t-1)\right]\cdot\mathbf{c}_i\tag{A.32}$$

to the Eq. (A.13) defining the microscopic dynamics of the density. By repeating the Chapman-Enskog procedure, on the slow t_2 time scale, we obtain

$$\partial_{t_2}\rho_\alpha = D_\alpha \left[\nabla^2\rho_\alpha + z_\alpha \nabla\cdot(\rho_\alpha \nabla\Phi)\right], \tag{A.33}$$

which is the diffusive behavior described by the Smoluchowski equation (A.1). Because the factor D_α of Eq. (A.32) is freely adjustable, one can in principle impose the desired diffusivity. To make sure that this is possible in practice, one should nonetheless perform a proper test which falls outside the scope of this chapter. The remaining part of the Chapman-Enskog procedure will be a mere repetition of that of Ref. [50], to which I refer the reader for details.

A.2 Boundary nodes and origin of the spurious currents

The second problem of this lattice-Boltzmann implementation concerns the formation of spurious currents at boundary nodes due to a slight imbalance of the microscopic equations.

For the sake of simplicity, I illustrate this phenomenon in the simplest case of the discretization of the gradient of a scalar field ρ, defined at every lattice node. The function

$$f(\mathbf{r}) = \sum_{i=1}^{N} \frac{a_0^i}{c_s^2}\rho(\mathbf{r}+\mathbf{c}_i)\,\mathbf{c}_i \tag{A.34}$$

is the lattice counterpart of the gradient, provided that the summation rules

$$\sum_{i=1}^{N} a_0^i \mathbf{c}_i \quad = \quad 1, \tag{A.35}$$

and

$$\sum_{i=1}^{N} a_0^i w_i \mathbf{c}_i^2 = c_s^2, \tag{A.36}$$

[which is Eq. (A.12)] are satisfied. By using them and the Taylor expansion Eq. (A.9), it is easy to prove that $f(\mathbf{r})$ is, indeed, the gradient of ρ:

$$\begin{aligned} f(\mathbf{r}) &= \sum_{i=1}^{N} \frac{a_0^i}{c_s^2}\rho(\mathbf{r}+\mathbf{c}_i)\,\mathbf{c}_i = \frac{1}{c_s^2}\sum_{i=1}^{N} a_0^i \rho(\mathbf{r})\mathbf{c}_i + \sum_{i=1}^{N} a_0^i w_i \left[(\mathbf{c}_i\cdot\nabla)\,\rho(\mathbf{r})\right]\mathbf{c}_i \\ &= \frac{\rho(\mathbf{r})}{c_s^2}\left[\sum_{i=1}^{N} a_0^i \mathbf{c}_i\right] + \frac{\nabla\rho}{c_s^2}\left[\sum_{i=1}^{N} a_0^i w_i \mathbf{c}_i^2\right] \\ &= \nabla\rho. \end{aligned} \tag{A.37}$$

Equations (A.35) and (A.36) are valid only when the summation is performed over all the N velocities allowed by the connectivity of the lattice. Then, it is immediately clear what happens on a boundary node, where we have to employ the the bounce-back rule for all the boundary links. For specificity, if the links $i = 1, ..., N'$ connect fluid nodes, while the remaining links $i = N', ..., N$ are the boundary links, the function $f(\mathbf{r})$ defined by Eq. (A.34) becomes (I substitute $a_1^i = a_0^i/c_s^2$)

$$f(\mathbf{r}) \quad = \quad \sum_{i=1}^{N'} a_1^i \rho(\mathbf{r}+\mathbf{c}_i)\,\mathbf{c}_i + \sum_{i=N'}^{N} a_1^i \rho(\mathbf{r})\,\mathbf{c}_i, \tag{A.38}$$

where the second term represents the populations that have been reflected back.

In order to explicitly compute the correction terms, let us Taylor expand the first part of Eq. (A.38)

$$\begin{aligned} f(\mathbf{r}) &= \sum_{i=1}^{N'} a_1^i \rho(\mathbf{r}) \mathbf{c}_i + \sum_{i=1}^{N'} a_1^i w_i \left[(\mathbf{c}_i \cdot \nabla) \rho(\mathbf{r}) \right] \mathbf{c}_i + \sum_{i=N'}^{N} a_1^i \rho(\mathbf{r}) \mathbf{c}_i \\ &= \sum_{i=1}^{N} a_1^i \mathbf{c}_i + \nabla \rho \left[\sum_{i=1}^{N'} w_i a_1^i \mathbf{c}_i^2 \right] \\ &= \nabla \rho \left[\sum_{i=1}^{N'} w_i a_1^i \mathbf{c}_i^2 \right]. \end{aligned} \tag{A.39}$$

Equations (A.39) tell us that on a boundary node the function $f(\mathbf{r})$ is not *exactly* equal to the gradient. Therefore, by repeating the Chapman-Enskog procedure on a boundary node, one no longer recovers the macroscopic equations. Hence, there will always be spurious currents arising from this (small) mismatch.

One can cure these spurious boundary currents by explicitly putting the correction suggested by Eqs. (A.39), and compute the gradient with the expression

$$\nabla \rho = \frac{f(\mathbf{r})}{\sum_{i=1}^{N'} w_i a_1^i \mathbf{c}_i^2}. \tag{A.40}$$

The readers may now expect similar corrections for all the expression which take part in the evolution equations [as Eqs. (A.15), (A.16), and (A.17)]. Although they can indeed be obtained, these corrections become increasingly involved and computationally expensive. To give an idea, I will explicitly show what happens to the expression given by Eq. (A.15), which I rewrite here:

$$\sum_{i=1}^{18} a_0^i \rho(\mathbf{r} - \mathbf{c}_i t - 1) = \rho - \partial_t \rho + \frac{1}{2} \partial_t^2 \rho + \frac{c_s^2}{2} \nabla^2 \rho. \tag{A.41}$$

At a boundary node, instead of Eq. (A.41), we have:

$$\begin{aligned} \sum_{i=1}^{18} a_0^i \rho(\mathbf{r} - \mathbf{c}_i t - 1) &= \sum_{i=1}^{N'} a_0^i \rho(\mathbf{r} - \mathbf{c}_i, t - 1) + \sum_{i=N'}^{N} a_0^i \rho(\mathbf{r}, t - 1) \\ &= \sum_{i=1}^{N\prime} a_0^i \left[\rho - \partial_t \rho - w_i \mathbf{c}_i \cdot \nabla \rho + \frac{1}{2} \left(\partial_t + w_i \mathbf{c}_i \cdot \nabla \right)^2 \rho + ... \right] + \\ &\quad + \sum_{i=N'}^{N} a_0^i \left[\rho - \partial_t \rho + \frac{1}{2} \partial_t^2 \rho + ... \right] \\ &= \sum_{i=1}^{N} a_0^i \left[\rho - \partial_t \rho + \frac{1}{2} \partial_t^2 \rho + ... \right] + \\ &\quad + \sum_{i=1}^{N'} a_0^i \left[-w_i \mathbf{c}_i \cdot \nabla \rho + w_i \partial_t \mathbf{c}_i \cdot \nabla \rho \right] \end{aligned} \tag{A.42}$$

In summary,

$$\sum_{i=1}^{18} a_0^i \rho\left(\mathbf{r}-\mathbf{c}_i t-1\right) = \rho - \partial_t \rho + \frac{1}{2}\partial_t^2 \rho + \frac{c_s^2}{2}\nabla^2 \rho + \tag{A.43}$$
$$+ \sum_{i=1}^{N'} a_0^i \left[-w_i \mathbf{c}_i \cdot \nabla \rho + w_i \partial_t \mathbf{c}_i \cdot \nabla \rho\right].$$

In Equation (A.43), the term in the square brackets is a spurious term which, if we want to correct the boundary lattice artifact, we should subtract to the left hand side. One should also not forget to put, in place of the density gradient, its corrected expression in terms of lattice quantities [Eq. (A.40)].

With Equation (A.43), I have shown that it is, in principle, possible to compute all the terms that will balance the macroscopic equations even in the presence of a boundary. At the same time, the reader might now be persuaded that these corrections become impractical.

In Chapter 5 Figure 5.7a, I show that all the imbalances at boundary nodes add up to give rise to spurious currents even in the absence of flow.

Bibliography

[1] L.D. Landau and E.M. Lifshitz. *Fluid Mechanics*. Butterworth/heinemann, Oxford, 2nd.rev.eng.ed. edition, 1998.

[2] V.G. Levich. *Physicochemical Hydrodynamics*. Prentice-Hall, Inc., 1962.

[3] R.F. Probstein. *Physicochemical Hydrodynamics*. Butterworth, Boston, 1989.

[4] G.K. Batchelor. *An Introduction to Fluid Dynamics*. Cambridge University Press, 1967.

[5] E.G.D. Cohen and W. Thirring, editors. *The Boltzmann Equation*. Sprienger-Verlag, Wien New York, 1973.

[6] G.R. Mcnamara and G. Zanetti. Use of the Boltzmann- equation ti simulate lattice-gas automata. *Phys. Rev. Lett.*, 61(20):2332, 1988.

[7] S. Succi. *The Lattice Boltzmann Equation for Fluid Dynamics and Beyond*. University Press, Oxford, 2001.

[8] A.J.C. Ladd. *J. Fluid Mech.*, 271:285, 1994.

[9] U. Frisch, D. d'Humières, B. Hasslacher, P. Lallemand, Y. Pomeau, and J.P. Rivet. *Complex Systems*, page 649, 1987. Reprinted in Lattica Gas Methods for Partial Differential Equations, Addison-Wesley, 1989.

[10] F.J. Higuera, S. Succi, and R. Benzi. Lattice gas-dynamics with enhanced collisions. *Europhys. Lett.*, 9(4):345, 1989.

[11] R. Benzi, S. Succi, and M. Vergassola. The lattice boltzmann equation: theory and applications. *Phys. Rep.*, 222:145, 1992.

[12] M.W. Heemels, M.H.J. Hagen, and C.P. Lowe. Simulating solid colloidal particles using the lattice-Boltzmann method. *J. Comp. Phys.*, 164(1):48, 2000.

[13] A.J.C. Ladd. *J. Fluid Mech.*, 271:311, 1994.

[14] Y.H. Qian, D. d'humières, and P. Lallemand. *Europhys. Lett.*, 17:479, 1992.

[15] D. d'Humières, P. Lallemand, and U. Frisch. *Europhys. Lett.*, 2:291, 1986.

[16] G. Gouy. *J.Physique*, 9(4):457, 1910.

[17] G. Gouy. *Ann.d.phys.*, 7(9):129, 1917.

[18] D.L. Chapman. *Phylos.Mag.*, 25(6):475, 1913.

[19] P. Debye and E. Hückel. *Physik. Z.*, 24:185, 1923.

[20] P. Debye and E. Hückel. *Physik. Z.*, 25:97, 1924.

[21] E.J.W. Verwey and J.TH.G. Overbeek. *Theory of the Stability of Lyophobic Colloids*. Elsevier, New York, 1948.

[22] J.N. Israelachvili. *Intermolecular and Surface Forces*. Academic Press, New York, 1991.

[23] R.J. Hunter. *Foundations of Colloid Science*. Oxford Science Publications, 1989.

[24] A.V. Delgado, editor. *Interfacial Electrokinetics and Electrophoresis*, volume 106 of *Surfactant Science Series*. Marcel Dekker Inc., New York, 2002.

[25] W.B. Russel, D.A. Saville, and W.R. Schowalter. *Colloidal Dispersion*. Cambridge University Press, 1995.

[26] R.J. Hunter. *The Zeta Potential in Colloidal Science*. Academic Press, 1981.

[27] F. Booth. *J. Chem. Phys.*, 22:1956, 1954.

[28] H. Ohshima, T.W. Healy, L.R. White, and R.W. O'Brien. Sedimentation Velocity and Potential in a Dilute Suspension of Charged Spherical Colloidal Particles. *J.Chem.Soc., Faraday Trans. 2*, 80:1299, 1982.

[29] E. Hückel. *Phys Z*, 25:204, 1924.

[30] M. von Smoluchowski. *Physical Chemestry*, 92:129, 1918.

[31] H. Ohshima. Electrophoresis of Charged Particles and Drops. In Delgado, editor, *Interfacial Electrokinetics and Electrophoresis*, chapter 5, page 123. Marcel Dekker Inc., 2002.

[32] J.L. Viovy. Electrophoresis of DNA and other polyelectrolytes: Physical mechanisms. *Rev. Mod. Phys.*, 72(3):813, 2000.

[33] S.R. de Groot and P. Mazur. *Non-equilibrium thermodynamics*. Dover, New York, 1984.

[34] H.C. Brinkman. *Appl. Sci. Res.*, A1:27, 1947.

[35] F.W. Wiegel. *Fluid Flow Through Porous Macromolecular Systems*. Sprienger-Verlag, Berlin Heidelberg New York, 1980.

[36] M. Sahimi. *Flow and Transport in Porous Media and Fractured Rock. From Classical Methods to Modern Approaches*. VCH, Weinheim, Germany, 1995.

[37] D.L. Koch and J.F. Brady. *J. Fluid Mech.*, 154:399, 1984.

[38] A. Acrivos, E.J. Hinch, and E.J. Jeffrey. *J. Fluid Mech.*, 101:403, 1980.

[39] R.E. Caflisch and J.H.C. Luke. *Phys. Fluids*, 28:759, 1985.

[40] A.J.C. Ladd. *Phys. Rev. Lett.*, 88:048301–1, 2002.

[41] C.P. Lowe and D. Frenkel. *Phys. Rev. Lett.*, 77:4552, 1996.

[42] D.L. Koch, R.J. Hill, and A.S. Sangani. *Phys. Fluids*, 10:2025, 1998.

[43] L.J. Durlofsky and J.F. Brady. *Phys. Fluids*, 30:3329, 1987.

[44] W.H. Press, S.A. Teukolski, and W.T. Vetterling. *Numerical Recipes*. Cambridge University Press, Cambridge, 1996.

[45] C. Holm, P. Kèkicheff, and R. Podgornik eds. *Electrostatic effects in Soft Matter and Biophysics*. NATO Sci. Series, Kluwer Ac. Pub., Dordrecht, 2001.

[46] W.M. Gelbart, R.F. Bruinsma, and P.A. Pincus. *Phys. Today*, 53:38, 2000.

[47] A.D. Stroock, S.K.W. Deringer, A. Ajdari, I. Mezic, H.A. Stone, and G.M. Whitesides. *Science*, 295:647, 2002.

[48] R.D. Groot. *J. Chem. Phys.*, 118:11265, 2003.

[49] P.B. Warren. *Int. J. Modern Phys. C*, 8:889, 1997.

[50] J. Horbach and D. Frenkel. *Phys. Rev. E*, 64:061507, 2001.

[51] W.R. Osborn, E. Orlandini, M.R. Swift, and J.M. Yeomans. *Phys. Rev. Lett.*, 75:4031, 1995.

[52] M.R. Swift, E. Orlandini, W.R. Osborn, and J.M. Yeomans. *Phys. Rev. E*, 54:5041, 1996.

[53] A.J.C. Ladd and R. Verberg. *J. Stat. Phys.*, 104:1191, 2001.

[54] L.-S. Luo and S.S. Girimaji. *Phys. Rev. E*, 66:035301, 2002.

[55] N.-Q. Nguyen and A.J.C. Ladd. *Phys. Rev. E*, 66:046708, 2002.

[56] H. Hashimoto. *J. Fluid Mech.*, 5:317, 1959.

[57] A.J.C. Ladd. *J. Chem. Phys.*, 93:3484, 1990.

[58] S Alexander, P.M. Chaikin, P. Grant, G.J. Morales, P. Pincus, and D. Hone. Charge renormalization, osmotic pressure, and bulk modulus of colloidal crystals: Theory. *Journal of Chemical Physics*, 1984.

[59] A.D. MacGillivray and J.J.Jr. Winkelman. *J. Chem. Phys.*, 45:2184, 1966.

[60] R.M. Fuoss, A. Katchalsky, and A. Lifson. *Proc. Natl. Acad. Sci. U.S.*, 37:579, 1951.

[61] E. Trizac, L. Bocquet, and M. Aubouy. Simple approach for charge renormalization in highly charged macroions. *Phys. Rev. Lett.*, 89(24), 2002.

[62] L. Bocquet, E. Trizac, and M. Aubouy. Effective charge saturation in colloidal suspensions. *J. Chem. Phys.*, 117(17):8138, 2002.

[63] S. Manning, G. *J. Chem. Phys.*, 51:924, 1969.

[64] G.S. Manning and J. Ray. Counterion condensation revisited. *J. Biomol. Struct.& Dynamics*, 16(2):461, 1998.

[65] H. Ohshima, T.W. Healy, L.R. White, and R.W O'Brien. Sedimentation Velocity and Potential in a Dilute Suspension of Charged Spherical Colloidal Particles. *J.Chem.Soc., Faraday Trans. 2*, pages 1310, Eq.(78), 1982.

[66] G.A. Schumacher and T.G.M. de Ven, van. Brownian Motion of Charged Colloidal Particles surrounded by Electric Double Layers. *Faraday Discuss. Chem. Soc.*, 83:75, 1987.

[67] H. Ohshima. Electrophoresis of Charged Particles and Drops. In Delgado, editor, *Interfacial Electrokinetics and Electrophoresis*, chapter 5, pages 135, Eq. (54). Marcel Dekker Inc., 2002.

[68] D. Long, J.L. Viovy, and A. Ajdari. Simultaneous action of electric fields and nonelectric forces on a polyelectrolyte: Motion and deformation. *Phys. Rev. Lett.*, 76(20):3858, 1996.

[69] D. Long and A. Ajdari. Symmetry properties of the electrophoretic motion of patterned colloidal particles. *Phys. Rev. Lett.*, 81(7):1529, 1998.

[70] A. Ortega and J.G. de la Torre. Hydrodynamic properties of rodlike and disklike particles in dilute solution. *J. Chem. Phys.*, 119(18):9914, 2003.

[71] W.E. Williams. Thin disks. *Journal of Fluid Mechanics*, 25:589, 1966.

[72] J. Happel and H. H.Brenner. *Low Reynolds number hydrodynamics.* Nijhoff, Dordrecht, The Netherland, 1983.

[73] S.L. Tawari, D.L. Koch, and C. Cohen. Electrical double-layer effects on the Brownian diffusivity and aggregation rate of Laponite clay particles. *J. Colloid Interface Sci.*, 240(1):54, 2001.

[74] H.J. Keh and J.M. Ding. Sedimentation velocity and potential in concentrated suspensions of charged spheres with arbitrary double-layer thickness. *J. Colloid Interface Sci.*, 227(2):540, 2000.

[75] P.G. Righetti. *Isoelectric Focusing: Theory, Methodology and Applications.* Elsevier, Amsterdam, 1983.

[76] P.G. Righetti, A. Stoyanov, and M. Zhukov. *The Proteome Revisited: Theory and Practice of All Relevant Electrophoresis Steps.* Elsevier, Amsterdam, 2001.

[77] E.M. Baskin, B.I. Shklovskii, and G.V. Zilberstein. Electrophoretic separation of proteins via complexation with a polyelectrolyte. *Physica A*, 317(3-4):313, 2003.

[78] J.L. Anderson. Effect of Nonuniform Zeta Potential on Particle Movement in Electric Fields. *J. Colloid. Interf. Science*, 105(1):45, 1985.

[79] J.D. Jackson. *Classical Electrodynamics*. John Wiley & Sons, 1962.

[80] http://scienceworld.wolfram.com/physics.

[81] X.W. Shan and H.D. Chen. Lattice boltzmann model for simulating flows with multiple phases and components. *Phys. Rev. E*, 47(3):1815, 1993.

[82] S. Melchionna and S. Succi. Electrorheology in nanopores via lattice Boltzmann simulation. *J. Chem. Phys.*, 120(9):4492, 2004.

[83] J. Horbach. Informal discussion.

[84] S. Wolfram. Cellular Automaton Fluids 1: Basic Theory. *J. Stat. Phys.*, 45:471, 1986. Reprinted in Lattica Gas Methods for Partial Differential Equations, Addison-Wesley, 1989.

Samenvatting

In dit proefschrift ligt de nadruk op *elektrohydrodynamica*. De elektrohydrodynamica beschrijft systemen waarin hydrodynamische (door stroming veroorzaakte) en elektrostatische (door lading veroorzaakte) interacties van vergelijkbare sterkte zijn en daardoor met elkaar concurreren. Op toegepast gebied is er hernieuwde interesse in dit vakgebied vanwege het praktisch nut voor *microfluidics* en voor de biofysica. Op theoretisch gebied is elektrohydrodynamica nog steeds uitdagend vanwege de inherente niet-lineariteit van de bijbehorende vergelijkingen.

Het eerste onderwerp in dit proefschrift - en tevens het enige dat niet gerelateerd is aan geladen colloïden - is het bestuderen van stroming in poreuze media door middel van de rooster-Boltzmannmethode. In hoofdstuk 4 heb ik laten zien hoe snelheidsfluctuaties gedempt worden in een eenvoudig model van een poreus medium. Tevens heb ik laten zien hoe het gebruik van benaderingen in vergelijkingen die op hun beurt weer gebaseerd zijn op de vooraf gemiddelde eigenschappen van de stroming tot grote fouten kan leiden. Dit strookt niet met de aanname die ten grondslag ligt aan bestaande theorieën voor hydrodynamische dispersie. In een poging om stroming in poreuze media te bestuderen, heb ik een zeer vereenvoudigd rooster-Boltzmannmodel voor poreuze media geïntroduceerd. Dit model heeft de prettige eigenschap dat het geen uitgesloten volume heeft, maar dat er toch wrijving van de vloeistof met obstakels mogelijk is. In hetzelfde hoofdstuk heb ik een eenvoudige methode gepresenteerd om het grootst mogelijke Pecletnummer te verkrijgen. (in roostersimulaties wordt het Pecletnummer altijd beperkt tot lage waarden door kunstmatige diffusie, veroorzaakt door simulatieartefacten).

In hoofdstuk 3 heb ik een korte introductie gegeven van de elektrokinetische vergelijkingen. In hoofdstuk 5 heb ik een nieuwe, tijdens mijn promotietijd ontwikkelde, methode beschreven die het mogelijk maakt om deze elektrokinetische vergelijkingen te behandelen en om voorheen nog niet verkende stromingscondities te bestuderen. Deze hybride methode koppelt een rooster-Boltzmannmodel voor het neutrale oplosmiddel aan een discretisatie van de Smoluchowskibeschrijving voor de opgeloste deeltjes. Deze combinatie van verschillende methodes is gerechtvaardigd door de keuze van het beschrijvingsniveau van de verschillende componenten in het systeem: de grote colloïdale deeltjes en kleine ionen zijn zeer verschillend van grootte. Een belangrijke eigenschap van de nieuwe methode is dat deze zich strikt houdt aan massa- en impulsbehoud op het niveau van een enkel roosterpunt, waardoor onnatuurlijke transportmechanismen zijn uitgesloten. De methode is bovendien zeer eenvoudig te implementeren en kan volledig parallel worden uitgevoerd. Om de voordelen van deze pragmatische aanpak te tonen, laat ik in appendix A twee technische problemen zien die uit een ander rooster-Boltzmannmodel voortkomen. Kleine discrepanties leiden

daar tot onnatuurlijke massastromen aan het oppervlak van een macroscopisch object, die de subtiele interacties waarin we geïnteresseerd zijn overstemmen. Concluderend meen ik dat de methode, hoewel deze nog verbeterd kan worden, reeds erg flexibel is en zeer geschikt om *microfluidics* en colloïdale suspensies van geladen deeltjes te bestuderen. Hoewel de methode in dit proefschrift nog niet uitgebreid is toegepast op *microfluidics*, meen ik dat dát het vakgebied is waarin het potentieel ervan volledig benut kan worden.

Het resterende deel van dit proefschrift beschrijft verkennende studies naar de elektrokinetische eigenschappen van geladen colloïden in elektrolyten, gebruik makend van het in hoofdstuk 5 geïntroduceerde rooster-Boltzmannmodel. De keuze voor een systeem van geladen colloïden in elektrolyten komt voort uit vragen als: hoe hangt de mobiliteit van een deeltje af van zijn vorm en ladingsverdeling?

In hoofdstuk 6 heb ik computersimulaties beschreven van de sedimentatiesnelheid van sterk geladen bollen. Ik heb laten zien dat deze sedimentatiesnelheid kan worden uitgedrukt in de evenwichtseigenschappen van de elektrische dubbellaag. Bovendien wordt deze afhankelijkheid bij sterke lading beïnvloed door de accumulatie van lading op het oppervlak van de bol. De sedimentatiesnelheid lijkt dan op die van een bol in een elektrolyt zonder toegevoegd zout, waarbij co-ionen geen invloed meer hebben op sedimentatiesnelheid en alleen de dynamica van de contra-ionen is relevant is.

Een ander belangrijk aspect van de elektrohydrodynamische interactie dat nogmaals de flexibiliteit van de methode aantoont, is de studie naar het effect van de vorm van colloïden op de elektrokinetica. Hoofdstuk 7 beschrijft een studie naar de rol van vorm, dichtheid, volumefractie, lading en ionenconcentratie op de sedimentatiesnelheid van schijfjes met een eindige dikte. Deze zijn zowel theoretisch relevant omdat ze een prototype zijn voor het bestuderen van algemene effecten van de vorm op de sedimentatiesnelheid, als praktisch relevant omdat ze een goed model vormen voor echte kleideeltjes. Mijn bevinding is dat schijfvormige deeltjes hydrodynamisch symmetrisch worden door niet-triviale interacties tussen het stromingsveld rond het deeltje en de elektrische dubbellaag.

De laatste toepassing die ik heb beschreven is de elektroforetische mobiliteit van een bol met geladen 'vlekken'. In hoofdstuk 8 heb ik laten zien hoe de elektroforetische mobiliteit van zon bol afhangt van het elektrische quadrupoolmoment en de Debyelengte. Ik heb ook laten zien dat als het door elektroforese voortbewogen deeltje niet exact bolvormig is (wat het geval is voor een bol in een roostermodel), er ook elektrische multipoolmomenten moeten worden beschouwd van een hogere orde dan het quadrupoolmoment.

Acknowledgments

The first person who I would like to thank is Daan Frenkel. Since the first time I met him Daan impressed me with the passion he puts in his research. More than with words, he teaches people how to do science with his example. Independently from how hard I studied one problem, he had always been able to consider it from a completely different perspective and to suggest a new, almost always more proficous, way to find a solution. His ideas are so strong that it usually took me good three days (or few hours of discussion with someone else) to fully understand Daan's suggestions.

I also thank my two co-promotors: Christopher Lowe and Ignacio Pagonabarraga. With Christopher, who is always full of ideas on how to begin a new project, I had the pleasure to work especially at the initial stages of my PhD. Ignacio's collaboration was decisive in putting into practice the method to study the electrokinetic phenomena, presented in Chapter 5, that constitutes the core of this manuscript. I thank him especially for his patience in working out together with me all the method's and computer code's little details.

Jürgen Horbach introduced me to the world of lattice-Boltzmann simulations of electrokinetic phenomena; with him I enjoyed several discussions.

I thank Angelo Cacciuto, Marco Cosentino Lagomarsino (with whom I shared one paper, the office, an aborted attempt to make a short movie, and great part of my social life in Amsterdam), and Nélido González-Segredo for their careful reading of this manuscript. If this thesis is provided with a "Samenvatting", this is thanks to the contribution of Ruud van Leeuwen and Simon Tindemans.

Working in, as Daan like to say, his groups (I can number at least three groups since I arrived at Amolf), has always been a great source of ideas and enthusiasm. I wanted to thank all the groups members individually with a word but it would take too much space. Sorry for that and thanks to you all! Besides Daan's group, the entire Amolf institute is a special environment, a research oasis, my thanks to all the Amolfers, who make it so.

One collective thank to all my friends, without other people even physics would be useless!

Finally, two special thanks. During the dark days, when writing this manuscript seemed an hopeless and never-ending task, thinking about Ilaria Giulia's way to life was an inexhaustible source of strength and motivations. My last thank to Annamaria, for her continuous support, for teaching me that life is about joy, for having chosen to be with me, and for her everlasting and contagious smile.

The work in this thesis covers the following publications:

Chapter 4:
F. Capuani, D. Frenkel and C.P. Lowe
Velocity fluctuations and dispersion in a simple porous medium
Phys. Rev. E 67, 5 (2003), 056306

Chapter 5:
F. Capuani, I. Pagonabarraga and D. Frenkel
Discrete solution of the electrokinetic equations
J. Chem. Phys. 121, 2 (2004), 973

Chapter 6:
F. Capuani, I. Pagonabarraga and D. Frenkel
Sedimentation velocity of highly charged spheres
(in preparation)

Chapter 7:
F. Capuani, I. Pagonabarraga and D. Frenkel
Sedimentation velocity of charged disks at various surface charge and volume fractions
(in preparation)

Chapter 8:
F. Capuani, D. Frenkel and I. Pagonabarraga
Electrophoretic mobility of charged-neutral model proteins
(in preparation)

other pubblications:

M. Cosentino Lagomarsino, F. Capuani, and C.P. Lowe
A simulation study of the dynamics of a driven filament in an Aristotelian fluid
J. Theor. Biol. 224, 2 (2003), 215